Master's Thesis in Physics

Simulations of anisotropy effects of classical spin dynamics in frustrated magnets at finite temperatures

Estrid B. Naver

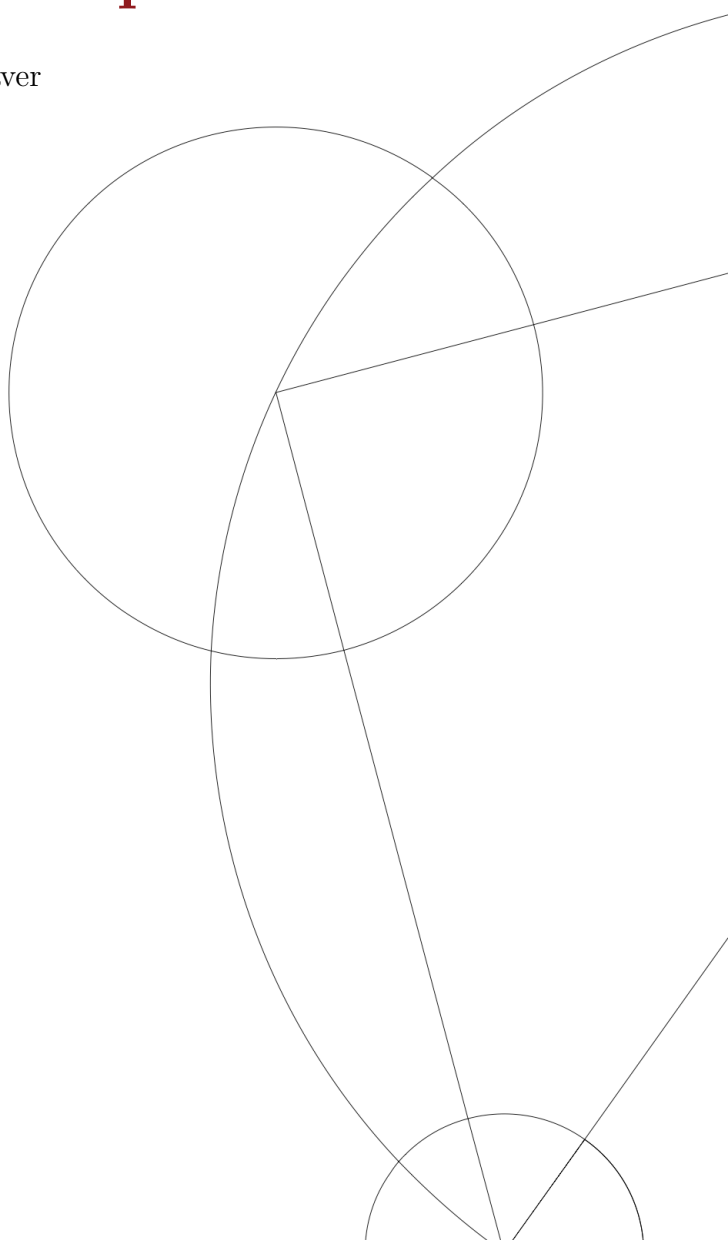

Supervisors
Henrik Jacobsen, Pascale Deen,
and Kim Lefmann

Niels Bohr Institute
1st of June, 2021

Contents

Abstract

Neutron scattering studies of $Gd_3Al_5O_{12}$ (GAG), a frustrated material with a hyperkagomé lattice, have shown several low lying magnetic excitations. A theoretical description of these excitations is missing, as they cannot be modelled using conventional spin wave theory. Spin dynamics simulations can help understanding the cause of the excitations. In this thesis we make use of an existing simulation program Copenhagen Langevin Spin Simulation Code (CLaSSiC), made to simulate Langevin spin dynamics. The single-ion anisotropy effect was implemented in the program and the physical parameters were validated both separately and in different combinations. These validations included both integration in spherical and Cartesian coordinates. The integration in spherical coordinates showed both instabilities and errors for simulations with finite temperature when compared to theory. The integration in Cartesian coordinates show results consistent with theoretical predictions, and using these we can accurately simulate the dynamics of any system of spins with nearest neighbour exchange interaction, single-spin anisotropy, applied magnetic field and temperature effects.
Two systems were simulated in order to compare to GAG, three spins in a triangle and 3×3 unit cells of a kagomé lattice, with various anisotropy directions and temperatures. These simulations used the same value for the exchange interaction as GAG with a similar temperature range as the neutron scattering studies. Simulating a hyperkagomé lattice would have taken too long with the current run time of the simulations.
The triangle with no anisotropy showed two excitation peaks, with one increasing in energy as a function of temperature, which shows a concrete example of the zero mode excitation at finite temperatures. The triangle with anisotropy in the local z-direction showed excitation peaks decreasing in energy as a function of temperature. The triangle with anisotropy in the local xy-plane had two excitations, the low energy excitation increasing in energy with temperature and the high energy excitation decreasing in energy with temperature. The kagomé lattice with no anisotropy showed signs of propagating spin waves, with a dispersion that was difficult to make out due to the low $\mathbf{q}$-resolution. The three kagomé simulations with anisotropies in the local z-axis, global z-axis and global xy-plane had energies constant in temperature. The kagomé lattice with anisotropy in the local xy-plane showed the energies changing as a function of temperature like for the triangle with anisotropy in the local xy-plane. In all the simulations with anisotropy the spin movements were confined by the anisotropy.
The shape of the excitation spectra for the triangle and the kagomé lattice with anisotropy in the local xy-plane both have two excitation peaks, with energies $E = 0.02$ meV and $E = 0.11$ meV for the triangle and $E = 0.03$ meV and $E = 0.15$ meV for the kagomé lattice. These are close to the energies of the excitation peaks INS1 and INS2 for GAG.
These simulations are a big step in the direction of understanding the excitations in GAG.

Acknowledgements

This thesis could not have been made without the help of other people. First and foremost Kim Lefmann, with his optimism and great knowledge of magnetism and neutron scattering. I would also like to thank Henrik Jacobsen for help with the ins and outs of fixing a simulation program and good advice in general. Thanks to Pascale Deen for help understanding frustrated garnets.
I would like to thank Emma Lenander for help working through shared confusion in the beginning of the project. I want to thank Jonas Hyatt for answering questions about the implementation of the program and coming up with a good name for it. Thanks to the lovely people in the magnetism and superconductivity group for good company and interesting conversation over lunch.
Thanks to my friends for proofreading the thesis. And finally a great thank to Stephen, for being supportive and excellent company during two lock downs.

Chapter 1

Introduction

Magnetism stems from magnetic moments arranged on a lattice. These magnetic moments can arrange themselves in a multitude of different ways, creating a wealth of different structures and effects. Competing interactions or geometric constraints can lead to the spins not ordering, an effect known as frustrated magnetism [1]. Often the frustration has a simple geometric origin like with three antiferromagnetic spins in a triangle. For Ising spins where the spins are confined to two directions, only one spin can be antiparallel to both its neighbours, as seen in Figure 1.1. For Heisenberg spins, the spins end up with 120° to each other, an example of which is seen in Figure 1.1.
This frustration leads to a large ground state degeneracy [2], now considered a key feature of frustration. Frustration can lead to interesting new states of matter like magnetic monopoles, spin liquids, and hidden order states [3], [1], [4].
Neutron scattering is an important tool in furthering our understanding of magnetic materials [5]. The magnetic moment of the neutrons makes them able to interact with magnetic materials and reveal their structure and dynamics [6], [7].

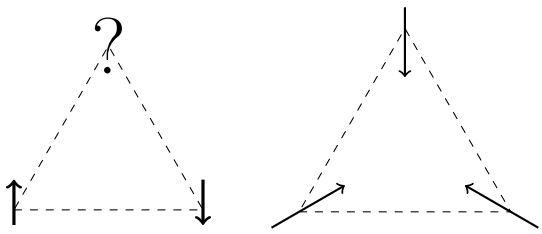

Figure 1.1

The frustrated antiferromagnet $Gd_3Al_5O_{12}$ (GAG) is one material under investigation. GAG has a lattice consisting of two sublattices of corner-sharing triangles, known as a hyperkagomé lattice as shown in Figure 2.10. The magnetic structure shows a very rich set of features, combining long-range and short-range order [4]. The study of dynamics has just recently started [4]. Inelastic neutron scattering studies have been done and several excitations identified, but the understanding of what behaviour causes these excitations is still lacking [4]. Due to the complexity of the system and the lack of long-range order, it is difficult to make theoretical predictions of the dynamics of GAG. Simulations can help bridge the gap between theory and experiments.

A simulation suite, Copenhagen Langevin Spin Simulation Code (CLaSSiC), has been written to perform numerical simulations of any lattice with nearest neighbour exchange, external magnetic field and temperature. The development of CLaSSiC was continued in this thesis by adding single-ion anisotropy and validating all of the interactions and different combinations of them. In an effort to build our understanding of spin dynamics in frustrated mag-

nets, and how they are affected by temperature and anisotropy strength, we simulated three spins in a triangle with and without anisotropy. To further get an idea of how the spin dynamics are affected by being in a lattice structure, we simulated a kagomé lattice consisting of 9 corner sharing triangles or 3×3 unit cells with various anisotropy directions.

The thesis is structured as follows. In Chapter 2 a brief introduction to the field of magnetism is given, with a focus on magnetic dynamics. Different types of magnetic excitations are discussed, like spin waves and the zero mode. The section finishes with a small review of existing literature about jarosite and two frustrated garnets, the examples of physical realisations of the kagomé and hyperkagomé lattices respectively. In Chapter 3 the theory behind neutron scattering is described and the neutron scattering cross section for magnetic dynamics derived. The implementation of CLaSSiC is described in Chapter 4. Chapter 5 goes through the extensive validation of the code performed during this thesis. Results of simulations of triangles and a kagomé lattice are presented in Chapter 6, along with the discussion of these. Finally the conclusion and outlook is presented in Chapter 7.

Chapter 2

Magnetism and Magnetic Interactions

In this chapter the theory behind the rest of the thesis will be described. We will go through the behaviour of a single magnetic moment, then go on to describe different interactions, like the exchange interaction and single ion anisotropy, and how these interactions lead to different types of magnetic order. This part of the chapter is based primarily on [8]. This thesis is focused on spin behaviour, so we go into more depth about spin dynamics. We explain the equation of motion that describes spin dynamics with the different interactions. The equation of motion is then used to derive dispersion relations for spin waves on a one-dimensional spin chain, and describe zero mode behaviour in different spin systems. A quick overview of current knowledge of a kagomé model system, jarosite, and a hyperkagomé system in gadolinium gallium garnet is presented.

2.1 Magnetism

The fundamental object in magnetism is the magnetic moment. This can be defined with a current loop. If there is current I around an area $d\mathbf{S}$ then the magnetic moment induced will be $d\boldsymbol{\mu}$

$$d\boldsymbol{\mu} = I d\mathbf{S}. \tag{2.1}$$

The magnetic moment points perpendicular to the plane of the loop and can therefore be parallel or antiparallel to the angular momentum of the charge going around the loop.
If there is current in a bigger loop the total magnetic moment will be equivalent to the sum of all the infinitesimal loops within it. All the currents from neighbouring infinitesimal loops will cancel leaving only the current running around the perimeter of the loop. Thus the total magnetic momentum is [8]

$$\boldsymbol{\mu} = \int d\boldsymbol{\mu} = I \int d\mathbf{S}. \tag{2.2}$$

Since a current loop is made from electrons moving and electrons have mass and thus angular momentum, there is angular momentum associated with the magnetic moment. Thus we can write

$$\boldsymbol{\mu} = \gamma \mathbf{L}, \tag{2.3}$$

where $\gamma = -g\mu_B/\hbar$ is the gyromagnetic ratio and $\mathbf{L}$ is the angular momentum of the electron.
Let us consider a magnetic moment in a magnetic field $\mathbf{B}$. The energy of the magnetic moment, given by

$$E = -\boldsymbol{\mu} \cdot \mathbf{B}, \tag{2.4}$$

will be minimised when the moment is parallel to the magnetic field. This means that there will be a torque on the magnetic moment and using Eq. 2.2 the equation of motion is

$$\frac{\mathrm{d}\boldsymbol{\mu}}{\mathrm{d}t} = \gamma \boldsymbol{\mu} \times \mathbf{B}. \tag{2.5}$$

Since the change in $\hat{\mu}$ is perpendicular to both $\hat{\mu}$ and $\mathbf{B}$ the magnetic moment will precess around $\mathbf{B}$. The frequency of precession can be shown to be

$$\omega_L = \gamma B. \tag{2.6}$$

This is known as the Larmor precession frequency [8].

A useful term when describing magnetism and magnetic materials is the magnetisation $\mathbf{M}$. This is defined as the magnetic moment per unit volume and is linearly proportional to the applied magnetic field for small field values

$$\mathbf{M} = \chi \mathbf{H}, \tag{2.7}$$

where $\mathbf{B} = \mu_0(\mathbf{H} + \mathbf{M})$, μ_0 is the vacuum permeability, and χ is the magnetic susceptibility. The susceptibility tells how an applied magnetic field changes the magnetisation.

If the material has a positive susceptibility it is paramagnetic, so that an applied magnetic field induces a magnetisation which aligns parallel with the applied field. If the susceptibility is negative the material is dominated by diamagnetism, which means the induced magnetisation is opposite of the applied field. All materials show some degree of diamagnetism. Even though an increase in magnetic field will tend to line up the spins, an increase in temperature will randomise them. The magnetisation of a magnetic material depends on B/T. If we look at paramagnetism semiclassically, that is ignoring that magnetic moments can only point in certain directions due to quantisation we find that the average magnetic moment is

$$\frac{\langle \mu_z \rangle}{\mu} = L(y) = \coth(y) - \frac{1}{y}, \tag{2.8}$$

where $y = \mu B/k_B T$. This is known as the Langevin function [8].

2.2 Magnetic interactions

There are multiple ways for magnetic moments to interact and potentially form long-range order.
The most common interaction between magnetic moments is the exchange interaction. This interaction is a form of electrostatic interaction, that arises because electrons with the same sign charge cost energy when they are close together and save energy when they are apart. To illustrate this interaction we will calculate it for two spins and then generalise to crystals with a macroscopic number of spins.

For two electrons the overall wave function must be antisymmetric so the spin part of the function must be either an antisymmetric singlet state χ_S or a symmetric triplet state χ_T. Thus the collective wave functions for the singlet and the triplet states are [8]

$$\Psi_S = \frac{1}{\sqrt{2}} \left[\psi_a(\mathbf{r}_1)\psi_b(\mathbf{r}_2) + \psi_a(\mathbf{r}_2)\psi_b(\mathbf{r}_1)\right] \chi_S \tag{2.9}$$

$$\Psi_T = \frac{1}{\sqrt{2}} \left[\psi_a(\mathbf{r}_1)\psi_b(\mathbf{r}_2) - \psi_a(\mathbf{r}_2)\psi_b(\mathbf{r}_1)\right] \chi_T, \tag{2.10}$$

where ψ_a and ψ_b describe the states of the first and second electron respectively.
By looking at the energy difference between the two states it can be shown that

$$\mathcal{H} = \frac{1}{4}(E_S + 3E_T) - (E_S - E_T)\mathbf{s}_1 \cdot \mathbf{s}_2, \tag{2.11}$$

where E_S is the energy of the singlet state and E_T is the energy of the triplet state. This energy difference stems from the previously mentioned electrostatic interactions.
The constant term is unimportant and can be absorbed into other constant energy terms. The interesting part of this is the spin-dependent term. If we define the exchange constant J by

$$J = \frac{E_S - E_T}{2}. \tag{2.12}$$

We can write the Hamiltonian as

$$\mathcal{H}_{spin} = -2J\mathbf{s}_1 \cdot \mathbf{s}_2. \tag{2.13}$$

Writing out the energy difference using wave functions, we confirm that the exchange interaction does stem from overlap in wave functions [8]

$$E_S - E_T = 2 \int \psi_a^*(\mathbf{r}_1)\psi_b^*(\mathbf{r}_2)\mathcal{H}\psi_a(\mathbf{r}_2)\psi_b(\mathbf{r}_1)\mathrm{d}\mathbf{r}_1\mathrm{d}\mathbf{r}_2. \tag{2.14}$$

Generalising this to a many-body system is complicated, but this derivation motivates the Heisenberg Hamiltonian written as a sum of pairwise interactions

$$\mathcal{H} = -\sum_{i,j} J_{i,j}\mathbf{s}_i \cdot \mathbf{s}_j, \tag{2.15}$$

where $J_{i,j}$ is the exchange constant between the i'th and the j'th spin. It is common for the coupling to the nearest neighbour to be stronger than the coupling to further neighbours, due to the electrostatic interaction being strongest when the distances between interacting particles are small. In this case everything aside from nearest neighbours can be neglected and the Hamiltonian simplifies to

$$\mathcal{H} = -2J\sum_{\langle i,j \rangle} \mathbf{s}_i \cdot \mathbf{s}_j, \tag{2.16}$$

where $\langle i, j \rangle$ denotes the sum over nearest neighbours and J is assumed to be constant through the system. Exchange interactions can also happen via non-magnetic ions like oxygen. This is known as superexchange.

Another common interaction is the interaction between a spin $\mathbf{s}$ and an external magnetic field $\mathbf{B}$. This is known as the Zeeman interaction and is described by

$$\mathcal{H}_Z = -g\mu_B \mathbf{s} \cdot \mathbf{B}, \tag{2.17}$$

where g is the electron g-factor, and μ_B is the Bohr magneton. If we have several electrons in an external field we get

$$\mathcal{H}_Z = -g\mu_B \sum_j \mathbf{s}_j \cdot \mathbf{B}. \tag{2.18}$$

The classical solution to this Hamiltonian is seen in Eq. 2.5.

2.2.1 Single-ion anisotropy

Anisotropy is an effect causing the magnetic moment to prefer to lie along a specific plane or axis in space. This leads to anisotropic materials having different magnetic properties depending on direction. In most magnetically anisotropic materials there is an axis along which it is easier to magnetise the material. This is known as the easy axis. There can be several reasons why a material is anisotropic, but the most common is crystal field effects.
The Hamiltonian for anisotropy axis $\hat{v}$ can be written

$$\mathcal{H}_{anis} = -\frac{D}{g\mu_B} \sum_i (\mathbf{s}_i \cdot \hat{v})^2 = B_{anis} \sum_i (\mathbf{s}_i \cdot \hat{v})^2, \tag{2.19}$$

where D is the strength of the anisotropy and $\hat{v}$ is a unit vector indicating the direction of the easy axis or the vector defining the easy plane depending on the sign of D. If $D > 0$ the energy is minimised when the spins lie along $\hat{v}$, and if $D < 0$ the energy is minimised when the spins are in the plane perpendicular to $\hat{v}$. If the easy axis anisotropy becomes very large the spins become Ising spins. This means that the spins are confined along the axis, and can only have two directions.
Another way to write the Hamiltonian is describing the anisotropy axis with a matrix κ

$$\mathcal{H}_{anis} = -\frac{D}{g\mu_B} \sum_i \mathbf{s}_i^T \kappa \mathbf{s}_i = B_{anis} \sum_i \mathbf{s}_i^T \kappa \mathbf{s}_i. \tag{2.20}$$

The matrix is related to $\hat{v}$ by

$$\kappa = \begin{pmatrix} v_x v_x & v_x v_y & v_x v_z \\ v_y v_x & v_y v_y & v_y v_z \\ v_z v_x & v_z v_y & v_z v_z \end{pmatrix}. \tag{2.21}$$

2.2.2 Dzyaloshinskii-Moriya interaction

The Dzyaloshinskii-Moriya (DM) interaction or anisotropic exchange interaction is the interaction between the excited state of one ion and the ground state of another ion. When acting between two spins $\mathbf{s}_1$ and $\mathbf{s}_2$ it leads to a term in the Hamiltonian equal to

$$\mathcal{H}_{DM} = \mathbf{D}_{DM} \cdot (\mathbf{s}_1 \times \mathbf{s}_2), \tag{2.22}$$

where $\mathbf{D}_{DM}$ is a vector that will lie either parallel or perpendicular to the line connecting the two spins. This commonly occurs in antiferromagnets, with the effect of canting the spins and introducing a weak ferromagnetic moment.

2.3 Magnetic order

In the previous section different types of magnetic interactions were described. These interactions lead to different possible magnetic ground states in materials. In this section we will describe some of the different possible ground states and the interactions that cause them.

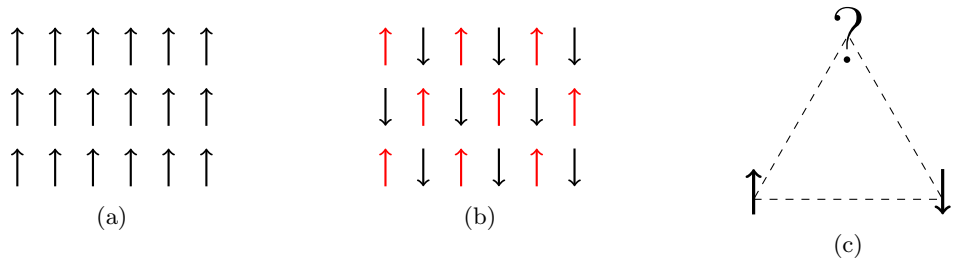

Figure 2.1: An example of ferromagnetism, antiferromagnetism and a frustrated system.

Ferromagnetism (FM) is the effect of spontaneous magnetisation even in the absence of an applied field, which means that all the magnetic moments align along the same direction as in Figure 2.1a. This is due to a positive exchange constant $J > 0$ which means the energy is minimised when the spins are parallel. If the temperature is increased the fluctuations will gradually destroy the magnetisation and above a critical temperature known as the Curie temperature T_{CW}, the order will be destroyed. The Curie temperature is defined by

$$T_{CW} = \frac{n\lambda\mu_{eff}^2}{3k_B}, \tag{2.23}$$

where λ is a constant that parametrizes the molecular field as a function of magnetisation, μ_{eff} is the value of the effective moment, and n is the number of spins in the lattice.
The ordering parameter for a ferromagnet is the magnetisation which is proportional to the sum of the spins

$$m_{FM} = \langle \mathbf{s}_i \rangle = \frac{1}{N} \sum \mathbf{s}_i. \tag{2.24}$$

Here N is the number of spins on the lattice.
The magnetic susceptibility of a ferromagnet above the critical temperature is

$$\chi \propto \frac{1}{T - T_{CW}}, \tag{2.25}$$

which is known as the Curie Weiss law.

Antiferromagnetism (AFM) stems from a negative exchange interaction, $J < 0$ which means the energy is minimised when spins are antiparallel to their neighbours. These materials can classically be described as having two interpenetrating sublattices, one where all the spins point up and one where all the spins point down, see example in Figure 2.1b. Similarly to the ferromagnetic materials order will be destroyed above a critical temperature known as the Néel temperature defined as

$$T_N = \frac{n|\lambda|\mu_{eff}^2}{3k_B}. \tag{2.26}$$

The ordering parameter for an antiferromagnet is the difference between the number of individual spins on each sublattice [8].

$$m_{AFM} = \frac{1}{N}\left(\sum_{i\in A}\mathbf{s}_i - \sum_{j\in B}\mathbf{s}_j\right), \tag{2.27}$$

where N is the total number of spins on the lattice, s is the spin value, and the two sublattices are denoted by A and B respectively.
The magnetic susceptibility of an antiferromagnet above the critical temperature can be fitted to a Curie-Weiss dependence

$$\chi \propto \frac{1}{T-\theta}, \tag{2.28}$$

where θ is the Weiss temperature. If $\theta > 0$ the material is a ferromagnet and if $\theta < 0$ the material is an antiferromagnet. If $\theta = 0$ the material is a paramagnet.

Frustrated magnetism occurs when a system has competing interactions so the energy cannot be minimised for all spins. This often leads to a degenerate ground state with many possible variations.
An example of this is the Ising model for a triangular lattice with antiferromagnetic spins, see Figure 2.1c. In the Ising model the spins have two possible directions, up and down. This means the three spins in the triangle can only be parallel or antiparallel to each other. If two spins are antiparallel with each other, then the third spin cannot satisfy the requirement of being antiparallel to both neighbouring spins. Whatever choice is made one of the two neighbours will be aligned with the third spin and thus does not get its energy minimised.

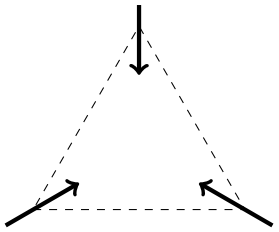

Figure 2.2

In the Heisenberg model, where the spins can point in any direction, the spins would end up with 120° to each other. An example of this is shown in Figure 2.2. This state is degenerate. Keeping the top spin fixed, the two other spins can rotate an arbitrary angle out of the plane while still maintaining an angle of 120 degrees with the other spins.

2.4 Spin dynamics

Disregarding quantum mechanics, a magnet may be perfectly ordered at $T = 0$ but at non-zero temperatures this order is disrupted by excitations. A common type of excitation is the spin wave, which can be produced at a small energy cost. These are characterised by a dispersion relation, which describes how the frequency of the wave ω relates to the wave vector $\mathbf{q}$.
To describe these excitations it is useful to look at an equation of motion for the spins. In this section the general equation of motion will be presented and we will derive dispersion relations for simple spin systems like FM and AFM one dimensional spin chains as well as two and three spins with AFM interactions.

2.4.1 Equation of motion

To find the equation of motion we need to start with the Hamiltonian for the system. We want to describe a system with N spins, nearest neighbour interaction J, Zeeman interaction, and single ion anisotropy D. Including this the Hamiltonian for the i'th spin is

$$H_i = 2J\sum_j \mathbf{s}_i \cdot \mathbf{s}_j - D(\mathbf{s}_i \cdot \hat{v})^2 + g\mu_B \mathbf{s}_i \cdot \mathbf{B} \tag{2.29}$$

$$= -g\mu_B \mathbf{s}_i \cdot \left(\frac{2J}{g\mu_B}\sum_j \mathbf{s}_j - \frac{D}{g\mu_B}(\mathbf{s}_i \cdot \hat{v})^2 + \mathbf{B} \right) \tag{2.30}$$

$$= -g\mu_B \mathbf{s}_i \cdot \tilde{\mathbf{B}}, \tag{2.31}$$

Where the neighbouring spins, the anisotropy and the external magnetic field has been combined into an effective field in the mean field approximation.
The effective magnetic field is given by

$$\tilde{\mathbf{B}} = -\frac{2Js}{g\mu_B}\sum_j \mathbf{s}_j - D\begin{pmatrix} v_x v_x & v_x v_y & v_x v_z \\ v_y v_x & v_y v_y & v_y v_z \\ v_z v_x & v_z v_y & v_z v_z \end{pmatrix}\begin{pmatrix} s_i^x \\ s_i^y \\ s_i^z \end{pmatrix} + \mathbf{B} \tag{2.32}$$

$$= \mathbf{B}_X - \mathbf{B}_{anis} + \mathbf{B}. \tag{2.33}$$

Where D is the anisotropy strength and v_x, v_y, v_z determine the direction of the anisotropy axis. To understand the definition of the anisotropy axis it is important to understand that the anisotropy does not have a direction, it can only be defined along an axis. If the anisotropy is positive, this is the easy axis and if the anisotropy is negative, the plane perpendicular to this axis is the easy plane. This means the direction of the anisotropy has to be given by a matrix where the diagonal represents the x, y, and z-axes and the off-diagonal is used to denote directions not directly along one of the three axes.
When finding the equation of motion a semiclassical approximation is used where the spins are vectors and can point in any direction. This approximation is best for large spins, $s \gg 1$, but is valid even for s=1/2 for 3D-systems [9]. The equation of motion is derived with the use of Ehrenfest's theorem

$$-i\hbar\frac{\mathrm{d}\mathbf{s}_i}{\mathrm{d}t} = [\hat{H}, \mathbf{s}_i]. \tag{2.34}$$

The commutators of the spin operators are

$$[s_i^x, s_i^y] = i\hbar s_i^z \delta_{ij}, \qquad [s_i^y, s_i^z] = i\hbar s_i^x \delta_{ij}, \qquad [s_i^z, s_i^x] = i\hbar s_i^y \delta_{ij}. \tag{2.35}$$

Using these equations and Eq. 2.29 the equation of motion is found the be

$$-i\hbar\frac{\mathrm{d}\mathbf{s}_i}{\mathrm{d}t} = \gamma \mathbf{s}_i \times \tilde{\mathbf{B}}. \tag{2.36}$$

A detailed derivation of the equation of motion for exchange interaction and external magnetic field can be found in Jacobsen's thesis [10] and a derivation of the single-ion anisotropy field is found in Appendix A.

2.4.2 Spin waves

Spin wave theory is a theory where one starts from a ground state where all spins are aligned and describes excitations as a collection of independent spin waves. In other words the theory is an expansion of small deviations from the ground state. This is a useful approximation for low temperature states, where the amplitudes of the spin waves are small and there is a negligible interaction between them [11]. Looking at just one spin wave, we see the spins precessing around the vertical axis as in Figure 2.3.
It is possible to derive a dispersion relation for spin waves on a simple lattice. In the following we will derive the dispersion relation for a one dimensional ferromagnetic spin chain and for a one dimensional antiferromagnetic spin chain.

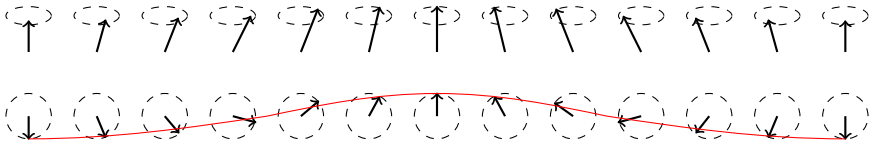

Figure 2.3: The excited state of a one dimensional ferromagnetic spin chain and the red line shows the spin wave. From E. Lenander [12].

Ferromagnetic spin wave theory

We derive the dispersion for a semi-classical spin chain. Starting with the equation of motion for the i'th spin in the chain in an external magnetic field, ignoring anisotropy

$$\frac{\mathrm{d}\mathbf{s}_i}{\mathrm{d}t} = \frac{1}{\hbar}\mathbf{s}_i \times \left(2\sum_j J_{ij}\mathbf{s}_j - g\mu_B \mathbf{B} \right). \tag{2.37}$$

This can be simplified by summing over nearest neighbours. We define the ground states as $\mathbf{s} = s\hat{z}$ with the magnetic field $\mathbf{B} = B\hat{z}$. Furthermore we know that the spin wave state is a small pertubation away from the ground state, so we can write it as

$$\mathbf{s}_i = s\hat{z} + \delta\mathbf{s}_i, \tag{2.38}$$

where δ is small.
Inserting this into the equation of motion we get

$$\hbar\frac{\mathrm{d}}{\mathrm{d}t}(s\hat{z} + \delta\mathbf{s}_i) = (s\hat{z} + \delta\mathbf{s}_i) \times (4Js\hat{z} + 2J(\delta\mathbf{s}_{i-1} + \delta\mathbf{s}_{i+1}) - g\mu_B B\hat{z}) \tag{2.39}$$

$$= s\hat{z} \times 2J(\delta\mathbf{s}_{i-1} + \delta\mathbf{s}_{i+1}) + \delta\mathbf{s}_i \times (4Js\hat{z} - g\mu_B B\hat{z}). \tag{2.40}$$

We have ignored the $\delta\mathbf{s}_i \times (\delta\mathbf{s}_{i-1} + \delta\mathbf{s}_{i+1})$ term as it is second order in δ.
Wave-like solutions are assumed for $\delta\mathbf{s}_i^x$, $\delta\mathbf{s}_i^y$ and $\delta\mathbf{s}_i^z = 0$

$$\delta s_i^x = A_x e^{i\omega t - i\mathbf{k}\cdot\mathbf{r}} \tag{2.41}$$

$$\delta s_i^y = A_y e^{i\omega t - i\mathbf{k}\cdot\mathbf{r}}. \tag{2.42}$$

The chain is taken to be in the x-direction which means $\mathbf{r} = ia\hat{x}$ where i is the spin index and a is the distance between the spins. This gives us $\mathbf{k}\cdot\mathbf{r} = ik_x a$.

After using this we find equations for the x and y components of the spin wave

$$i\hbar\omega A_x = \left(4Js(1-\cos(k_x a)) + g\mu_B B\right) A_y, \tag{2.43}$$
$$i\hbar\omega A_y = -\left(4Js(1-\cos(k_x a)) + g\mu_B B\right) A_x. \tag{2.44}$$

Solving for ω results in

$$\hbar\omega_q = 4Js(1-\cos(qa)) + g\mu_B B. \tag{2.45}$$

It can be readily shown that when adding single ion anisotropy with an easy axis in the z-direction the dispersion will be [7]

$$\hbar\omega_q = 4Js(1-\cos(qa)) + g\mu_B B - g\mu_B B_{anis}. \tag{2.46}$$

The dispersions for varying **B**-fields can be seen in Figure 2.4. Here we see that the effect of the **B**-field on the dispersion is to move the dispersion in energy. The anisotropy value has the same effect.

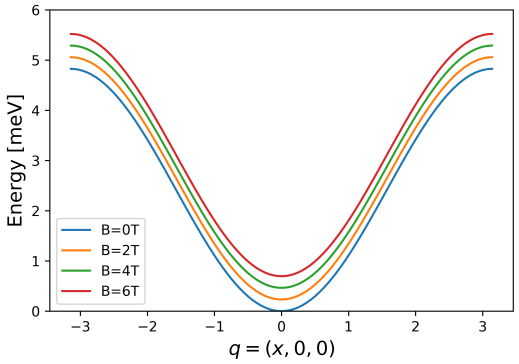

Figure 2.4: The dispersion of a spinwave with $J = 2$K, $s = 7/2$, $\mathbf{B}_{anis} = 0$ and various **B**-field strengths.

Antiferromagnetic spin wave theory

To find the dispersion of an antiferromagnetic one dimensional spin chain we follow the derivation in Yosida [11]. We start by deriving the general spin wave dispersion for an antiferromagnet. The equations of motion for the two spins in the sublattices are

$$-i\hbar\frac{\mathrm{d}\mathbf{s}_j}{\mathrm{d}t} = i(\tilde{\mathbf{B}}_j \times \mathbf{s}_j), \tag{2.47}$$
$$-i\hbar\frac{\mathrm{d}\mathbf{s}_l}{\mathrm{d}t} = i(\tilde{\mathbf{B}}_l \times \mathbf{s}_l). \tag{2.48}$$

Here j represent points on one sublattice and l represents points on the other sublattice. The effective fields $\tilde{\mathbf{B}}_j$ and $\tilde{\mathbf{B}}_l$ are given by

$$\tilde{\mathbf{B}}_j = 2\sum_l J_{jl}\mathbf{s}_l + g\mu_B B\hat{z} + DS_{jz}\hat{z}, \tag{2.49}$$
$$\tilde{\mathbf{B}}_l = 2\sum_j J_{jl}\mathbf{s}_j + g\mu_B B\hat{z} + DS_{jz}\hat{z}. \tag{2.50}$$

The easy axis is taken to be the z-axis, and the external magnetic field also aligns with the z-axis.
We assume the spins to be in the ground state with a small perturbation. This means they are pointing primarily in the z-direction with the perturbation in the xy-plane

$$\mathbf{s}_j = s\hat{z} + \delta\mathbf{s}_j, \qquad \mathbf{s}_l = -s\hat{z} + \delta\mathbf{s}_l. \tag{2.51}$$

Inserting this into the equation of motion and keeping only first order terms in $\delta\mathbf{s}_j$ and $\delta\mathbf{s}_l$

$$-\hbar\frac{\mathrm{d}}{\mathrm{d}t}\delta\mathbf{s}_j = (-2\sum_l J_{jl}s\hat{z} + g\mu_B B\hat{z} + DS\hat{z}) \times \delta\mathbf{s}_j + 2\sum_l J_{jl}\delta\mathbf{s}_j \times s\hat{z}, \tag{2.52}$$

$$-\hbar\frac{\mathrm{d}}{\mathrm{d}t}\delta\mathbf{s}_l = (2\sum_j J_{jl}s\hat{z} + g\mu_B B\hat{z} - DS\hat{z}) \times \delta\mathbf{s}_j - 2\sum_j J_{jl}\delta\mathbf{s}_l \times s\hat{z}. \tag{2.53}$$

Now that we have two coupled differential equations, we need to make a linear transformation to uncouple them so they can be solved separately. The Fourier transformation is introduced

$$\mathbf{A}_\mathbf{q} = \left(\frac{2}{N}\right)^{1/2}\sum_j \mathrm{e}^{-i\mathbf{q}\cdot\mathbf{r}_j}\delta\mathbf{s}_j, \tag{2.54}$$

$$\mathbf{B}_\mathbf{q} = \left(\frac{2}{N}\right)^{1/2}\sum_l \mathrm{e}^{-i\mathbf{q}\cdot\mathbf{r}_l}\delta\mathbf{s}_l. \tag{2.55}$$

The equations of motion for $\mathbf{A}_\mathbf{q}$ and $\mathbf{B}_\mathbf{q}$ are:

$$-\hbar\frac{\mathrm{d}}{\mathrm{d}t}\mathbf{A}_\mathbf{q} = (-2\sum_l J_{jl}s\hat{z} + g\mu_B B\hat{z} + DS\hat{z}) \times \mathbf{A}_\mathbf{q} + 2\sum_j J_{jl}\mathrm{e}^{-i\mathbf{q}\cdot(\mathbf{r}_j-\mathbf{r}_l)}\mathbf{B}_\mathbf{q} \times s\hat{z}, \tag{2.56}$$

$$-\hbar\frac{\mathrm{d}}{\mathrm{d}t}\mathbf{B}_\mathbf{q} = (2\sum_j J_{jl}s\hat{z} + g\mu_B B\hat{z} - DS\hat{z}) \times \mathbf{B}_\mathbf{q} - 2\sum_l J_{jl}\mathrm{e}^{-i\mathbf{q}\cdot(\mathbf{r}_l-\mathbf{r}_j)}\mathbf{A}_\mathbf{q} \times s\hat{z}. \tag{2.57}$$

We assume the interaction is only present between nearest neighbour sites. We define a quantity γ_q by

$$\sum_j J_{jl}\mathrm{e}^{-i\mathbf{q}\cdot(\mathbf{r}_j-\mathbf{r}_l)} = zJ\gamma_q, \tag{2.58}$$

where z is the number of nearest neighbours and γ_q is the Fourier transform of the exchange term.
By adding i times the y-component to the x-component of the equations and introducing $A_{q+} = A_{qx} + iA_{qy}$ and $B_{q+} = B_{qx} + iB_{qy}$ we get

$$\hbar\frac{\mathrm{d}}{\mathrm{d}t}A_{q+} = -i\left[(-2Jzs + g\mu_B B + DS)A_{q+} - 2Jzs\gamma_q B_{q+}\right], \tag{2.59}$$

$$\hbar\frac{\mathrm{d}}{\mathrm{d}t}B_{q+} = -i\left[(2Jzs + g\mu_B B - DS)B_{q+} + 2Jzs\gamma_q A_{q+}\right]. \tag{2.60}$$

If we take the time dependency of A_q and B_q to be $\mathrm{e}^{-i\omega_q t}$ the relation determining the frequency ω_q is

$$\begin{vmatrix} \hbar\omega_q - (2Jzs - g\mu_B B - Ds) & -2Jzs\gamma_q \\ 2Jsz\gamma_q & \hbar\omega_q + (2Jzs - g\mu_B B - Ds) \end{vmatrix} = 0 \tag{2.61}$$

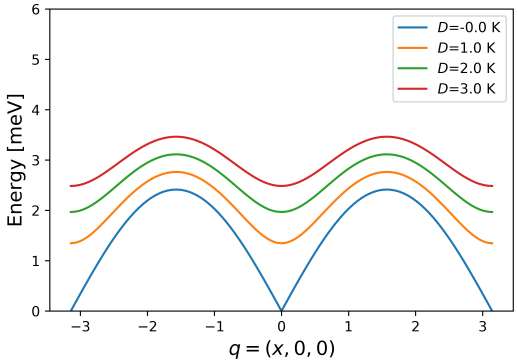

Figure 2.5: The dispersion of an antiferromagnetic spinwave with $J = 2$K, $s = 7/2$, $\mathbf{B} = 0$ and various values of D.

The solutions are

$$\hbar|\omega_q^{\pm}| = \sqrt{(2Jzs)^2(1-\gamma_q^2) + 4|J|zs^2D + s^2D^2} \pm g\mu_B B. \tag{2.62}$$

For a one dimensional chain it becomes

$$\hbar|\omega_q^{\pm}| = \sqrt{(4Js)^2(1-\cos(qa)^2) + 8|J|s^2D + s^2D^2} \pm g\mu_B B, \tag{2.63}$$

where a is the distance between the spins in the chain.
The dispersion relation can be seen plotted in Figure 2.5, with different values of D. We can see that changing the anisotropy changes both the shape and the energy of the dispersion. Changing the value of the magnetic field $\mathbf{B}$ changes the energy of the dispersion and splits into two bands.

2.4.3 Zero mode

The zero mode excitation is a dispersionless excitation found in some frustrated materials. These are associated with the degeneracy of the ground state, specifically the spin configurations where certain spins can be rotated around a specific axis without any energy cost [13]. This dispersionless excitation strongly affects the lower temperature thermodynamic behaviour and leads to a persistence of spin fluctuations down to zero temperature. We here show a few different manifestations of zero modes.

Rotor mode

The rotor mode is a version of the zero mode found in nanoparticles with antiferromagnetic order and two sublattices [14]. Because of the exchange interaction the spins are at equilibrium when antiparallel to each other. If they are canted away from this position they will begin to rotate as illustrated in Figure 2.6. The frequency of rotation can be derived from the equations of motion.
We start with the spin vectors

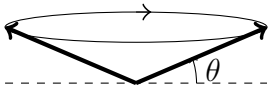

Figure 2.6

$$\mathbf{s}_0 = (\cos(\theta)\cos(\omega t), \sin(\theta), \cos(\theta)\sin(\omega t))^{\dagger}, \tag{2.64}$$

$$\mathbf{s}_1 = (-\cos(\theta)\cos(\omega t), \sin(\theta), -\cos(\theta)\sin(\omega t))^{\dagger}. \tag{2.65}$$

We take the equation of motion from Eq. 2.36 with the effective field determined by Eq. 2.32. We have zero external field and no anisotropy, so inserting this we get

$$\frac{\mathrm{d}\mathbf{s}_0}{\mathrm{d}t} = \gamma \mathbf{s}_0 \times \left(\frac{2J}{g\mu_B} \mathbf{s}_1 \right). \tag{2.66}$$

The spins will be constant in the y-direction and rotate with a constant frequency in the xz-plane so we can set $t = 0$ without loss of generality

$$\begin{pmatrix} 0 \\ 0 \\ \omega \cos(\theta) \end{pmatrix} = \frac{2Js}{\hbar} \begin{pmatrix} 0 \\ 0 \\ 2\cos(\theta)\sin(\theta) \end{pmatrix}. \tag{2.67}$$

Taking the z-component and solving for ω

$$\omega_{rot}(T) = \frac{4Js}{\hbar} \sin(\theta) \tag{2.68}$$

The mode can be thermally activated.

Zero mode for three spins

There is also a version of the zero mode found in three spin systems, similar to the rotor mode for two spins. This mode can be seen for three antiferromagnetic spins arranged in a triangle. If two spins are canted away from equilibrium, they will begin to rotate with a well defined frequency.
The derivation of this frequency is similar to the derivation of the rotor mode. The main differences are the equilibrium positions of the spins are at 120° to each other and there is a third spin $\mathbf{s}_2 = (0, -1, 0)^\dagger$ which has a constant effect on the two other spins. Thus, in the absence of anisotropies the equation of motion becomes

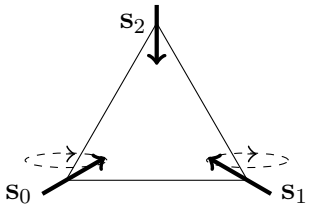

Figure 2.7

$$\frac{\mathrm{d}\mathbf{s}_0}{\mathrm{d}t} = \gamma \mathbf{s}_0 \times \left(\frac{2J}{g\mu_B} (\mathbf{s}_1 + \mathbf{s}_2) \right). \tag{2.69}$$

Using the same method as for the two-spin rotor mode we find

$$\omega = \frac{2Js}{\hbar} (2\sin(\theta) - 1), \tag{2.70}$$

where θ is the angle with horizontal, so that the spins are in equilibrium when $\theta = 30°$. It follows that this mode can be activated thermally just like the rotor mode.

Zero mode in kagomé lattice

The zero mode can also be found in a kagomé lattice. This is the case when six spins forming a ring all rotate, and the spins surrounding them are stationary as illustrated in Figure 2.8. This is one of the three possible Néel states of the kagomé lattice [15]. As with the previous two systems, we can find the equation for the frequency of the zero mode based on the canting angle θ of the spins. We start with the same spin positions as for the triangle but each shows up twice, as all the moving spins have four neighbours. Then the derivation continues as before, and we get the dispersion

$$\omega = \frac{4Js}{\hbar}(2\sin(\theta) - 1). \tag{2.71}$$

This is the same dispersion relation as for the triangle, except for a factor two. Intuitively this makes sense as all the rotating spins are part of two triangles.

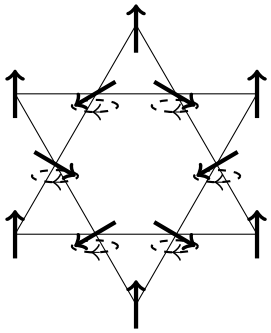

Figure 2.8

2.5 Experiments on frustrated antiferromagnets

The previous sections derive results for systems with two specific excitations, spin waves and the zero mode excitation, but these might not always be enough to describe the dynamics of a given system. This is where simulations come in. With the simulation program I and many others have helped develop, it is possible to replicate all the dynamics of a system with the correct initial conditions. In this thesis we work on gaining a better understanding of complex frustrated systems like the kagomé and hyperkagomé lattices.
This section is about the research on physical realisations of the kagomé lattice and the hyperkagomé lattice to better understand the data that we may try to replicate and explain with simulations.

2.5.1 Jarosite

The kagomé antiferromagnet is an interesting and much studied system given its frustrated nature and lack of long-range order. Several physical realisations of the kagomé lattice exists, and one of the most studied groups is the jarosite family of magnets. Jarosites are a subgroup of the alunite mineral family, which has the chemical composition $AM_3(SO_4)_3(OH)_6$ with A = Na^+, K^+, Ag^+, Rb^+, $NH_4{}^+$, H_3O^+, $\frac{1}{2}\,Pb^{2+}$ and M = Al^{3+}, Fe^{3+}, V^{3+}, Cr^{3+} [16]. Their lattice is structured with the M-ion forming a kagomé lattice in layers, that interact very little with each other. This makes the structure a good approximation of a 2D kagomé lattice structure.
It has been shown to be a canted antiferromagnet with weak Dzyaloshinskii-Moriya (DM) interaction for most choices of A cations [17]. The magnetism of iron jarosite, containing a s=5/2 Fe^{3+}, has been extensively studied.
Cr-jarosite, $KCr_3(OD)_6(SO_4)_2$, is another less studied example of the kagomé lattice. This is a system with the magnetic moments arising from the magnetic Cr^{3+} ions, and spin value $s = 3/2$. The low spin value makes it sit in a point between classical and quantum spin behaviour [17].

A problem when studying Cr-jarosite, as with other jarosites, is the difficulty in synthesizing pure compounds. This leads to differences in estimations of constants like the Curie-Weiss temperature and the critical temperature for Cr-jarosite. There is a consensus on the qualitative magnetic behaviour, which describes Cr-jarosite as an antiferromagnet with a weak DM-interaction. The DM-interaction leads to the spins canting out of the plane, which for all the layers adds up to a weak ferromagnetic moment [17].

The simple kagomé antiferromagnet has a macroscopic ground state degeneracy which prevents long-range ordering down to T=0, and leads to a large amount of zero-energy excitations or zero modes for the lattice [16]. However in physically realized kagomé lattices there is always additional interactions that cause ordering at finite temperatures. For the jarosites this is the DM-interaction. This leads to spin waves below the critical temperature and a spin wave gap due to the broken rotational symmetry [17]. Because the kagomé lattice is a frustrated system there will be fluctuations between the degenerate ground states, which has the appearance of low-energy excitations with broad linewidths in $\mathbf{q}$ and energy. The zero-energy mode may still be present in jarosites, but the DM-interaction will lift the zero-mode to finite energies.
The dynamics of Fe-jarosite $KFe_3(SO_4)_3(OH)_6$ have been investigated with neutron spectroscopy.

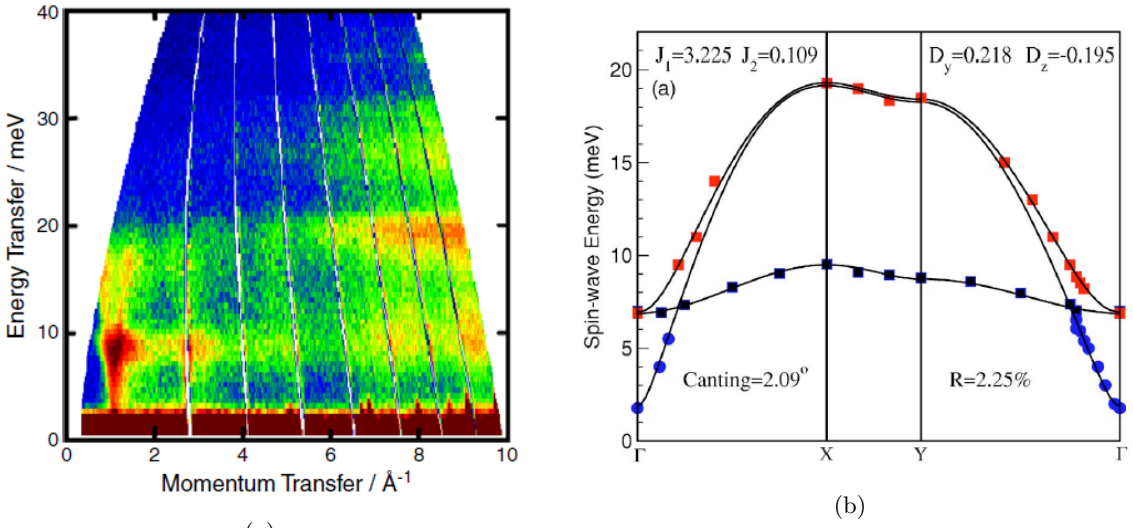

(a) (b)

Figure 2.9: (a) $\chi''(\mathbf{q},\omega)$ for deuterated Fe-jarosite powder, measured using time of flight spectroscopy at 5 K. From Coomer et al. [18]. (b) Single-crystal spin wave spectrum of Fe-jarosite measured using neutron spectroscopy (circles and squares) from Matan et al. [19], and the best-fit theoretical spin wave dispersion. From Yildirim et al. [15].

Coomer et al. [18] measured the imaginary susceptibility $\chi''(\mathbf{q},\omega)$ for deuterated Fe-jarosite powder, shown in Figure 2.9a. The imaginary susceptibility is related to the dynamical structure factor via $\chi''(\mathbf{q},\omega) = S(\mathbf{q},\omega)/(1+n_B(\omega))$ where the Bose population factor is $n_B(\omega) = 1/(\exp(\hbar\omega/k_BT)-1)$. The data shows spin wave excitations emerging from $q \approx 1\text{Å}^{-1}$ and 3Å^{-1} with a bandwidth of about 20 meV. A flat mode with increased intensity is present around 8 meV and phonon excitations are seen above $q \approx 6\text{Å}^{-1}$ with energies in the range 5-35 meV.
Matan et al. [19] used neutron spectroscopy on a single crystal to investigate the spin waves

in more detail. They arrived at a spin wave dispersion seen in Figure 2.9b showing three gapped spin waves, one of which is the 8 meV mode. Yildirim et al. performed detailed spin wave calculations assuming a Hamiltonian with nearest neighbour and next nearest neighbour exchange interactions J_1 and J_2 as well as a DM-interactions $\mathbf{D}_{DM}^{ij}$. They arrived at a model with $J_1 = 3.225$ meV, $J_2 = 0.109$ meV, $D_{DM}^{y} = 0.218$ meV, $D_{DM}^{z} = -0.195$ meV and confirmed that the DM-interaction is the better model for the spin wave gap than a single-ion anisotropy.

2.5.2 Frustrated garnets

The hyperkagomé lattice is a three-dimensional lattice of corner sharing triangles. The way the triangles are connected means that ten-spin loops form in the lattice, this is analogous to the kagomé lattice where six-spin loops form. The zero mode can propagate in these loops. An example of a hyperkagomé compound is $Gd_3Ga_5O_{12}$ (GGG). It has a lattice consisting of two interpenetrating hyperkagomé sublattices as shown in Figure 2.10. GGG has antiferromagnetic near-neighbour interactions of strength $J_1 = 107$ mK and an anisotropic orientation of the spins that show they prefer orienting in their local xy-plane [20]. The spins show short-range order below the Curie-Weiss temperature, and longer range correlations develop at the lowest temperatures [21]. It was found that the dipolar interaction plays a role in this ordering [22].

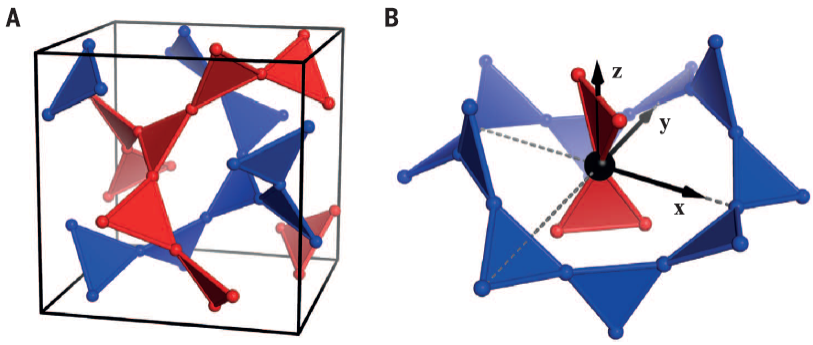

Figure 2.10: (A) Crystal structure of GGG showing only Gd^{3+} ions. The two sublattices are coloured red and blue. (B) The local environment of the ions, showing the local coordinate system and the surrounding ten ion loop. Taken from Paddison et al. [20].

Paddison et al. [20] discovered long-range hidden order from the average spin alignment on each ten spin loop, also known as a director. The directors are highly anisotropic and align with their local z-axis, which leads to long-range correlations. This long-range order is a result of the interplay between the antiferromagnetic interactions and the local xy anisotropy of the spins.
The spin dynamics of a powder of GGG were investigated by Deen et al. [23] with the use of inelastic neutron scattering. Figure 2.11 shows the scattering function $S(q, \omega)$ at 0.06K. This shows the elastic line and three excitations labeled INS1, INS2 and INS3. The excitations do not originate from normal spin waves, which means a theoretical description of the excitations is still needed. It can be concluded from the peak-dependence on wave vector transfer q that the peaks do not originate from local vibrational excitations or crystal-field excitations. The integrated intensity of INS3 is well described by the intensity of a singlet-triplet excitation of a dimerized state. The integrated intensity of INS1 follows the behaviour of INS3

closely, but at low and high q the model of a singlet-triplet excitation fails. INS2 has an integrated intensity with a minimum where INS1, and INS3 shows a maximum, which indicates INS2 has a different origin from the other excitations. INS3 further shows a strong temperature dependence in energy position and excitation lifetime, corresponding to the expectations of an optical mode. It is possible that the excitations stem from optical or soft modes with a high-energy mode represented by INS3.
The dispersion of GGG in an applied magnetic field have been reproduced theoretically by d'Ambrumenil et al. [24] using linear spin-wave theory on the ten ion loops. Though the study is carried out in a magnetic field strong enough to create a ferromagnetic ground state, which is very different to the zero-field ground state, the dispersion looks similar. Comparing results suggests that INS1 originates from near dispersionless bands and INS2 consists of multiple dispersions that overlap in reciprocal space. The equivalent of INS3 is not found using spin wave theory, and probably has an entirely different origin.

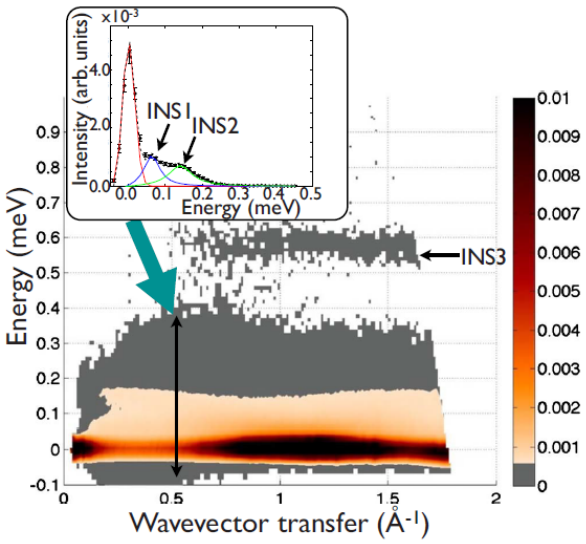

Figure 2.11: The scattering function $S(q, \omega)$ of GGG at 0.06K. Inset is cut at wave vector transfer $q = 0.5\text{Å}^{-1}$ showing the elastic peak and two excitations. Taken from Deen et al. [23].

To learn more about the dynamics of the hyperkagomé lattice we can look at $Gd_3Al_5O_{12}$ (GAG) which is isostructural to GGG. Jacobsen et al. [4] has done an experimental study of the structure and dynamics of GGG and GAG.
Looking at the magnetic structure of GAG they find that antiferromagnetic near-neighbour interactions of strength $J_1 = 186$ mK [22] and a strong local xy anisotropy. They confirm the existence of a long-range director state as in GGG, as the directors in GAG orient along their local z-direction and have weak long-range correlations. Furthermore the excitation spectrum of GAG shows three inelastic peaks INS1, INS2, and INS3. The energies of the excitations are slightly higher than in GGG, which reflects the higher value of J in GAG. The temperature dependence of INS3 is nearly identical to GGG.
On the μeV scale the spins fluctuate with a rate that decreases as $T^{1.5}$, similar to what was found with Mossbauer spectroscopy [25] and muon spin rotation [26]. These fluctuations have no q-dependence which is consistent both with independent spin fluctuations, or with spin diffusion of loops.

A lot of experimental work have been done to describe the rich and complex dynamics of these materials [27] [28], but the theory to describe them is still lacking. The unique ability of the simulations presented here is to replicate the behaviour of the spins in a lattice as if we had a real crystal, placed in a specific temperature and magnetic field. In addition to replicating experimental results we also get data on all of the spin movements, which means we can see specifically what the spins are doing that results in the different excitations, and we can tune different parameters to see how they affect the excitation spectrum.
In this thesis we are interested in the magnetic excitations of GAG shown in Figure 2.12 and furthering our understanding of where they stem from.

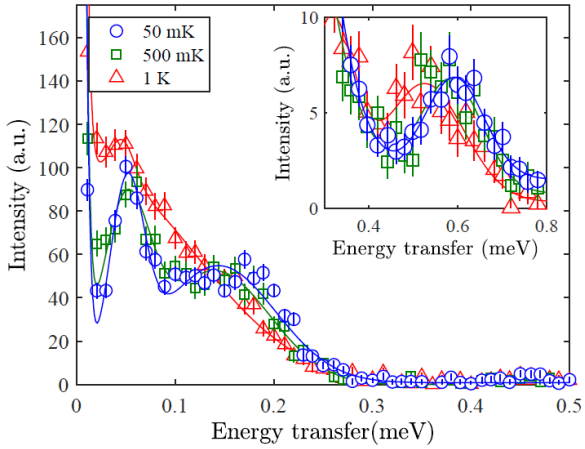

Figure 2.12: Temperature and energy dependence of excitations of GAG found from inelastic neutron scattering on a powder of GAG. Inset shows **q**-integrated intensity of the higher energy excitation. Figure from Jacobsen et al. [4].

Chapter 3

Neutron Scattering

In this chapter we will go through the basics of neutron scattering and derive the equation describing the neutron scattering from magnetic dynamics. The chapter is inspired by the notes by K. Lefmann [7].

3.1 Basic scattering theory

The neutron is a neutral particle with mass $m_N = 1.675 \cdot 10^{-27}$ kg and spin 1/2. Neutrons interact with nuclei and can penetrate materials more deeply than e.g. X-rays, due to being charge neutral. Neutrons can also be moderated to have wavelengths similar to the interatomic distances in materials, and energies similar to the typical excitation energies in solids. The magnetic moment of the neutron means that they are sensitive to magnetic order and magnetic fluctuations of materials. Neutron scattering is therefore a powerful tool to investigate the structure and dynamics of materials. To understand how we start by looking at the flux of a neutron beam. This is defined as

$$\Psi = \frac{\text{number of neutrons impinging on surface area per second}}{\text{surface area perpendicular to neutron beam direction}}, \tag{3.1}$$

which is usually given in units of $\mathrm{n}/(\mathrm{cm}^2\mathrm{s})$.
When doing neutron scattering experiments a beam of neutrons is directed towards a sample, the neutrons interact with the sample, and they are measured. The results of these measurements are given as cross sections. Neutrons can be both scattered and absorbed by the sample, and an absorption and a scattering cross section can be defined. We will only look at the scattering cross section.
We define the differential scattering cross section, because we are interested in the angular dependence of the scattered neutrons

$$\frac{\mathrm{d}\sigma}{\mathrm{d}\Omega} = \frac{1}{\Psi}\frac{\text{number of neutrons scattered per second into solid angle } \mathrm{d}\Omega}{\mathrm{d}\Omega}. \tag{3.2}$$

This applies when we do not measure the energy of the scattered neutrons. When doing inelastic scattering, where the neutrons change energy during the experiment, it is important to keep track of this energy change. The energy dependence of the scattered neutrons is de-

scribed by the partial differential scattering cross section

$$\frac{\mathrm{d}^2\sigma}{\mathrm{d}\Omega \mathrm{d}E_f} = \tag{3.3}$$
$$\frac{1}{\Psi}\frac{\text{number of neutrons scattered per second into solid angle } \mathrm{d}\Omega \text{ with energy in } [E_f : E_f + \mathrm{d}E_f]}{\mathrm{d}\Omega \mathrm{d}E_f}.$$

Here the final energy of the neutrons is given by E_f.

If we can calculate these scattering cross sections we know what to expect from experiments. We start simple, by looking at scattering by a single nucleus, fixed in space and labeled j. The wave function of the incoming neutron can be described as a plane wave

$$\psi_i(\mathbf{r}) = \frac{1}{\sqrt{Y}} \exp(i\mathbf{k}_i \cdot \mathbf{r}), \tag{3.4}$$

where Y is a normalisation constant, which is unimportant.
The scattered neutron can be described as a spherical wave leaving the nucleus

$$\psi_f(\mathbf{r}) = \psi_i(\mathbf{r}_j)\frac{-b_j}{|\mathbf{r} - \mathbf{r}_j|} \exp(ik_f|\mathbf{r} - \mathbf{r}_j|), \tag{3.5}$$

where b_j denotes the scattering length, a quantity characteristic of the specific isotope describing how strongly the isotope scatters. The above equation is only valid when $|\mathbf{r} - \mathbf{r}_j| \gg b_j$.
Generally $\mathbf{r}$ is about 1 m and $\mathbf{r}_j$ is typically on the order of 1 μm or less. This means the density of outgoing neutrons can be approximated to

$$|\psi_f|^2 \approx |\psi_i|^2 \frac{b_j^2}{r^2}. \tag{3.6}$$

The number of neutrons per second intersecting a small surface $\mathrm{d}A$ is $v|\psi_f|^2\mathrm{d}A$. This means the number of neutrons per second in the solid angle $\mathrm{d}\Omega = \mathrm{d}A/r^2$ is $v|\psi_i|^2 b_j^2 \mathrm{d}\Omega$. The incoming flux is $\Psi = b|\psi_i|^2$, which leads to the expression

$$\frac{\mathrm{d}\sigma}{\mathrm{d}\Omega} = b_j^2. \tag{3.7}$$

Since the nucleus is fixed, the energy of the neutron must remain constant which means this is an example of elastic scattering.
Generally we are more concerned with scattering from a system of particles. We will add complexity by looking at the scattering from two nuclei and the interference between the two scattered waves. We assume elastic scattering and denote the nuclear scattering lengths as b_j and $b_{j'}$ respectively. This means the outgoing wave can be described by

$$\psi_f(\mathbf{r}) = \psi_i(\mathbf{r_j})\frac{-b_j}{|\mathbf{r} - \mathbf{r}_j|} \exp(ik_f|\mathbf{r} - \mathbf{r}_j|) + \psi_i(\mathbf{r_{j'}})\frac{-b_{j'}}{|\mathbf{r} - \mathbf{r}_{j'}|} \exp(ik_f|\mathbf{r} - \mathbf{r}_{j'}|). \tag{3.8}$$

As before we assume the distance to the observer is much larger than the distance to the two nuclei $r_j, r_{j'} \ll r$ which means we can rewrite the outgoing wave as

$$\psi_f(\mathbf{r}) = -\frac{1}{\sqrt{Y}}\frac{1}{r} \exp(i\mathbf{k}_f \cdot \mathbf{r}_j)(b_j \exp(i\mathbf{q} \cdot \mathbf{r_j}) + b_{j'} \exp(i\mathbf{q} \cdot \mathbf{r_{j'}})), \tag{3.9}$$

where we have defined the scattering vector

$$\mathbf{q} = \mathbf{k}_i - \mathbf{k}_f. \tag{3.10}$$

As before we have the intensity of neutrons impinging on a small area given as $v|\psi_f(\mathbf{r})|^2 \mathrm{d}A$. If we take the case of two identical nuclei with identical scattering lengths $b_j = b_{j'} = b$, the scattering cross section becomes

$$\frac{\mathrm{d}\sigma}{\mathrm{d}\Omega} = b^2|\exp(i\mathbf{q}\cdot\mathbf{r_j}) + \exp(i\mathbf{q}\cdot\mathbf{r}_{j'})|^2 = 2b^2(1+\cos(\mathbf{q}\cdot(\mathbf{r_j}-\mathbf{r}_{j'}))). \tag{3.11}$$

This equation shows interference in action: the scattering cross section varies with $\mathbf{q}$ and the distance between the atoms.
To find the cross section for a large number of nuclei, we would make the same calculation as above, which means we can generalise the equation to

$$\frac{\mathrm{d}\sigma}{\mathrm{d}\Omega} = \left|\sum_j b_j \exp(i\mathbf{q}\cdot\mathbf{r_j})\right|^2. \tag{3.12}$$

This sum will be zero unless $\mathbf{q}\cdot\mathbf{r} = 2\pi n$ where n is an integer.

3.2 Quantum mechanical treatment of scattering

To describe the inelastic scattering we need a quantum mechanical formulation of neutron scattering theory. As before we start with the state of the incoming wave, which is defined as

$$|\psi_i\rangle = \frac{1}{\sqrt{Y}}\exp(i\mathbf{k}_i\cdot\mathbf{r}), \tag{3.13}$$

where $Y = L^3$ can be identified as the normalisation volume for the state, assumed to be enclosed in a cubic box with side length L.
The state of the outgoing wave is expressed as a plane wave, instead of a spherical outgoing wave

$$|\psi_f\rangle = \frac{1}{\sqrt{Y}}\exp(i\mathbf{k}_f\cdot\mathbf{r}). \tag{3.14}$$

The scattering process itself is described by the Fermi Golden Rule which gives the rate of change between the initial state $|\psi_i\rangle$ and a final state $|\psi_f\rangle$

$$W_{i\to f} = \frac{2\pi}{\hbar}\frac{\mathrm{d}n}{\mathrm{d}E_f}|\langle\psi_i|\hat{V}|\psi_f\rangle|^2, \tag{3.15}$$

Where $\frac{\mathrm{d}n}{\mathrm{d}E_f}$ is the density of states in $\mathbf{k}$-space and $\hat{V}$ is the scattering potential of the neutron.
Inserting $\frac{\mathrm{d}n}{\mathrm{d}E_f} = \frac{Yk_f m_n}{2\pi^2\hbar^2}$ and $\mathrm{d}\Omega/(4\pi)$ we get only neutrons scattered into the solid angle $\mathrm{d}\Omega$.

$$W_{i\to f,\mathrm{d}\Omega} = \frac{Yk_f m_n}{(2\pi)^2\hbar^3}\mathrm{d}\Omega|\langle\psi_i|\hat{V}|\psi_f\rangle|. \tag{3.16}$$

With the number of neutrons scattered into $\mathrm{d}\Omega$ per second, we can find the differential scattering cross section

$$\frac{\mathrm{d}\sigma}{\mathrm{d}\Omega} = Y^2\frac{k_f}{k_i}\left(\frac{m_n}{2\pi\hbar^2}\right)^2|\langle\psi_i|\hat{V}|\psi_f\rangle|^2. \tag{3.17}$$

This can be used to find the same results for the scattering cross section as the semi-classical calculations.
It can also be used to develop the formalism for inelastic magnetic scattering. When looking at inelastic scattering we need to keep track of the quantum state of the sample since it changes during the scattering process. The initial and final sample states are $|\lambda_i\rangle$ and $|\lambda_f\rangle$ respectively. This results in the following partial differential scattering cross section for inelastic scattering

$$\left.\frac{\mathrm{d}^2\sigma}{\mathrm{d}\Omega\mathrm{d}E_f}\right|_{\lambda_i\to\lambda_f} = \frac{k_f}{k_i}\left(\frac{m_n}{2\pi\hbar^2}\right)^2 |\langle\lambda_i\mathbf{k}_i|\hat{V}|\mathbf{k}_f\lambda_f\rangle|^2\delta(E_{\lambda_i}-E_{\lambda_f}-\hbar\omega), \tag{3.18}$$

where the δ-function expresses explicit energy conservation and the normalisation factor Y is omitted.
We take the potential to be a sum of nuclear potentials

$$\hat{V} = \frac{2\pi\hbar^2}{m_n}\sum_j b_j\delta(\mathbf{r}-\mathbf{R}_j), \tag{3.19}$$

where $\mathbf{R}_j$ is the operator for the location of the j'th nucleus. Inserting this into the matrix element of the cross section we get

$$|\langle\lambda_i\psi_i|\hat{V}|\lambda_f\psi_f\rangle|^2 = \left(\frac{2\pi\hbar^2}{m_n}\right)^2\sum_{j,j'} b_j b_{j'}\langle\lambda_i|\exp(-i\mathbf{q}\cdot\mathbf{R}_j)|\lambda_f\rangle\langle\lambda_i|\exp(i\mathbf{q}\cdot\mathbf{R}_{j'})|\lambda_f\rangle. \tag{3.20}$$

The δ function is rewritten as

$$\delta(E_{\lambda_i}-E_{\lambda_f}+\hbar\omega) = \frac{1}{2\pi\hbar}\int_{-\infty}^{\infty}\exp\left(\frac{i(E_{\lambda_f}-E_{\lambda_i})t}{\hbar}\right)\exp(-i\omega t)\mathrm{d}t. \tag{3.21}$$

Insert these in the inelastic scattering cross section:

$$\begin{aligned}\left.\frac{\mathrm{d}^2\sigma}{\mathrm{d}\Omega\mathrm{d}E_f}\right|_{\lambda_i\to\lambda_f} &= \frac{k_f}{k_i}\sum_{j,j'}\frac{b_j b_{j'}}{2\pi\hbar}\int_{-\infty}^{\infty}\langle\lambda_i|\exp(-i\mathbf{q}\cdot\mathbf{R}_j)|\lambda_f\rangle \qquad (3.22)\\ &\quad\times\langle\lambda_f|\exp\left(\frac{iHt}{\hbar}\right)\exp(i\mathbf{q}\cdot\mathbf{R}_{j'})\exp\left(\frac{-iHt}{\hbar}\right)|\lambda_i\rangle\exp(-i\omega t)\mathrm{d}t,\\ \left.\frac{\mathrm{d}^2\sigma}{\mathrm{d}\Omega\mathrm{d}E_f}\right|_{\lambda_i\to\lambda_f} &= \frac{k_f}{k_i}\sum_{j,j'}\frac{b_j b_{j'}}{2\pi\hbar}\int_{-\infty}^{\infty}\langle\lambda_i|\exp(-i\mathbf{q}\cdot\mathbf{R}_j(0))|\lambda_f\rangle \qquad (3.23)\\ &\quad\times\langle\lambda_f|\exp(i\mathbf{q}\cdot\mathbf{R}_{j'}(t))|\lambda_i\rangle\exp(-i\omega t)\mathrm{d}t.\end{aligned}$$

Here we have made use of the fact that for a Hamiltonian H with eigenstate $|\lambda\rangle$ and corresponding eigenenergy the following is true:

$$\exp\left(\frac{iHt}{\hbar}\right)|\lambda\rangle = \exp\left(\frac{iE_\lambda t}{\hbar}\right)|\lambda\rangle. \tag{3.24}$$

We have further employed the time-dependent operators

$$\mathbf{R}_j(t) = \exp(iHt/\hbar)\mathbf{R}_j\exp(-iHt/\hbar). \tag{3.25}$$

In an experiment we do not observe the final state of the sample, only of the neutron. This means in order to find the total cross section, we can sum over all the possible final states. We furthermore only consider systems in thermal equilibrium, which means we can take a thermal average of the cross section.
This leads us to the equation for the observable cross section

$$\begin{aligned}\frac{\mathrm{d}^2\sigma}{\mathrm{d}\Omega \mathrm{d}E_f} &= \left\langle \sum_{\lambda_f} \frac{\mathrm{d}^2\sigma}{\mathrm{d}\Omega \mathrm{d}E_f}\bigg|_{\lambda_i \to \lambda_f} \right\rangle \\ &= \frac{k_f}{k_i} \sum_{j,j'} \frac{b_j b_{j'}}{2\pi\hbar} \int_{-\infty}^{\infty} \langle \exp(-i\mathbf{q}\cdot\mathbf{R}_j(0)) \exp(-i\mathbf{q}\cdot\mathbf{R}_{j'}(t))\rangle \exp(-i\omega t)\mathrm{d}t.\end{aligned} \tag{3.26}$$

This final equation covers both elastic and inelastic nuclear scattering.

3.3 Magnetic scattering

We now look at magnetic scattering. This is the scattering that occurs when the magnetic moment of the neutron interacts with the magnetic moments in a material. We here consider only magnetic fields arising from the spins of electrons in unpaired atomic orbitals.
We will develop the formalism for inelastic magnetic scattering. We start with the master equation for inelastic neutron scattering as given in Eq. 3.18. To use this we need the magnetic scattering potential, which we take to be the neutron interaction with the magnetic ions. This interaction is given by the total nuclear Zeeman interaction summed over all magnetic sites j:

$$\hat{V} = \frac{\mu_0}{4\pi} g\mu_B \gamma \mu_N \hat{\sigma} \cdot \nabla \times \left(\frac{\mathbf{s}_j \times (\mathbf{r} - \mathbf{r}_j)}{|\mathbf{r} - \mathbf{r}_j|^3} \right). \tag{3.27}$$

Here we have the Bohr magneton $\mu_B = e\hbar/(2m_e)$ and the nuclear magneton $\mu_N = e\hbar/(2m_p)$ where m_e and m_p are the masses of the electron and proton respectively.
We assume thermal equilibrium and sum over all of the possible final states $|\lambda_f\rangle$, like we did for nuclear scattering. Doing this and inserting the scattering potential we get

$$\begin{aligned}\frac{\mathrm{d}^2\sigma}{\mathrm{d}\Omega \mathrm{d}E_f}\bigg|_{\sigma_i \to \sigma_f} &= \frac{k_f}{k_i} \left(\frac{\mu_0}{4\pi}\right)^2 \left(\frac{m_n}{2\pi\hbar^2}\right)^2 (g\mu_B\gamma\mu_N)^2 \sum_{\lambda_i,\lambda_f} p_{\lambda_i} \\ &\times \left| \left\langle \mathbf{k}_f \lambda_f \sigma_f \middle| \hat{\sigma} \cdot \nabla \times \left(\frac{\mathbf{s}_j \times (\mathbf{r} - \mathbf{r}_j)}{|\mathbf{r} - \mathbf{r}_j|^3} \right) \middle| \mathbf{k}_i \lambda_i \sigma_i \right\rangle \right|^2 \\ &\times \delta(\hbar + E_{\lambda_i} - E_{\lambda_f}).\end{aligned} \tag{3.28}$$

The matrix element can be simplified using the following mathematical identity

$$\nabla \times \left(\frac{\mathbf{s}_j \times (\mathbf{r} - \mathbf{r}_j)}{|\mathbf{r} - \mathbf{r}_j|^3} \right) = \frac{1}{2\pi^2} \int \hat{\mathbf{q}}' \times (\mathbf{s}_j \times \hat{\mathbf{q}}') \exp(i\mathbf{q}' \cdot (\mathbf{r} - \mathbf{r}_j)) \mathrm{d}^3\mathbf{q}'. \tag{3.29}$$

Inserting this into the matrix element and performing the integral over k-states we find

$$\begin{aligned}\langle \mathbf{k}_f \lambda_f \sigma_f | \hat{V} | \mathbf{k}_i \lambda_i \sigma_i \rangle &= 4\pi \langle \lambda_f \sigma_f | \sum_j \exp(i\mathbf{q}\cdot\mathbf{r}_j) \hat{\sigma} \cdot (\hat{\mathbf{q}} \times (\mathbf{s}_j \times \hat{\mathbf{q}})) | \lambda_i \sigma_i \rangle \\ &= 4\pi \sum_j \langle \lambda_f \sigma_f | \exp(i\mathbf{q}\cdot\mathbf{r}_j) \hat{\sigma} \cdot \mathbf{s}_{j\perp} | \lambda_i \sigma_i \rangle.\end{aligned} \tag{3.30}$$

Here we have defined the spin-component perpendicular to the scattering vector $\mathbf{s}_{j\perp} \equiv \hat{\mathbf{q}} \times (\mathbf{s}_j \times \hat{\mathbf{q}})$.

Now we look at the spin part of the matrix element to further simplify it. Assuming that the neutrons are unpolarized, we will not observe the final spin state of the neutron. This means we sum over σ_f and average over the initial state σ_i. Furthermore since the initial neutron state does not correlate with the initial sample state we can factorise the inner products

$$\begin{aligned}
&\sum_{\sigma_i,\sigma_f} p_{\sigma_i} |\langle \sigma_f \lambda_f | \hat{\sigma} \cdot \mathbf{s}_\perp | \sigma_i \lambda_i \rangle|^2 \qquad (3.31)\\
&\quad = \sum_{\alpha,\beta} \sum_{\sigma_i,\sigma_f} p_{\sigma_i} \langle \sigma_i | \sigma^\beta | \sigma_f \rangle \langle \sigma_f | \sigma^\alpha | \sigma_i \rangle \langle \lambda_i | s_\perp^\beta | \lambda_f \rangle \langle \lambda_f | s_\perp^\alpha | \lambda_i \rangle \\
&\quad = \sum_{\alpha,\beta} \sum_{\sigma_i} p_{\sigma_i} \langle \sigma_i | \sigma^\beta \sigma^\alpha | \sigma_i \rangle \langle \lambda_i | s_\perp^\beta | \lambda_f \rangle \langle \lambda_f | s_\perp^\alpha | \lambda_i \rangle.
\end{aligned}$$

For unpolarised neutrons $\alpha = \beta$: $\sum_{\sigma_i} p_{\sigma_i} \langle \sigma_i | \sigma^\alpha \sigma^\alpha | \sigma_i \rangle = 1$. Likewise if we have $\alpha \neq \beta$: $\sum_{\sigma_i} p_{\sigma_i} \langle \sigma_i | \sigma^\alpha \sigma^\beta | \sigma_i \rangle = 0$.
We can use this to perform the sum over σ_i to obtain

$$\sum_{\sigma_i,\sigma_f} p_{\sigma_i} |\langle \sigma_f \lambda_f | \hat{\sigma} \cdot \mathbf{s}_\perp | \sigma_i \lambda_i \rangle|^2 = \sum_\alpha \langle \lambda_i | s_\perp^\alpha | \lambda_f \rangle \langle \lambda_f | s_\perp^\alpha | \lambda_i \rangle. \qquad (3.32)$$

Summing over the final states $|\lambda_f\rangle$ results in

$$\langle \lambda_i | \mathbf{s}_{j,\perp} \cdot \mathbf{s}_{j',\perp} | \lambda_i \rangle. \qquad (3.33)$$

We can use that the perpendicular projection is defined as $\mathbf{s}_{j\perp} = \mathbf{s}_j - (\mathbf{s}_j \cdot \hat{\mathbf{q}})\hat{\mathbf{q}}$

$$\mathbf{s}_{j\perp} \cdot \mathbf{s}_{j'\perp} = \sum_{\alpha,\beta} (\delta_{\alpha\beta} - \hat{q}_\alpha \hat{q}_\beta) s_j^\alpha s_{j'}^\beta. \qquad (3.34)$$

Inserting this, we get the magnetic cross section to be

$$\begin{aligned}
\frac{\mathrm{d}^2\sigma}{\mathrm{d}\Omega \mathrm{d}E_f} &= (\gamma r_0)^2 \frac{k_f}{k_i} \left[\frac{g}{2} F(\mathbf{q}) \right]^2 \sum_{\alpha,\beta} (\delta_{\alpha\beta} - \hat{q}_\alpha \hat{q}_\beta) \qquad (3.35)\\
&\quad \times \sum_{\lambda_i,\lambda_f} p_{\lambda_i} \sum_{j,j'} \langle \lambda_i | \exp(-i\mathbf{q} \cdot \mathbf{r}_{j'}) s_{j'}^\alpha | \lambda_f \rangle \langle \lambda_f | \exp(i\mathbf{q} \cdot \mathbf{r}_j s_j^\beta | \lambda_i \rangle \\
&\quad \times \delta(E_{\lambda_i} - E_{\lambda_f} + \hbar\omega).
\end{aligned}$$

here $F(\mathbf{q})$ is the magnetic form factor defined as

$$F(\mathbf{q}) = \int \exp(i\mathbf{q} \cdot \mathbf{r}) \rho_s(\mathbf{r}) \mathrm{d}^3\mathbf{r}, \qquad (3.36)$$

and stems from the assumption that the electrons that cause the magnetism are located in orbitals around particular ions. Here $\rho_s(\mathbf{r})$ is defined as the normalised spin density on the unfilled orbitals.
The prefactors have been rewritten using the classical electron radius $r_0 = e^2\mu_0/(4\pi m_e)$.
As in the derivation of the nuclear cross section we rewrite the δ-function as an integral and use the definition of a time dependent operator.

After making this transformation and performing the completeness sum over the final states $|\lambda_f\rangle$ we get the following cross section for magnetic scattering

$$\frac{\mathrm{d}^2\sigma}{\mathrm{d}\Omega \mathrm{d}E_f} = \frac{(\gamma r_0)^2}{2\pi\hbar}\frac{k_f}{k_i}\left(\frac{g}{2}F(\mathbf{q})\right)^2 \sum_{\alpha,\beta}(\delta_{\alpha\beta} - \hat{q}_\alpha\hat{q}_\beta) \tag{3.37}$$

$$\times \sum_{j,j'}\int_{-\infty}^{\infty}\mathrm{d}t e^{-i\omega t}\langle \exp(-i\mathbf{q}\cdot\mathbf{R}_j(0))s_j^\alpha(0)\exp(i\mathbf{q}\cdot\mathbf{R}_{j'}(t)s_{j'}^\beta(t).\rangle \tag{3.38}$$

The nuclear spin position $\mathbf{R}(t)$ and the atomic spin $\mathbf{s}(t)$ are both operators with an elastic and an inelastic part. Since we are interested in the magnetic signal we can disregard the contributions that are inelastic in the phonon channel. This leaves us the with magnetic diffraction signal which is elastic in both channels and the inelastic magnetic signal which is elastic in the phonon channel and inelastic in the spins.
This means we can replace the general nuclear position operators $\mathbf{R}_j(t)$ with the nuclear equilibrium positions in a lattice, $\mathbf{r}_j$, multiply with the Debye-Waller factor, and use the periodicity of the lattice to find the following.

$$\left(\frac{\mathrm{d}^2\sigma}{\mathrm{d}\Omega \mathrm{d}E_f}\right)_{magn.} = \frac{(\gamma r_0)^2}{2\pi\hbar}\frac{k_f}{k_i}\left(\frac{g}{2}F(\mathbf{q})\right)^2 \exp(-2W)\sum_{\alpha,\beta}(\delta_{\alpha\beta} - \hat{q}_\alpha\hat{q}_\beta) \tag{3.39}$$

$$\times \sum_{j,j'}\int_{-\infty}^{\infty}\mathrm{d}t e^{i\mathbf{q}\cdot(\mathbf{r}_{j'}-\mathbf{r}_j)}\langle \mathbf{s}_j^\alpha(0)\mathbf{s}_{j'}^\beta(t)\rangle e^{-i\omega t}.$$

Going back to the semiclassical approximation where the spins can be described as vectors we get

$$\left(\frac{\mathrm{d}^2\sigma}{\mathrm{d}\Omega \mathrm{d}E_f}\right)_{magn.} = \frac{(\gamma r_0)^2}{2\pi\hbar}\frac{k_f}{k_i}\left(\frac{g}{2}F(\mathbf{q})\right)^2 \exp(-2W)\sum_{\alpha,\beta}(\delta_{\alpha\beta} - \hat{q}_\alpha\hat{q}_\beta) \tag{3.40}$$

$$\times \sum_j \mathbf{s}_j^\alpha(0)e^{-i\mathbf{q}\cdot\mathbf{r}_j}\sum_{j'}\int_{-\infty}^{\infty}\mathrm{d}t e^{i\mathbf{q}\cdot\mathbf{r}_{j'}}\mathbf{s}_{j'}^\beta(t)e^{-i\omega t}$$

$$= \frac{(\gamma r_0)^2}{2\pi\hbar}\frac{k_f}{k_i}\left(\frac{g}{2}F(\mathbf{q})\right)^2 \exp(-2W)\sum_{\alpha,\beta}(\delta_{\alpha\beta} - \hat{q}_\alpha\hat{q}_\beta)S^{\alpha,\beta}(\mathbf{q},\omega), \tag{3.41}$$

where $S^{\alpha,\beta}(\mathbf{q},\omega)$ is the scattering function defined as

$$S^{\alpha,\beta}(\mathbf{q},\omega) = \sum_j \mathbf{s}_j^\alpha(0)e^{-i\mathbf{q}\cdot\mathbf{r}_j}\sum_{j'}\int_{-\infty}^{\infty}\mathrm{d}t e^{i\mathbf{q}\cdot\mathbf{r}_{j'}}\mathbf{s}_{j'}^\beta(t)e^{-i\omega t}. \tag{3.42}$$

This can be simulated and compared to experiments.
Generally we can take $\alpha = \beta$, as performing the sums over α and β will show $S^{\alpha,\beta} = -S^{\beta,\alpha}$ in all but a few cases with chiral symmetry.

3.4 Reciprocal space

When calculating the above cross section for the simulated spin movements it is important to use to correct **q**-vectors. The amount of **q**-vectors we can calculate the scattering function for is determined by the amount of unit cells simulated.

This is relevant when simulating a spin chain, a triangle and a kagomé lattice. The kagomé lattice is a lattice of triangles, where some spins have been taken out see Figure 3.1. For the spin chain the unit cell consists of one spin in case of the ferromagnetic chain and two spins for the antiferromagnetic chain. For the kagomé lattice the unit cell consists of three spins in a triangle. Figure 3.1a shows 3×3 unit cells.

3.4.1 Reciprocal kagomé lattice

We are interested in which $\mathbf{q}$-values are relevant for the kagomé lattice. To find this out it is helpful to find the reciprocal lattice vectors.
First the constant α is defined as $\alpha = 3.645$ Å. α is the shortest distance between two atoms.

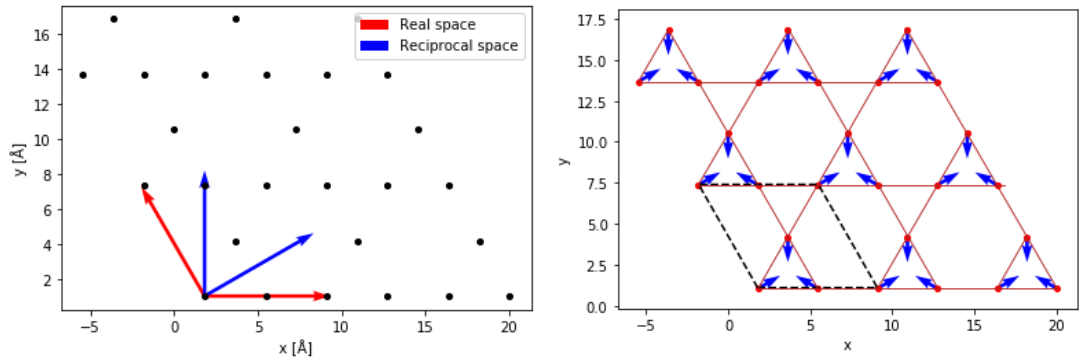

(a) The lattice vectors and reciprocal space vectors for the kagomé lattice.

(b) The $\mathbf{q} = 0$ ground state. A unit cell is shown by the black dashed lines.

Figure 3.1

The lattice vectors are defined so they encompass one unit cell, as seen in Figure 3.1a.

$$\mathbf{a} = \begin{pmatrix} 2\alpha \\ 0 \\ 0 \end{pmatrix}, \quad \mathbf{b} = \begin{pmatrix} -\alpha \\ \sqrt{3}\alpha \\ 0 \end{pmatrix}, \quad \mathbf{c} = \begin{pmatrix} 0 \\ 0 \\ \beta \end{pmatrix}. \tag{3.43}$$

In this case we have defined β to be an arbitrary length with units Å. It is not important exactly what this constant is since we are only interested in the plane spanned by $\mathbf{a}$ and $\mathbf{b}$. We can now use the lattice vectors to find the reciprocal lattice vectors. We only look at a 2D kagomé lattice, which means we can look only a the reciprocal lattice in the plane. The reciprocal lattice vectors are defined as follows.

$$\mathbf{a}^* = 2\pi \frac{\mathbf{b} \times \mathbf{c}}{\mathbf{a} \cdot (\mathbf{b} \times \mathbf{c})} \qquad \mathbf{b}^* = 2\pi \frac{\mathbf{c} \times \mathbf{a}}{\mathbf{a} \cdot (\mathbf{b} \times \mathbf{c})}. \tag{3.44}$$

Inserting the lattice vectors, gives the following reciprocal lattice vectors

$$\mathbf{a}^* = \frac{\pi}{\sqrt{3}\alpha} \begin{pmatrix} \sqrt{3} \\ 1 \\ 0 \end{pmatrix} \qquad \mathbf{b}^* = \frac{\pi}{\sqrt{3}\alpha} \begin{pmatrix} 0 \\ 2 \\ 0 \end{pmatrix}. \tag{3.45}$$

Now when we write $\mathbf{q} = (h, k)$ we mean $\mathbf{q} = h\mathbf{a}^* + k\mathbf{b}^*$.

We can now write the coordinates of the spins in a unit cell as follows

$$\begin{aligned}\Delta_0 &= 0\mathbf{a} + 0\mathbf{b}\\ \Delta_1 &= \frac{1}{2}\mathbf{a}\\ \Delta_2 &= \frac{1}{2}\mathbf{a} + \frac{1}{2}\mathbf{b}.\end{aligned}$$

3.4.2 Kagomé form factors

To find where we expect peaks in the reciprocal lattice we look at the elastic scattering function, found from Eq. 3.40

$$S^{\alpha\alpha}(\mathbf{q},\omega) \propto \sum_{j'} s^{\alpha}_{j'}(t_0)\exp(-i\mathbf{q}\cdot\mathbf{r_{j'}})\sum_{j} s^{\alpha}_{j}(t_0)\exp(i\mathbf{q}\cdot\mathbf{r_j}). \tag{3.46}$$

This is the scattering function for $\alpha = \beta$, because the terms for $\alpha \neq \beta$ cancel out, as the lattice does not have chiral symmetry.
We can start by looking at one of the sums, as they are the complex conjugate of each other

$$\sum_{j} s^{\alpha}_{j}(t_0)\exp(i\mathbf{q}\cdot\mathbf{r}_j). \tag{3.47}$$

Instead of summing over the whole lattice we can split this into a sum over the unit cells in the lattice and the spins in a unit cell.

$$\sum_{j} e^{i\mathbf{q}\cdot\mathbf{r}} = \sum_{k} e^{i\mathbf{q}\cdot\mathbf{R_k}}\sum_{\Delta} s^{\alpha}_{\Delta}(t_0)e^{i\mathbf{q}\cdot\Delta}. \tag{3.48}$$

The sum over the unit cells in the lattice is known as the lattice sum, and this gives us a δ-function that tells us that the inserted $\mathbf{q}$-vectors must be integer multiples of the reciprocal lattice vectors. This is an example of Bragg's law.

$$\sum_{k}\exp(i\mathbf{q}\cdot\mathbf{R}_k) \propto \delta(\mathbf{q},\tau) \tag{3.49}$$

The second sum is more interesting as it contains the spin directions. We will calculate this sum in two cases. The first case is for all of the spins being parallel to each other. This is equivalent to the nuclear scattering. We insert the coordinates of the spins in the unit cell

$$F_\alpha = \left(s^\alpha e^{i\mathbf{q}\cdot\frac{1}{2}\mathbf{a}} + s^\alpha e^{i\mathbf{q}\cdot(\frac{1}{2}\mathbf{a}+\frac{1}{2}\mathbf{b})} + s^\alpha\right). \tag{3.50}$$

Inserting $\mathbf{q} = h\mathbf{a}^* + k\mathbf{b}^*$ and $s^\alpha = 1$ into the form factor results in

$$F(h,k) = 1 + e^{ih\pi} + e^{i(h+k)\pi}. \tag{3.51}$$

This shows us that we will have elastic peaks from nuclear scattering when h and k are integer values, with the strongest peaks at $h = 0, 2$ and $k = 0, 2$.

To see how the spins affect this, we look at Eq. 3.47 again, but this time taking the spin directions into account. As we are still looking at elastic scattering it makes sense to take the spin directions of a ground state. The ground state chosen is the $\mathbf{q} = 0$ state where the spins

have 120° to each other, as seen in Figure 3.1b. The spins in a unit cell have the following coordinates

$$\mathbf{s}_0 = \frac{\sqrt{3}}{2}\hat{x} + \frac{1}{2}\hat{y}, \tag{3.52}$$

$$\mathbf{s}_1 = -\frac{\sqrt{3}}{2}\hat{x} + \frac{1}{2}\hat{y}, \tag{3.53}$$

$$\mathbf{s}_2 = 0\hat{x} - 1\hat{y}. \tag{3.54}$$

These are then inserted into the form factor equation to find the form factors in the x- and y-directions.

$$F_x(h,k) = \frac{3}{2} - \frac{3}{2}\exp(ih\pi), \tag{3.55}$$

$$F_y(h,k) = \frac{1}{2} + \frac{1}{2}\exp(ih\pi) - \exp(i(h+k)\pi). \tag{3.56}$$

If we ignore the rule that only the spin component perpendicular to $\mathbf{q}$ is part of the scattering cross section, as we do in the simulations, we will observe the cross section $\sum_\alpha S^{\alpha\alpha}(\mathbf{q},\omega)$. This means we can take the total form factor to be the sum of the individual components squared

$$|F_{tot}|^2 = |F_x|^2 + |F_y|^2 = 3 - \cos(h\pi) - \cos(k\pi) - \cos((h+k)\pi). \tag{3.57}$$

We can see that $|F_{tot}|^2 = 0$ when h, k are both even, and maximum $|F_{tot}|^2 = 4$ when either h or k is odd. This pattern of peaks shows a kagomé lattice, as can be seen in Figure 3.2, showing that the reciprocal lattice also is a kagomé lattice. In this figure the scattering cross section has been plotted for different values of q_x and q_y.

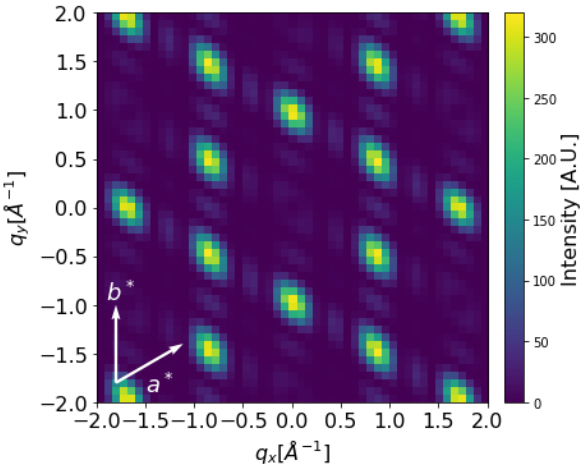

Figure 3.2: The cross section of a kagomé lattice with spins in a ground state. The reciprocal lattice vectors are plotted in white, with $\mathbf{a} = (7.3, 0)$ Å, $\mathbf{b} = (-3.6, 6.3)$ Å, $\mathbf{a}^* = (0.9, 0.5)$ Å, and $\mathbf{b}^* = (0, 1.0)$ Å.

Chapter 4

Implementation of Simulations

This chapter will describe the simulation program Classical Langevin Spin Simulations Code (CLaSSiC) [29]. The first version of this simulation tool was written in Matlab by Jakob Garde to simulate a system of two spins with anisotropy and comparing with experimental results [30]. This was expanded upon by Henrik Jacobsen who also compared with experimental data [10]. Rasmus Tang Christensen rewrote the code in Python to be able to simulate more than two spins in order to investigate triangular systems and a hyperkagomé lattice [31]. Jonas Peter Hyatt wrote the current version of the program, which is generalised to work for an arbitrary spin geometry and does integration in spherical coordinates [32]. This version was further modified and validated by Emma Lenander [12] and myself. I have further validated and extended the work by 1) Implementing single-ion anisotropy and 2) Implementing integration in Cartesian coordinates.

I will outline the derivation of the equations of motion that form the basis of CLaSSiC. Then the program will be described from a user's perspective and finally the various results from the simulations on systems ranging from one spin to 3×3 unit cells of a kagomé lattice will be described.

4.1 Langevin spin dynamics

In Chapter 2 the semi-classical spin dynamics of spins interacting with a magnetic field, anisotropy and each other via the exchange interaction were derived. The next step is to include temperature effects. To add temperature we couple the spins to a heat bath. This means the energy of the system is no longer constant, but can fluctuate. A damping term is added to remove energy from the system and a random magnetic field is added to add energy to the system. These two terms need to be equal on average so that the system remains in thermal equilibrium.
The damping term is proportional to the velocity of the spin precession times a constant $\lambda \ll 1$ and thus has magnitude $|\frac{\partial \mathbf{s}_i}{\partial t}|$. The direction should lead to the minimum energy configuration for the spin which occurs when the spin is anti parallel to the magnetic field.
The random field $\mathbf{b}(t)$ is added to simulate the small perturbations temperature causes to a system.
The total time evolution of the spin is now [30]

$$\frac{\mathrm{d}\mathbf{s}_i}{\mathrm{d}t} = \gamma \mathbf{s}_i \times (\tilde{\mathbf{B}} + \mathbf{b}) \pm \lambda \mathbf{s}_i \times \frac{\partial \mathbf{s}_i}{\partial t}. \tag{4.1}$$

Here we have defined the random term to be

$$\langle b^2 \rangle = \frac{2\lambda k_B T \hbar \mathrm{d}t}{s(g\mu_B)^2}, \tag{4.2}$$

where k_B is the Boltzmann constant, $\mathrm{d}t$ is the simulation time step, λ is the damping factor and T is the temperature. The damping factor is typically in the order of 10^{-4}. It is important to notice that the temperature is defined in absolute units due to the fluctuation-dissipation theorem [33], which makes it possible to compare simulations directly to experiments.
By expanding $\frac{\partial \mathbf{s}_i}{\partial t}$ to first order in λ we get

$$\frac{\mathrm{d}\mathbf{s}_i}{\mathrm{d}t} = \gamma \mathbf{s}_i \times (\tilde{\mathbf{B}} + \mathbf{b}) - \gamma\lambda \mathbf{s}_i \times (\mathbf{s}_i \times \tilde{\mathbf{B}}). \tag{4.3}$$

The equation has a deterministic part determined by $\tilde{\mathbf{B}}$ and a random part determined by the size of the random field $\mathbf{b}$.

$$\frac{\mathrm{d}\mathbf{s}_i}{\mathrm{d}t}\Big|_{det} = \gamma(\mathbf{s}_i \times \tilde{\mathbf{B}}) - \gamma\lambda \mathbf{s}_i \times (\mathbf{s}_i \times \tilde{\mathbf{B}}), \tag{4.4}$$

$$\frac{\mathrm{d}\mathbf{s}_i}{\mathrm{d}t}\Big|_{rand} = \gamma(\mathbf{s}_i \times \mathbf{b}). \tag{4.5}$$

We numerically integrate Eq. 4.3 to find a real space trajectory for each spin, which can be related to experiments by Fourier transformation as shown below.
The integration method used for the deterministic part is the fifth order Adams-Bashforth method [34]. This is a linear multistep method, meaning it evaluates the next step in the integration by using a weighted average of a single new function evaluation and the previous four function evaluations. The equation for calculating the next step is

$$\begin{aligned} y_{n+5} = y_{n+4} + \mathrm{d}t\Big(&\frac{1901}{720} f(t_{n+4}, y_{n+4}) - \frac{2774}{720} f(t_{n+3}, y_{n+3}) + \\ &\frac{2616}{720} f(t_{n+2}, y_{n+2}) - \frac{1274}{720} f(t_{n+1}, y_{n+1}) + \frac{251}{720} f(t_n, y_n)\Big). \end{aligned} \tag{4.6}$$

Where $f(t, y) = \gamma(\mathbf{s}_i \times \tilde{\mathbf{B}}) + \gamma\lambda \mathbf{s}_i \times (\mathbf{s}_i \times \tilde{\mathbf{B}})$.
The random part is added to this integration every time step

$$\frac{\mathrm{d}\mathbf{s}_i}{\mathrm{d}t} = y_{n+5} + \gamma(\mathbf{s}_i \times \mathbf{b}). \tag{4.7}$$

It is important to note that the integration of the random part is done differently from the deterministic part. This is explained the Garde's thesis [30].
The numerical integration have been implemented both in Cartesian coordinates and spherical coordinates. The derivation of Eq. 4.3 in spherical coordinates can be found in Appendix B. This version of the code was implemented first in spherical coordinates as it eliminated the need to renormalise the spin after each time step, as is necessary for the integration in Cartesian coordinates. The integration in spherical coordinates introduced other errors, like the simulations becoming suddenly unstable and the spin starting to behave randomly, and the temperature effects not functioning exactly as expected.

The program also includes an option to do the numerical integration using a 2nd or 4th order Runge Kutta methods. However there is a bug in the current implementation, introduced

when converting the code to Python. The bug went unnoticed until now. These methods only give correct results for the Zeeman-interaction and do not conserve energy for the exchange interaction and anisotropy. This is due to the fact that the effective magnetic field $\tilde{B}$ does not update between time steps. In this thesis only the Adams-Bashforth integration is used.

4.2 Scattering cross section

The goal with the simulations is to compare them with experimental data. To achieve this we need to calculate the scattering cross section from the simulated spin movements.
We start from Eq. 3.40. The absolute value of the intensity is not important for our purposes, so the prefactors have been omitted for simplicity.

$$S^{\alpha\beta}(\mathbf{q},\omega) = \sum_j \mathbf{s}_j^\alpha(0)e^{-i\mathbf{q}\cdot\mathbf{r}_j} \sum_{j'} \int_{-\infty}^{\infty} \mathrm{d}t e^{i\mathbf{q}\cdot\mathbf{r}_{j'}} \mathbf{s}_{j'}^\beta(t) e^{-i\omega t}, \tag{4.8}$$

where $\mathbf{q} = \mathbf{k}_f - \mathbf{k}_i$ is the scattering vector, α and β run over the Cartesian coordinates, j and j' run over the spins, r_j and $r_{j'}$ are the lattice positions of the spins, and s_j^α and $s_{j'}^\beta$ are the α,β components of the j, j' th spin.
Shifting by t_0 and assuming $\alpha = \beta$:

$$S^{\alpha\alpha}(\mathbf{q},\omega) = \sum_{j'} s_{j'}^\alpha(t_0)\exp(-i\mathbf{q}\cdot\mathbf{r_{j'}}) \sum_j \int_\infty s_j^\alpha(t_0+t)\exp(i\mathbf{q}\cdot\mathbf{r_j})\exp(-i\omega t)\mathrm{d}t. \tag{4.9}$$

The reason we can assume $\alpha = \beta$ is because performing the sums over α and β will show $S^{\alpha,\beta} = -S^{\beta,\alpha}$ in all but a few cases.
When deriving the magnetic cross section, we saw that neutrons only observe $\mathbf{s}_\perp$, the components of the spin vector perpendicular to $\mathbf{q}$. In the simulations we are not limited by this, and instead of calculating this for every time step in the simulation the cross section was calculated for each component of the spin x, y, and z.

4.3 From a user's perspective

CLaSSiC is implemented as a Python package using a class based approach, chosen to allow for the easiest development and reuse of simulations. The simulations are implemented in a general fashion, which means the specific systems and the framework for simulating are separate. The basic idea is to take a crystal structure provided by the user and solve the equations of motion seen in Eq. 4.3 for all of the spins.
The crystal structure is loaded via an input file containing the positions of the spins. The file can contain one or several unit cells, and one can set periodic boundary conditions in chosen axes. The nearest neighbours of the individual spins are found by the program, based on the distance between the spins in the chosen lattice and the boundary conditions. Then a Python class is defined which extends the simulation base class. The base class contains the general logic of the simulations and the user class specifies the parameters:

- Size of the spin s
- The external magnetic field $\mathbf{B}$

- The nearest neighbour exchange constant J
- The anisotropy matrix B_{anis}
- The temperature T
- The coefficient of friction λ

The spins are modelled as semi-classical vectors.
Once the parameters are loaded the user can specify the initial orientations of the spins or they can let the program find an approximate ground state via simulated annealing [32]. The simulation can run after specifying the timestep dt and the number of simulated datapoints N.
The parameters can be split into the physical parameters and non-physical parameters. The physical parameters are the ones that can be measured or controlled in an experiment: the exchange constant J, spin s, anisotropy B_{anis}, external magnetic field B, and temperature T. The non-physical parameters are the ones that are artefacts of the simulation: the time step dt, number of simulated datapoints N and friction coefficient λ.

4.3.1 Units

There are several different interactions implemented in CLaSSiC and used in the following simulations and it is useful to have them in the same units. We have chosen Kelvin. The exchange interaction J and temperature T are given in Kelvin as default. The external magnetic field B can be calculated in Kelvin like

$$B^K = \frac{g\mu_B}{2sk_B}B, \tag{4.10}$$

where B^K is the magnetic field in Kelvin, s is the spin size and B is the magnetic field in Tesla.
The anisotropy in units of Kelvin is given by [10]

$$D = \frac{g\mu_B}{2s'k_B}B_{anis}, \tag{4.11}$$

where D is the anisotropy in Kelvin, $s' = s - \frac{1}{2}$, and B_{anis} is the anisotropy in Tesla. As an example a magnetic field of 5 T corresponds to 1 K.

4.4 Output of simulations

After the simulation the simulation can output different forms of data. The most straight forward is the spin movements of all of the simulated spins, specifically the x, y, and z-components of the spin as a function of time. These can be Fourier-transformed to find the scattering function according to Eq. 4.9 $S(\mathbf{q}, \omega)$ which shows the intensity as a function of the momentum transfer $\mathbf{q}$ and energy ω. This can show the excitation energies of the system as peaks in the intensity. The third level of abstraction is the analysis of the scattering function. An example of this would be fitting a Lorentzian function to find the specific energies and width of the excitation peaks. Examples of these three outputs will be shown in Chapter 5.

Chapter 5

Validation

This chapter shows the extensive validation of the code done throughout this thesis. We will compare the integration in spherical coordinates with integration in Cartesian coordinates. We will validate the implementation of the Zeeman interaction, the temperature, the nearest neighbour exchange interaction and the single ion anisotropy. The combined effects of these interactions are also validated on different systems, like two spins with anisotropy and exchange interaction, and a spin chain with exchange interaction and a magnetic field. This is a crucial part of running simulations intended to be comparable with experimental data. We must verify that the simulations give the correct result when simulating systems with known behaviour, otherwise we cannot trust them to be correct when simulating more complex systems.

5.1 Zeeman interaction

To validate the implementation of the Zeeman interaction a single spin in a magnetic field was simulated, with spin value $s = \frac{7}{2}$, zero temperature and damping, and $\mathrm{d}t = 1 \cdot 10^{-14}$ s. We expect the spin to precess around the magnetic field axis with the Larmor frequency as illustrated in Figure 5.1. The spin components of this simulation are shown in Figure 5.2a as a function of time. The figure shows that the spin oscillates in x and y and stays stationary along the z-direction. This shows that the spin does precess around the z-axis with a constant angle as expected. To find the energy of the precession we look at the Fourier transformation of the spin movement, also known as the scattering function $S(\mathbf{q}, \omega)$. This is shown in Figure 5.2b with a Lorentzian function fitted to the peak. From this fit we can extract the mean and width of the peak, which we take as the energy of the oscillation and the error on the energy.

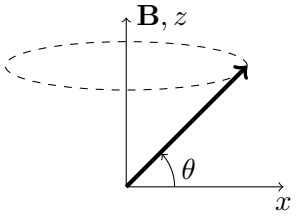

Figure 5.1: One spin in a magnetic field $\mathbf{B}$ and angle θ with the x-axis.

The Larmor frequency as given by Eq. 2.6 is calculated to be $\hbar\omega_L = 0.5794$ meV for a magnetic field of $B = 5$ T.
The simulation using Cartesian coordinates yielded a Larmor frequency of $\hbar\omega_L = 0.5792 \pm 0.002$ meV. The simulation done in spherical coordinates gave the same frequency of $\hbar\omega_L = 0.5792 \pm 0.002$ meV.

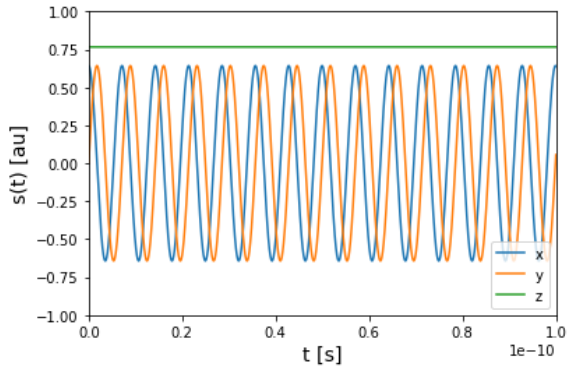

(a) The spin components of a single spin in a magnetic field with field strength $B = 5$ T, and angle $\theta = 50^\circ$ with the x-axis.

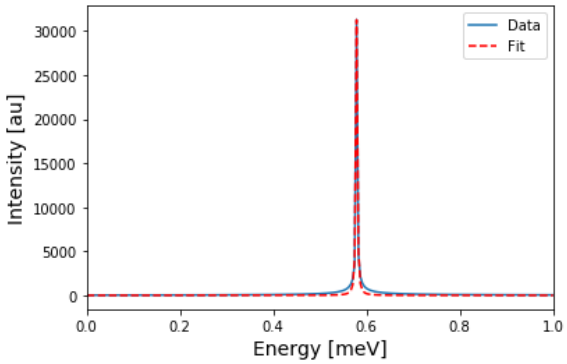

(b) Intensity as a function of energy for one spin in a magnetic field with field strength $B = 5$ T.

Figure 5.2

5.2 Anisotropy

To validate the implementation of the anisotropy, a single spin with an easy axis anisotropy was simulated. With an easy axis anisotropy and no other interactions the spin will precess around the anisotropy easy axis with a frequency depending on the canting angle between the spin and the easy axis. The expected energy can be found by looking at the equation of motion

$$\frac{\mathrm{d}\mathbf{s}}{\mathrm{d}t} = \gamma \mathbf{s} \times (-\mathbf{B}_{anis}), \tag{5.1}$$

where $\mathbf{B}_{anis}$ is the anisotropy field.
Inserting the spin vector and setting the anisotropy direction along the z-axis

$$\frac{\mathrm{d}}{\mathrm{d}t}\begin{pmatrix}\cos(\theta)\cos(\omega t)\\ \cos(\theta)\sin(\omega t)\\ \sin(\theta)\end{pmatrix} = \gamma \begin{pmatrix}\cos(\theta)\cos(\omega t)\\ \cos(\theta)\sin(\omega t)\\ \sin(\theta)\end{pmatrix} \times -B_{anis}\begin{pmatrix}0&0&0\\0&0&0\\0&0&1\end{pmatrix}\begin{pmatrix}\cos(\theta)\cos(\omega t)\\ \cos(\theta)\sin(\omega t)\\ \sin(\theta)\end{pmatrix}, \tag{5.2}$$

$$\Leftrightarrow \omega\cos(\theta)\begin{pmatrix}-\sin(\omega t)\\ \cos(\omega t)\\ 0\end{pmatrix} = \gamma B_{anis}\begin{pmatrix}-\cos(\theta)\sin(\theta)\sin(\omega t)\\ \cos(\theta)\sin(\theta)\cos(\omega t)\\ 0\end{pmatrix}. \tag{5.3}$$

Here B_{anis} is the anisotropy field strength and θ is the canting angle with respect to the anisotropy axis.
Setting $t = 0$

$$\omega\cos(\theta)\begin{pmatrix}0\\1\\0\end{pmatrix} = \gamma B_{anis}\begin{pmatrix}0\\ \cos(\theta)\sin(\theta)\\ 0\end{pmatrix}. \tag{5.4}$$

Taking the y-coordinate and inserting $\gamma = g\mu_B/\hbar$ we get

$$\hbar\omega = g\mu_B B_{anis}\cos(\theta). \tag{5.5}$$

The simulated results are shown in Figure 5.3, and show excellent agreement.

This works with the anisotropy easy axis in any direction. The easy plane anisotropy will be tested in Section 5.5.

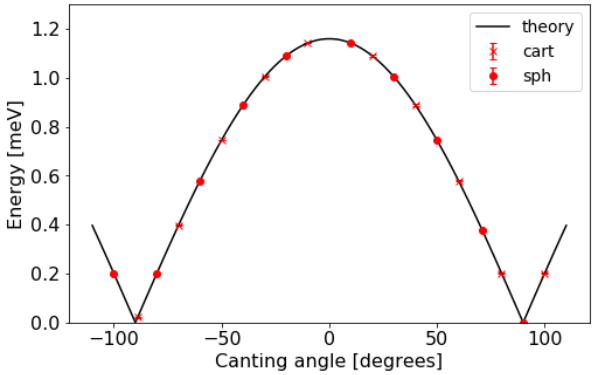

Figure 5.3: Energy as a function of the angle with the z-axis with anisotropy $B_{anis} = 10$ T.

5.3 Temperature

When temperature is added, the spin will start fluctuating randomly. Averages of the spin movement along a specific axis should follow the Langevin curve given by Eq. 5.6.

$$\frac{\langle s^z \rangle}{s} = L(y) = \coth(y) - \frac{1}{y}, \qquad y = \frac{\mu B}{k_B T}. \tag{5.6}$$

To test this a single spin in a magnetic field along the z-axis with non-zero temperature was simulated. The simulation was run for $N = 10^6$ data points, long enough to make sure the spin had reached equilibrium. After this the mean of the z-coordinate of the spin was calculated. This was done for three different magnetic fields and seven temperatures to see if the results would follow Eq. 5.6.
The results of the simulations can be seen in Figure 5.4. Using integration with spherical coordinates the data points were consistently off from the theory. The simulations with Cartesian coordinates show the points following the theory very well.

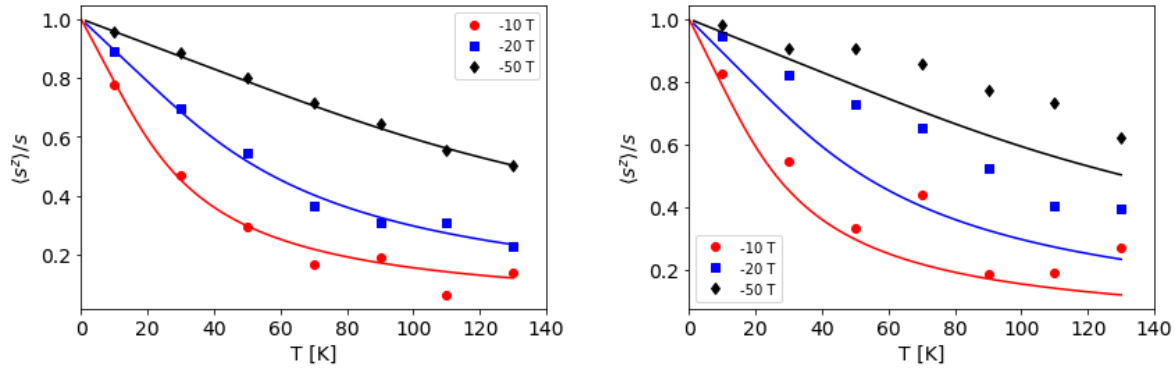

Figure 5.4: Mean of the z-coordinate of a single spin in a field as a function of temperature. The dots are the simulated data and the line the Langevin curve. The simulation has $\mathrm{d}t = 10^{-15}$ s and $N = 10^6$. The left hand graph shows the simulation in Cartesian coordinates, and the right hand graph shows the simulation in spherical coordinates.

5.4 Exchange interaction

To validate the implementation of the exchange field two interacting spins were simulated. We have two spins pointing antiparallel, canted with a slight angle, so they form a v as seen in Figure 5.5a. They have antiferromagnetic interaction with exchange strength $J = 2$ K and spin value $s = \frac{7}{2}$. This will cause them to rotate, in the rotor mode, as discussed in Section 2.4.3. The frequency of rotation as a function of canting angle follows Eq. 2.68. The simulated rotation energy as a function of θ is shown in Figure 5.6. The figure shows the simulated data reproducing the theoretical curve very well for both spherical and Cartesian integration.

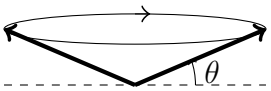

(a) Two spins canted with an angle θ performing the rotor mode precession.

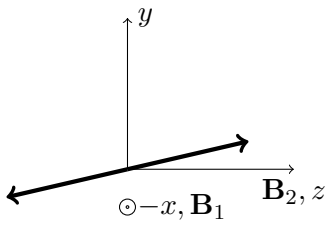

(b) Two spins started in opposite directions, with an easy plane anisotropy $\mathbf{B}_1$ in the yz-plane, and an easy axis anisotropy $\mathbf{B}_2$ along the z-axis.

Figure 5.5

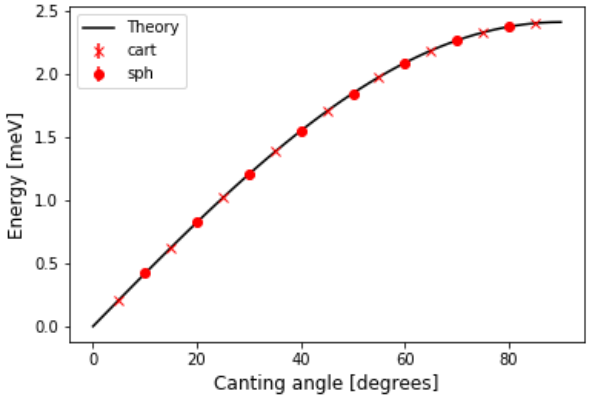

Figure 5.6: The energies of the rotor mode as function of canting angle plotted with the theoretical prediction, for two spins with $J = 2$ K. The data points plotted alternate between spherical and Cartesian integration.

5.5 Anisotropy and exchange interaction

To further validate the anisotropy two spins with exchange interaction, easy axis and easy plane anisotropy were simulated at zero temperature. The directions of the spins and the anisotropies are shown in Figure 5.5b. If they had no exchange interaction the spins would precess freely around the anisotropy easy axis, as the single spin does. However when there is an exchange interaction the spins will have two rotation frequencies. These are described by

the following equations [35]

$$\omega_- = g\mu_B \sqrt{\left(B_2 + \frac{4s}{g\mu_B} J\right)(B_2 - B_1)}, \tag{5.7}$$

$$\omega_+ = g\mu_B \sqrt{B_2 \left(B_2 - B_1 + \frac{4s}{g\mu_B} J\right)}. \tag{5.8}$$

Here B_1 is the anisotropy field in the easy plane in Tesla, B_2 is the anisotropy field in the easy axis in Tesla, J is the exchange constant, and s is the spin value.
We see that the spins do indeed rotate with frequencies $\omega_\pm$ as a function of D_1, D_2 and J in Figure 5.7. The anisotropy strength is given in Kelvin, with the unit conversion described in Section 4.3.1. There is excellent agreement between theory and simulations.

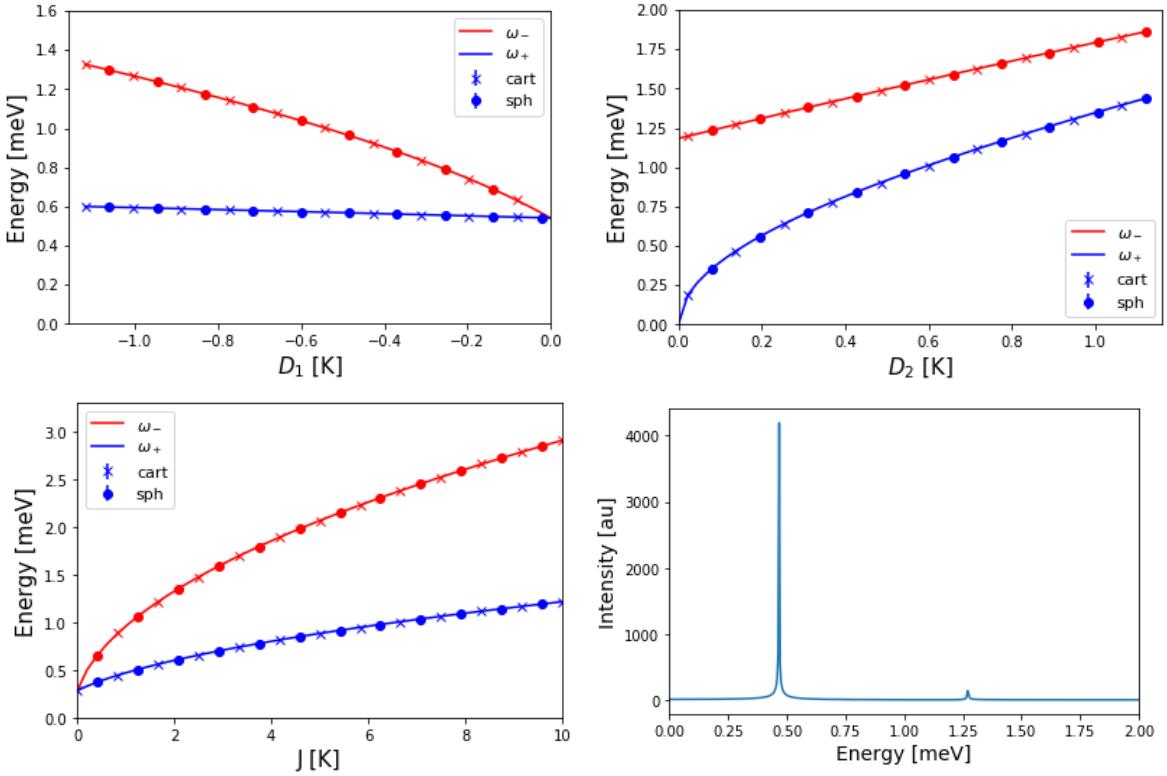

Figure 5.7: Varying D_1, D_2 and J. The solid lines are Eq. 5.7 and Eq. 5.8. The data points are plotted so the ones found with spherical and Cartesian integration alternate. The fourth graph is the intensity spectrum for a simulation with $J = 2$ K, $D_1 = -1.12$ K, and $D_2 = 0.14$ K

To validate the temperature for the two spins, we simulated two spins with two anisotropies and temperature to compare with Henrik Jacobsen's figures [10]. In his thesis he simulated hematite nanoparticles which he then compared to neutron scattering data. A nanoparticle is a particle with a size in the nanometer range, consisting of around 10^4 spins. The spins in the hematite particles move coherently and can thus be simulated as two superspins, one spin to represent each sublattice in the antiferromagnet. The superspins are defined by

$$\sum_{m \in A} \mathbf{s}_m = \mathbf{S}_A, \qquad \sum_{j \in B} \mathbf{s}_j = \mathbf{S}_B, \tag{5.9}$$

and are of the order $\frac{5}{2} \cdot 5 \cdot 10^3$. Here A and B denote the two sublattices.
The results of my simulations are shown in Figure 5.9. The results of Jacobsen's simulations are shown in Figure 5.10 for comparison. The two different simulations show near identical results.
The data shows the peaks on the x- and y-components of the cross section that can be modelled as dampened harmonic oscillators and the rotor mode is seen as a shoulder on the z-component. This rotor mode was discovered by Garde [30] and reproduced by Jacobsen [10], [14] and is when the spins rotate in the yz-plane as in Figure 5.5a. This can be seen when looking at the spin components in Figure 5.8, where the y- and z-components are oscillating at the same time.

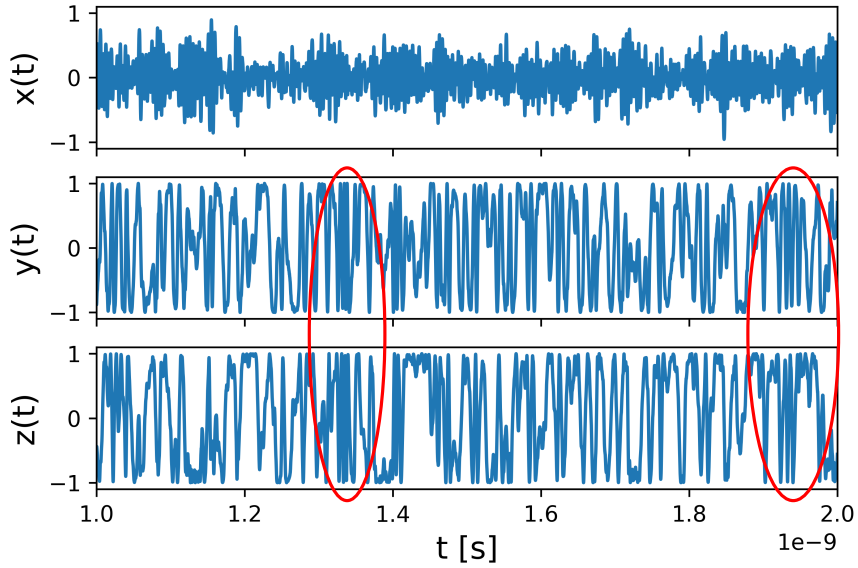

Figure 5.8: Time evolution of one of the spins at $T = 150$ K. Rapid coupled oscillations within the yz-plane are marked by the red ellipses.

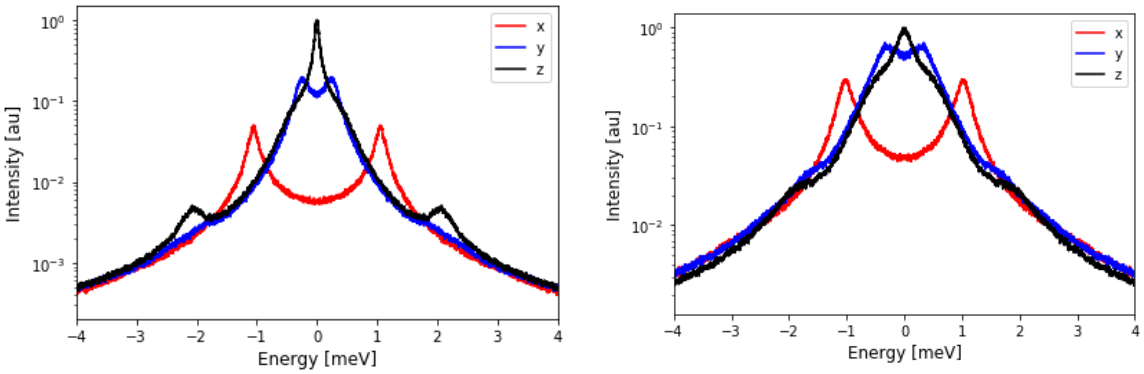

Figure 5.9: Two spins simulated with s =5/2, J =242 K, B_1=-44.6 mT, B_2=4.46 mT, dt = 10^{-15} s, $N = 10^8$, $N_A = 5 \cdot 10^3$. Temperature 50 K (left) and 150 K (right).

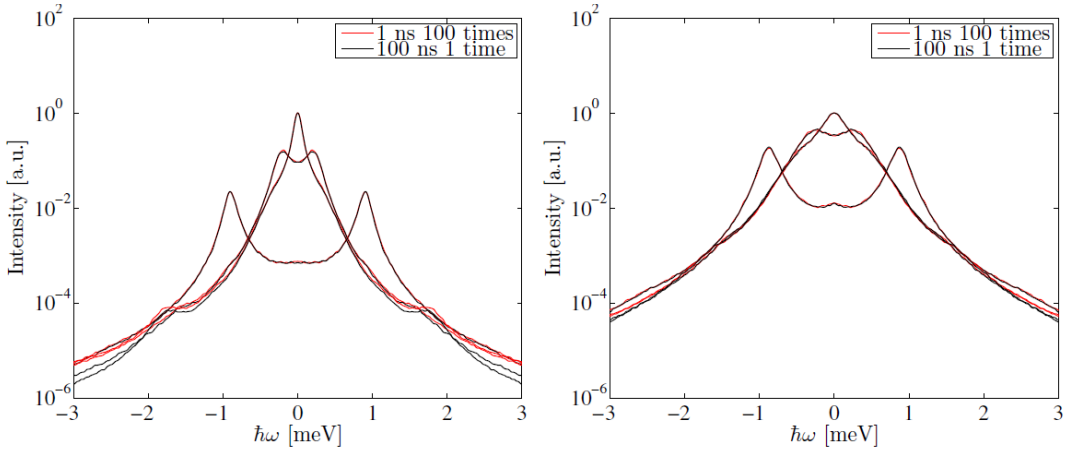

Figure 5.10: Two spins simulated with s =5/2, J =242 K, B_1=-44.6 mT, B_2=4.46 mT, dt = 10^{-15} s, $N = 10^8$, $N_A = 5 \cdot 10^3$. Temperature 50 K (left) and 150 K (right). From Jacobsen [10]

5.6 Ferromagnetic spin chain

A ferromagnetic spin chain with exchange strength $J = 2$ K and spin size $s = \frac{7}{2}$ was simulated in an external magnetic field at $T = 0$. The spins were started in a position close to the ground state, in a spin wave excitation. The spin chain had 12 spins so there were 12 possible modes for the chain, described by

$$\mathbf{q}_j = 2\pi \frac{(x_j - n/2)}{qa} \hat{x} \tag{5.10}$$

Where n is the number of spins and x_j is the mode we consider.
The spin chain will stay in the mode that it is started in when simulating in zero temperature. This means that to see the full dispersion with all 12 modes, the spin chain must be simulated 12 different times, where each time it is started in a different mode. We did this by starting the spins, so they pointed along the z-axis, with very small x and y components dictated by the $\mathbf{q}_j$ mode. The added scattering cross sections of the 12 simulations with a magnetic field of $\mathbf{B} = 1$ K $\hat{z}$ are shown in Figure 5.11 plotted with the dispersion relation for the spin wave, given by Eq. 2.46.

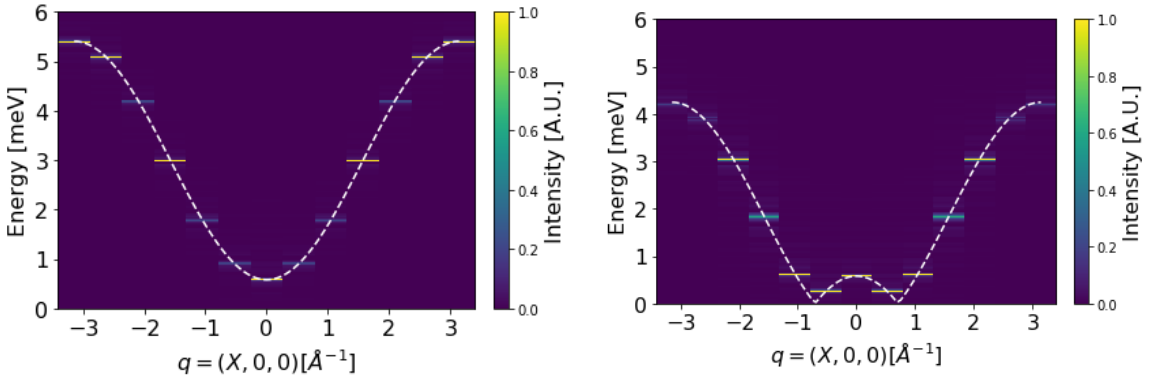

Figure 5.11: The cross section for 12 different simulations of the FM spin chain added together with exchange $J = 2$ K and magnetic field $B = 1$ K. Theoretical dispersion plotted as white dashed line. The left panel has been started with the magnetisation aligned with the field and the right panel with the magnetisation opposite the field.

If the spin starts antiparallel to the field the dispersion shifts downwards as seen in Figure 5.11. This is due to the fact that the ferromagnetic exchange interaction and the Zeeman interaction work against each other, which means the Zeeman term has the opposite sign as Eq. 2.46.
If an easy-axis anisotropy in the z-direction is added it acts like a magnetic field and will shift the dispersion along the energy-axis. The main difference between the effect of anisotropy and magnetic field is that since the anisotropy is not directional it will work add to the effect of the exchange interaction no matter if the spins are in the positive z-direction or the negative z-direction.
When adding temperature to the simulations, we no longer have to simulate the spin chain several times to get several modes. This is due to the fact that with non-zero temperature, the energy of the system can change and thus the spin chain can jump between modes. For small temperatures the temperature broadens the energy peaks, but they still fit the dispersion well as seen in Figure 5.12. For large temperatures the spins no longer form spin waves and therefore the dispersion is not confined to modes, but a continuum in energy, banded by the low T dispersion.

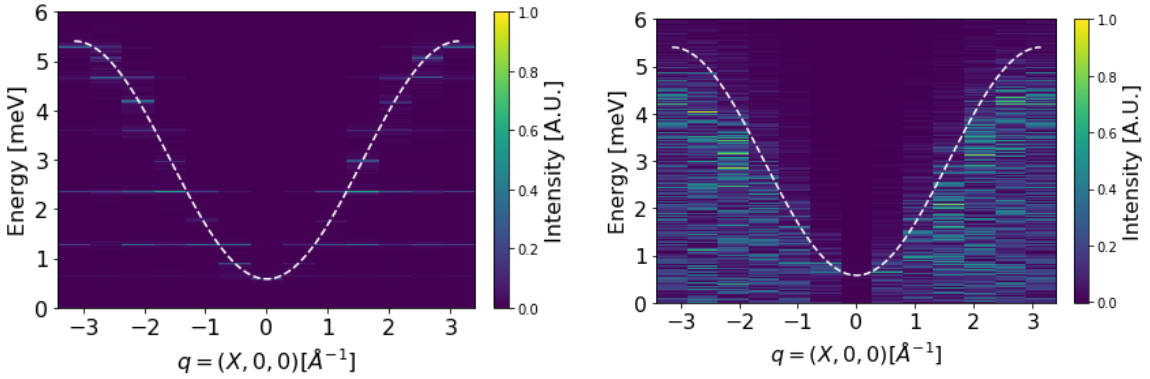

Figure 5.12: The cross section for two simulations of the FM spin chain with exchange $J = 2$ K and magnetic field $B = 1$ K, $N = 2 \cdot 10^6$, $\mathrm{d}t = 2 \cdot 10^{15}$ and different temperatures. Theoretical dispersion plotted as white dashed line. The left panel has $T = 1$ K and the right panel has $T = 50$ K.

5.7 Antiferromagnetic spin chain

An antiferromagnetic spin chain with exchange strength $J = 2$ K and spin size $s = \frac{7}{2}$ was also simulated. As with the ferromagnetic chain the spins were started close to the ground state in a wave formation. The modes are the same as for the ferromagnetic spin chain, but the spins are started antiparallel to their neighbours instead of parallel.
Figure 5.13 shows the spectrum for the antiferromagnetic spin chain without temperature and with two different anisotropies. The dashdotted line is the theoretical dispersion given by Eq. 2.63.

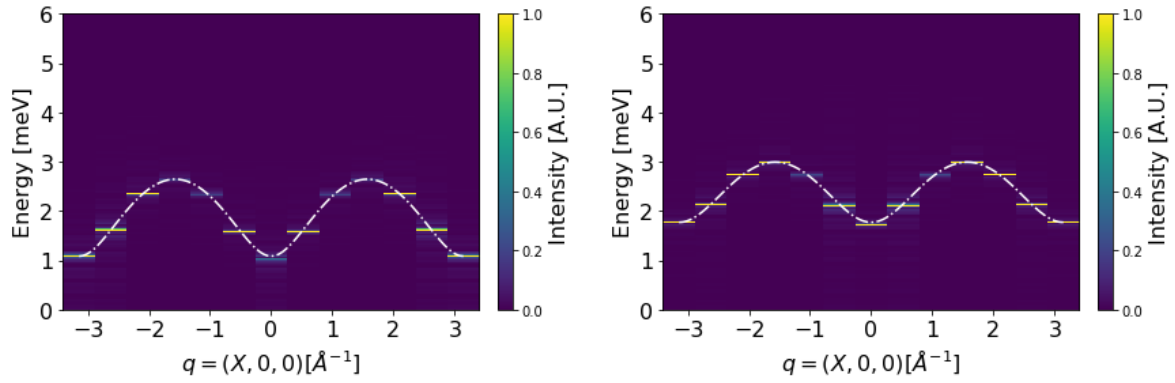

Figure 5.13: The cross section for 12 different simulations of the AFM spin chain added together with exchange strength $J = 2$ K. Theoretical dispersion plotted as white dashed line. The left panel has anisotropy $D = 0.4$ K and the right panel has $D = 1$ K.

The spectrum was also simulated with a magnetic field along the z-axis and no anisotropy, the results of which are shown in Figure 5.14. We can see here that the dispersion splits into two when adding a magnetic field, as predicted in Eq. 2.63.

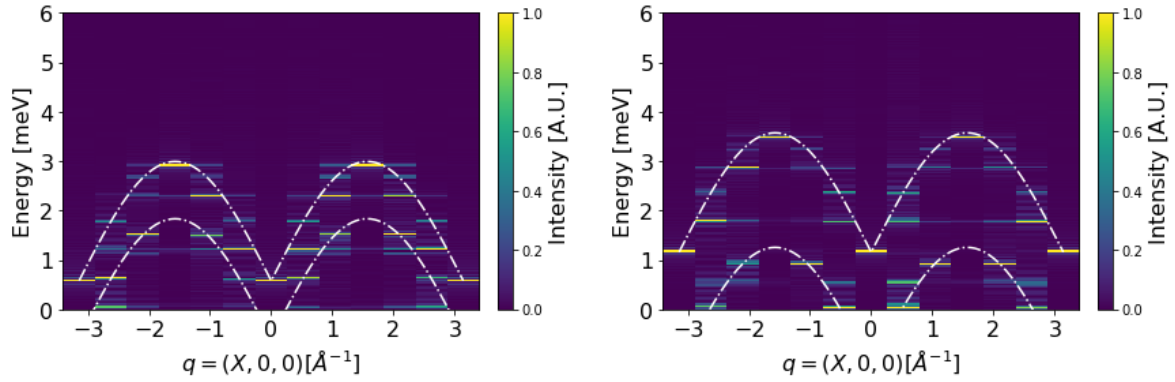

Figure 5.14: The cross section for 12 different simulations af the AFM spin chain added together. Theoretical dispersion plotted as white dash-dotted line. The left panel has magnetic field $B = 1$ K and the right panel has $B = 2$ K.

When simulating the antiferromagnetic spin chain with anisotropy and temperature we see that for low temperatures, the theoretical dispersion is still followed but the peaks are broader like for the ferromagnetic chain. Figure 5.15 shows that at $T = 1$ K, this is the case. The figure also shows that there is a dispersion-less mode at $E \approx 1.3$ meV. This suggests that some

of the spins move independently of each other or all at the same time. The effect was not investigated further due to time constraints. The figure shows that for higher temperatures the energies of the spins no longer follows the theoretical curve but there is a continuum of energies limited by the spin wave dispersion. It is as expected that the order of the spin chain breaks down for higher temperatures, and the system is no longer solely described by well defined spin waves.

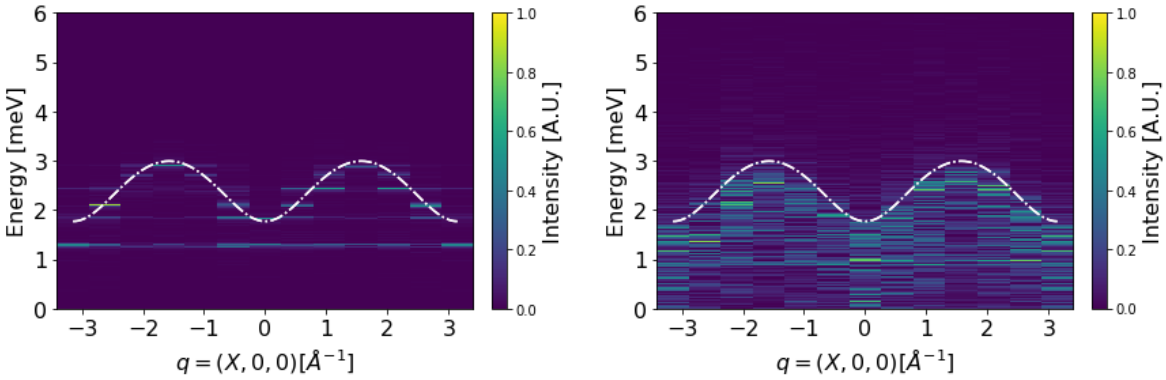

Figure 5.15: The cross section of one simulation of the AFM spin chain with anisotropy $D = 1$ K and temperature. Theoretical dispersion plotted as white dash-dotted line. The left panel has temperature $T = 1$ K and the right panel has $T = 10$ K.

5.8 Triangle with anisotropy

A triangle was simulated with antiferromagnetic exchange $J = 2$ K and varying easy axis anisotropy. The main results are shown and discussed in Chapter 6, but the simulation is discussed briefly here because it demonstrates a difference between the integration in spherical and Cartesian coordinates. The integration in spherical coordinates behaves unpredictably for certain canting angles and anisotropy values, in this case the canting angles 20° and 25° at anisotropy $B_{anis} = 1$ T and $B_{anis} = 2$ T. This is illustrated by the spin movement of one of the canted spins, seen in Figure 5.16, where the spin goes from oscillating with a well defined frequency to moving in a disorganised manner. This does not occur for the integration in Cartesian coordinates.
We do not know the reason this occurs for the integration in spherical coordinates, as time did not permit further investigation.

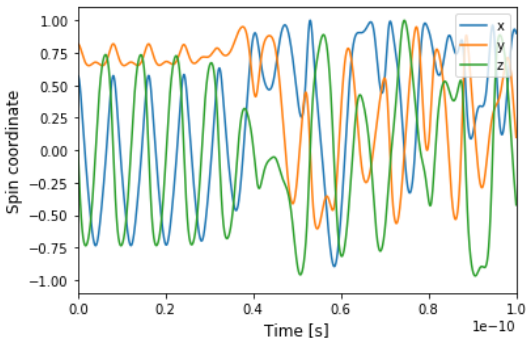

Figure 5.16: The spin components for a spin in a simulated triangle with anisotropy $B_{anis} = 2$ T and $\phi = 25°$ showing the point where the spins start moving unpredictably.

5.9 Time step

The size of the time step in a numerical simulation is very important. If the step is too big the results will be wrong and if it is too small the simulation will take longer time to converge. A range of time steps was simulated to find the optimal time step.

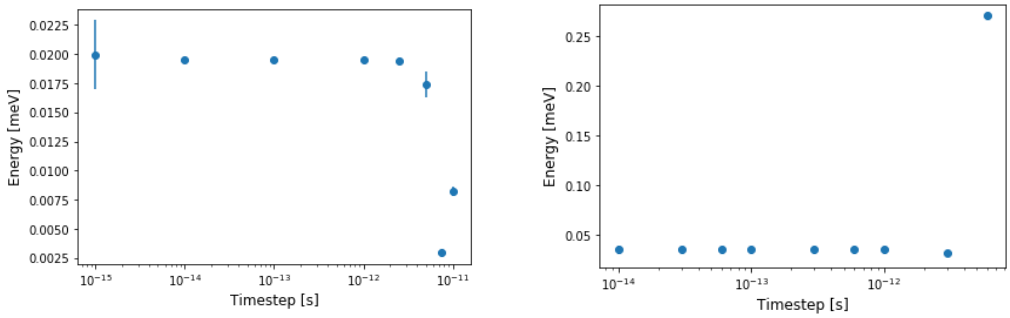

(a) Two spins in zero temperature with antiferromagnetic exchange $J = 186$ mK and varying time steps.

(b) Three spins in zero temperature with antiferromagnetic exchange $J = 186$ mK and varying time steps.

Figure 5.17

Figure 5.17 shows the energy of two spins and three spins rotating for different time steps. This figure shows that for a range of time steps the energy is seen equally well, but when the time step becomes too large the energy of the system seems to change. This is the result of the time step being too large to properly make out the oscillations of the spin, and instead makes it look like the spin moves differently.

Another important parameter is the length of the simulation. If the total simulation time $N \cdot \mathrm{d}t$ is not long enough the energy resolution becomes too large to properly make out the excitation peaks. Examples of this are seen in Figure 5.18 where the 1 ns peak is very wide and angular, both for the two and three spin simulations. This effect can be predicted from the Heisenberg uncertainty principle $\Delta E \Delta t \geq \hbar/2$. Here $\Delta E = 1.5 \cdot 10^{-3}$ meV is given by the half width at half max of the excitation peak, and $\Delta t = 0.38$ ns is the standard deviation of a Gaussian fit of a step function with width 1 ns. Inserting this we get

$$\Delta E \Delta t = 3 \cdot 10^{-6} \cdot 1.602 \cdot 10^{-19}\mathrm{J} \cdot 0.38 \cdot 10^{-9}\mathrm{s} = 0.91 \cdot 10^{-34}\mathrm{J} \cdot \mathrm{s}, \tag{5.11}$$

which is larger than $\hbar/2 = 0.53 \cdot 10^{-34}$ J $\cdot$ s.
The time step was chosen to be $\mathrm{d}t = 10^{-13}$ s for both the two spins and the triangle as this was small enough to accurately depict the energies of the system.

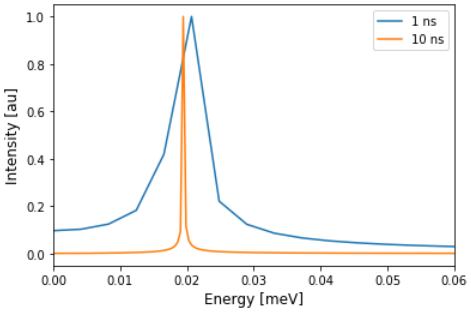

(a) Intensity spectra for the two spin simulations with the shortest simulation times.

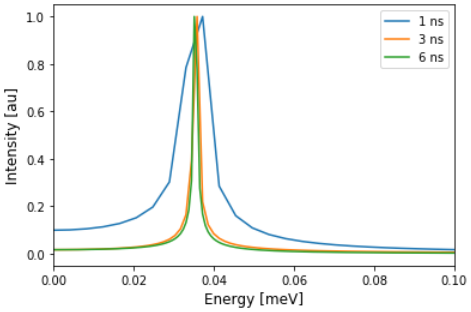

(b) Intensity spectra for three spin simulations with shortest simulation times.

Figure 5.18

5.10 Total simulation time

When adding temperature to the simulations it perturbs the spin system by thermal fluctuations and it is important to make sure the simulations run for long enough for the spins to reach a thermal equilibrium. The time it takes for the spins to reach equilibrium is dependent on the size of the damping factor λ and the temperature T. The larger they both are, the faster the spins reach equilibrium, but the broader the features in the energy axis. The damping factor can also be adjusted, but we chose to skip this to focus on more influential factors.

To determine how long simulation time was needed to reach equilibrium we simulated a triangle in temperature for 100 ns and looked at the scattering function for 10 ns intervals to see when it stopped changing. The calculated power spectra for the scattering function are seen in Figure 5.19a. The first 20 ns strange things show up. From 20 ns onwards we see there are peaks at two different energies, depending on the time interval either one or both show up. This suggests the chosen interval time is too small to get convergent spectra. Looking at intervals of 30 ns instead we get the five power spectra in Figure 5.19b. These are more similar, and it can be seen that the peak positions and the shape of the spectrum is stable after 30 ns. There are still differences in peak shape and size in the power spectra after 30 ns. This can be helped by transforming longer time intervals to find the power spectra. This is shown in Figure 5.20. These spectra are much more uniform, with similar profiles. This shows that the power spectra converge after about 60 ns.

All triangle simulations with temperature have run for 100 ns and the power spectra have been calculated for the last 60 ns. The simulations of the kagomé lattice have run for 500 ns and the power spectra have been calculated for the last 400 ns, to be absolutely sure equilibrium was reached and the power spectra converge.

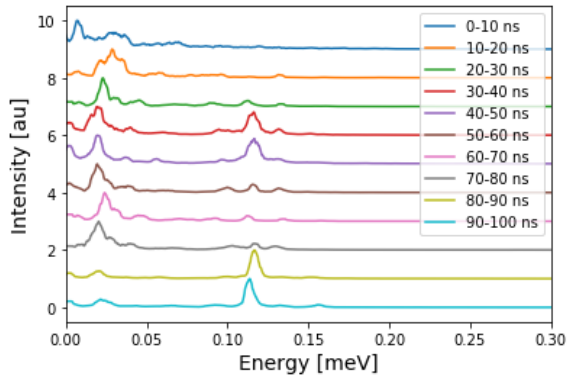

(a) Intensities calculated from 10 ns time intervals from a simulation of a triangle with time step $\mathrm{d}t = 10^{-13}$ s, AFM exchange $J = 186$ mK, temperature $T = 20$ mK and easy plane anisotropy $D = 80$ mK in the local xy-plane. Intensities offset with one along the y-axis.

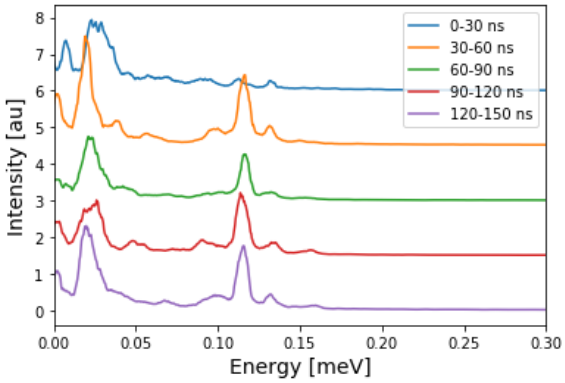

(b) Intensities calculated from 30 ns time intervals from a triangle with time step $\mathrm{d}t = 10^{-13}$ s, AFM exchange $J = 186$ mK, temperature $T = 20$ mK and easy plane anisotropy $D = 80$ mK in the local xy-plane. Intensities offset with one along the y-axis.

Figure 5.19

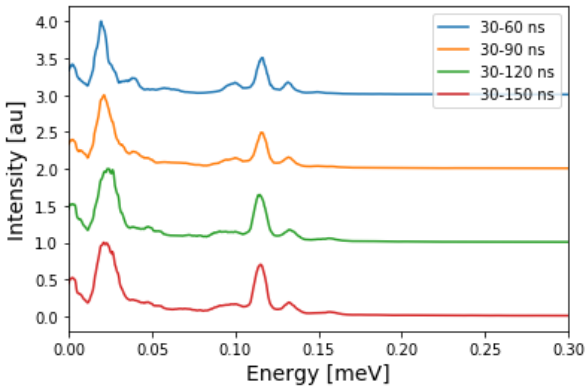

Figure 5.20: Intensities calculated from increasing time intervals, starting at 30 ns from a simulation of a triangle with time step $\mathrm{d}t = 10^{-13}$ s, AFM exchange $J = 186$ mK, temperature $T = 20$ mK, easy plane anisotropy $D = 80$ mK in the local xy-plane. Intensities offset with one along the y-axis.

5.11 Discussion

We have done extensive validation on the code, for physical and non-physical parameters. The physical parameters, exchange interaction J, single-ion anisotropy D, external magnetic field B and temperature T, were validated both for integration in spherical and Cartesian coordinates. This was done because the simulations in spherical coordinates gave weird outputs. The simulations in spherical coordinates give correct results for several simulations in zero temperature, namely for one and two spins, but become unstable when simulating three spins in zero temperature. The results from simulations in spherical coordinates with temperature also do not align with theory. We have not found the exact cause of this, but speculate that the instability might stem from the factor of $1/\sin(\theta)$ in the equation of motion, Eq. B.9. This factor approaches infinity for $\theta \to 0$ and thus might lead to the change in angle becoming very large, invalidating the fundamental assumption that $\mathrm{d}\theta$ and $\mathrm{d}\phi$ are small.

A possible work-around might be to reduce dt.
The spherical coordinates were implemented to eliminate the error introduced when normalising the spin at every time step, as is necessary in Cartesian coordinates. This was not a good solution as the normalising error is significantly smaller than the errors introduced when simulating in spherical coordinates. Furthermore the error from normalising the spin length can only build up, when the spins are in non-zero temperature. The addition of temperature means the spins will be more affected by the temperature, than they are by the error and we can thus ignore it in this case.
The simulations using integration in Cartesian coordinates have been consistently in agreement with analytical calculations over a variety of different systems with a combination of different factors. The implementation of the Zeeman interaction, temperature, nearest neighbour exchange interaction and the anisotropy interaction have all been validated independently, and in combination. This was done by comparing to theoretical predictions. One and two spins were simulated with different interactions and shown to faithfully reproduce theory. A one-dimensional spin chain was simulated with ferro- and antiferromagnetic exchange, magnetic field, temperature, and periodic boundary conditions. These results reproduced the theoretical dispersion relations.
The two spin simulation with antiferromagnetic exchange, easy axis and easy plane anisotropy, and temperature, faithfully reproduced results from Jacobsen's thesis [10] which have been verified by neutron scattering experiments.
We can conclude that we can accurately simulate the dynamics of any system of spins, including exchange interactions, local and global anisotropies, applied magnetic fields and temperature effects.

For the accuracy of the simulations it is also very important that the non-physical parameters are correct. We have focused on three non-physical parameters, namely the size of the time step dt, the total simulation length $N \cdot \mathrm{d}t$ and the time interval included in the calculation of the power spectrum. The size of the time step needs to be small enough that it accurately depicts when the spin oscillates, and that the approximations used when integrating the equations of motion are valid. An upper bound was determined by simulating two and three spins with antiferromagnetic exchange $J = 186$ mK, canted away from equilibrium, with several different time steps and finding the excitation energy of the systems. We found the maximum time step that still gave the correct results to be 10^{-12} s, any size smaller than this would also give correct simulation results. The downside to having a small time step is that the number of simulated points needs to increase to get the same simulated time which means the simulations overall take longer time to run. With the exchange parameters and anisotropy constants used in this thesis we found a reasonable compromise to be $\mathrm{d}t = 10^{-13}$ s.
The total simulated time determines the energy resolution of the power spectrum in accordance with the Heisenberg uncertainty principle. Therefore it is important to have a long enough simulation that we can make out the excitations of the system. We tested this without temperature and found that the simulated time has to be at least 10 ns for the two spins and 6 ns for the three spin simulation. We did not investigate this for bigger systems, but do not expect these times to change significantly if all other parameters are the same.
When simulating with finite temperature another demand is placed on the total simulated time. That is because the simulation needs to run long enough that the simulated system reaches thermal equilibrium, and longer so a power spectrum can be calculated for the system in equilibrium. To place a lower limit on the simulation time needed to reach equilib-

rium, we simulated a triangle with antiferromagnetic exchange $J = 186$ mK, easy plane anisotropy $D = 80$ mK and temperature $T = 20$ mK, and calculating the power spectrum for different time intervals of the simulation. Equilibrium was clearly not reached during the first 30 ns, as the power spectra changed drastically. Calculating the power spectrum over different size time intervals, starting at 30 ns showed that the spectrum converged when including at least 60 ns.
This means that when simulating without temperature it is only necessary to simulate at least 10 ns, but when simulating with temperature it is important to simulate for at least 90 ns to make sure the system reaches equilibrium and the power spectrum of the spin movement converges.
This led to the safe choice of a total simulation time of 100 ns for the triangle and 500 ns for the kagomé lattice, with power spectra calculated from the last 60 ns and 400 ns respectively. The kagomé simulations took approximately 8 hours on a stationary computer.

Chapter 6

Results

In this chapter we will describe simulations of two frustrated systems to see to what extent they are able to replicate the observed magnetic dynamics of GAG. The systems simulated are a triangle and 3×3 unit cells of a kagomé lattice with antiferromagnetic exchange and different anisotropy directions. The results are compared with experimental data for GAG.

6.1 Triangle at zero temperature

We simulate three antiferromagnetic spins in a triangle with $s = 7/2$ and $J = 2$ K. The spins are started with the top spin pointing along the y-axis and the two lower spins canted away from the ground state with an angle ϕ as shown in Figure 6.1a. When there is no external field or temperature this means they will move in a zero mode with a set frequency.
If there is no anisotropy this frequency depends on the canting angle as given by Eq. 2.70 where $\phi = \theta - 30°$.
If there is anisotropy along the local z-axis of the spins this will determine the frequency of the zero mode for small values of ϕ. This can be seen in Figure 6.1b. Around $\phi = 0$ the shape of the graph looks like the simulation for a single spin with anisotropy in Figure 5.3, whereas for $|\phi| \gg 0$ the energy dependence looks more like the theoretical energy dependence of a triangle with no anisotropy.

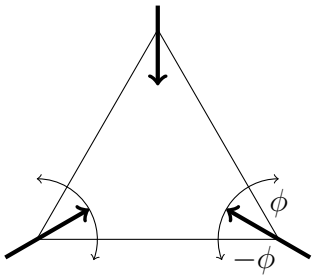

(a) Three spins in a triangle, two of them are being canting with angle ϕ or $-\phi$.

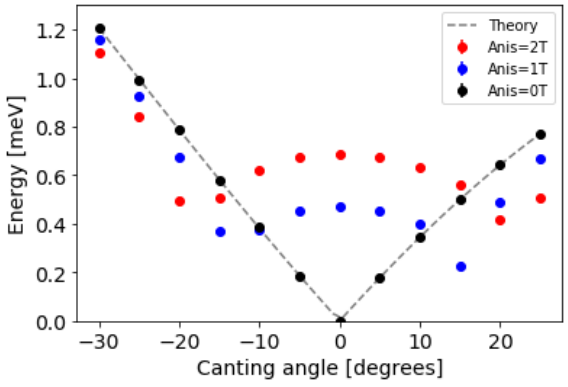

(b) The peak energy as a function of canting angle for different values of the easy axis anisotropy. Simulated in Cartesian coordinates

Figure 6.1

6.2 Triangles at elevated temperatures

We will move on to simulating three spins in a triangle with temperature, a system as yet without theoretical predictions for its dynamics. To make this comparable to inelastic neutron scattering data on GAG we take the spin to be $s = 7/2$, the antiferromagnetic exchange constant to be $J = 186$ mK and temperatures in the range $1 - 200$ mK. Since there is currently no data on the size of the anisotropy in GAG the anisotropy is taken to be the same order of magnitude as the exchange to see how both influence the system.

6.2.1 Triangle with no anisotropy

Simulating a triangle in temperature resulted in a narrow peak at $E = 6 \cdot 10^{-4}$ meV at both $\mathbf{q} = (0, 0)$ and $\mathbf{q} = (1/3, 1/3)$ and a broader, higher energy peak at $\mathbf{q} = (1/3, 1/3)$. The two peaks of the $\mathbf{q} = (1/3, 1/3)$ spectrum can be seen in Figure 6.2a with a fit of two Lorentzian functions for $\mathbf{q} = (1/3, 1/3)$ respectively. The Lorentzian functions are given by

$$L(x) = \frac{A\Gamma^2}{(x-\mu)^2 + \Gamma^2}, \tag{6.1}$$

$$I(\omega) = L_1(\omega) + L_2(\omega) = \frac{A_1\Gamma_1^2}{(x-\mu_1)^2 + \Gamma_1^2} + \frac{A_2\Gamma_2^2}{(x-\mu_2)^2 + \Gamma_2^2}. \tag{6.2}$$

where the parameters are the amplitude A, the mean μ and the full width at half maximum of the peak Γ. The excitation peaks are expected to have a Lorentzian line shape for finite excitation lifetimes.
The mean μ of the Lorentzian functions were taken to be the energy of the peak and the width Γ of the Lorentzian as the errorbar. The energies as a function of temperature is shown in Figure 6.2b. The figure shows that the lower energy mode stays constant in temperature, but the broader higher energy mode increases in energy with temperature. It also grows broader and less well defined.

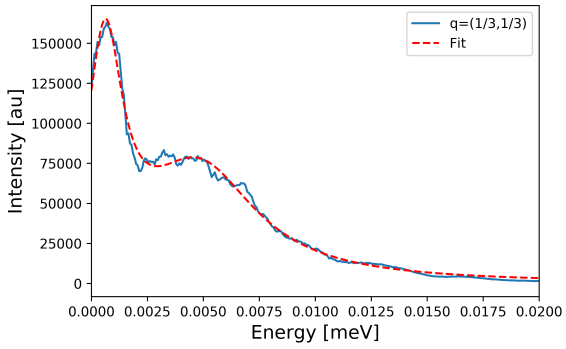

(a) Intensity for $\mathbf{q} = (1/3, 1/3)$ as a function of energy for a simulated AFM spin triangle with $J = 186$ mK and $T = 4$ mK. A double Lorentzian fit is plotted in dashed red.

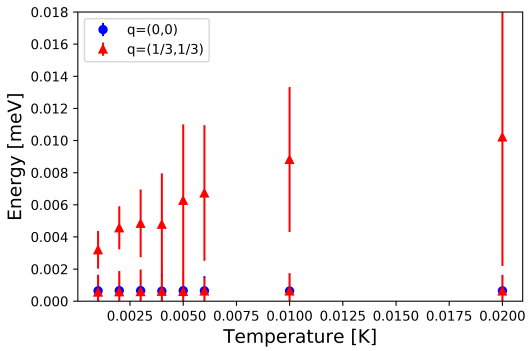

(b) Energy of simulated antiferromagnetic spin triangle with $J = 186$ mK as function of temperature calculated for two different q-values.

Figure 6.2

6.2.2 Triangle with anisotropy in local z-axis

Next a triangle with easy axis anisotropy was simulated. The anisotropy axis for each spin was along its local z-direction as seen in Figure 6.3.

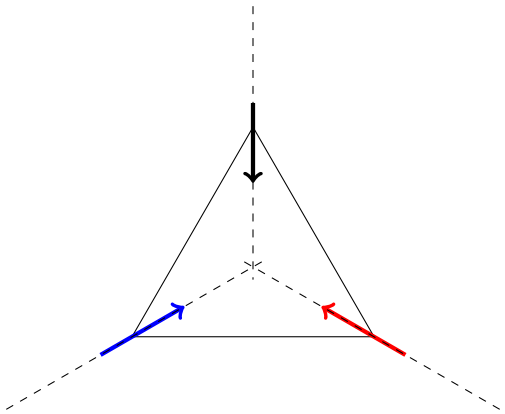

Figure 6.3: Three spins in a triangle with anisotropy axes shown by dashed lines.

To understand the simulations we start by looking at the movements of the spins in real space, an example of which is seen in Figure 6.4a. This shows the movement of the three spins with exchange constant $J = 186$ mK, temperature $T = 90$ mK, and anisotropy $D = 80$ mK. The figure shows the spins placed in the origin, but it is important to note that in the simulations the spins are placed in the corners of a triangle. The spins oscillate around their local z-axis, which is the ground state position of the spins. The spin distance from local z increases with increasing temperature or decreasing anisotropy. An example of this is seen when comparing Figures 6.4a and 6.4b where the spin movement extends much further from the local z-axis when the anisotropy is halved. This shows the temperature pushing the spins away from the equilibrium position. We can also conclude the anisotropy in this regime has a larger restraining effect on the spins than the exchange interaction, when comparing with the zero anisotropy simulation where the spin movements were significantly less well-defined.

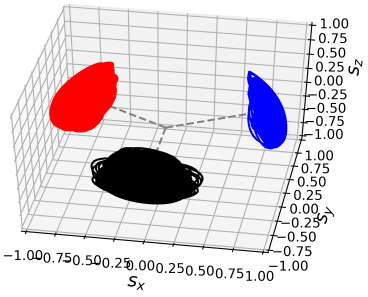

(a) Spin movement of the three spins in the triangle with $J = 186$ mK, $T = 90$ mK, and $D = 80$ mK. The colours of the spin movements corresponds to the same colour spin in Fig. 6.3. The local z-axes are shown as dashed lines.

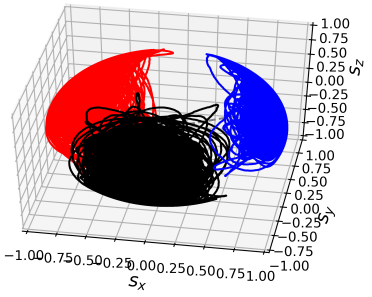

(b) Spin movement of the three spins in the triangle with $J = 186$ mK, $T = 90$ mK, and $D = 40$ mK. The colours of the spin movements corresponds to the same colour spin in Fig. 6.3. The local z-axes are shown as dashed lines.

Figure 6.4

Taking a step further in the analysis, we look at the scattering cross section $S(\mathbf{q}, \omega)$ for the spins. Two of the scattering cross sections can be seen in Figure 6.5 along with fits of two Lorentzian functions.
Figure 6.5a shows two sharp peaks at $\mathbf{q} = (0, 0)$, indicating there are two rotational modes in the system. This is an example of when the anisotropy and/or exchange interaction was dominating over the temperature, which resulted in well defined peaks. Figure 6.5b shows a spectrum where the temperature dominates. The spectrum is noisy, and the peaks are broader and less well defined.
To see how the energies of the modes behaved when changing anisotropy, temperature and exchange constant the spectra were fitted with two Lorentzian functions for $\mathbf{q} = (0, 0)$ and three for $\mathbf{q} = (1/3, 1/3)$. These plots are shown in Figures 6.6a, 6.6b and 6.6c.
Here we see first of all that the energies when looking at the different $\mathbf{q}$-values $\mathbf{q} = (0, 0)$ and $\mathbf{q} = (1/3, 1/3)$ are the same with the exception of the peak at $E = 0$ for $\mathbf{q} = (1/3, 1/3)$. This peak originates from the static structure, and shows up because of the placement of the spins in the lattice, not because of the movement of the spins.

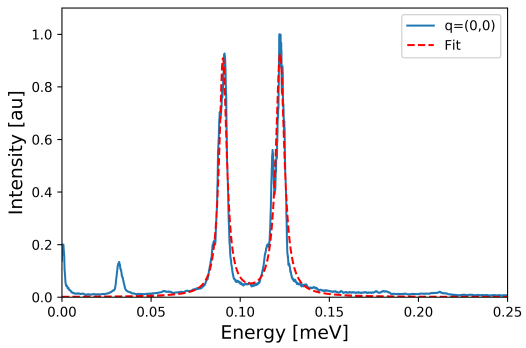

(a) Cross section of three spin simulation with $J = 186$ mK, $T = 90$ mK, and $D = 80$ mK.

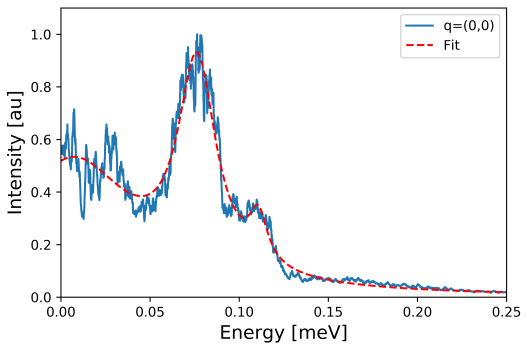

(b) Cross section of three spin simulation with $J = 186$ mK, $T = 500$ mK, and $D = 80$ mK

Figure 6.5

Figure 6.6a show that the non-zero energies increase with increasing anisotropy. The large errorbars on the points with low anisotropy are a sign that the peaks become broad and less well defined. This broadening of the peaks also happens for large temperatures as is seen on the spectrum in Figure 6.5b. This indicates that when the temperature dominates over the anisotropy interaction it leads to the spin having a short lifetime, leading to a less well-defined oscillation and therefore a broader energy spectrum.
In contrast to the simulated triangle without anisotropy Figure 6.6b shows the energy of the spins decreasing with increasing temperature. The two cases do have different energy scales, $E \sim 10^{-3}$ meV for the simulations with no anisotropy and $E \sim 10^{-1}$ meV for the simulations with anisotropy. This likely means that the two graphs represent two different excitations. When increasing the exchange constant the energies increase as seen in Figure 6.6c. This is as expected.

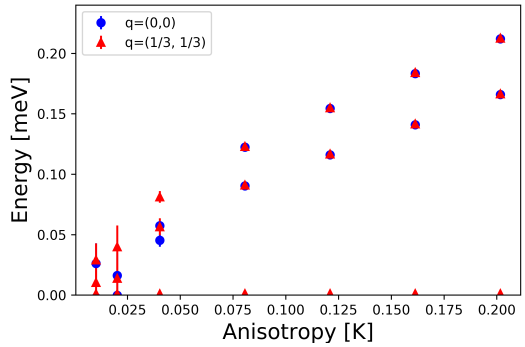

(a) Excitation energies as a function of anisotropy for a simulated triangle with $J = 186$ mK and $T = 90$ mK.

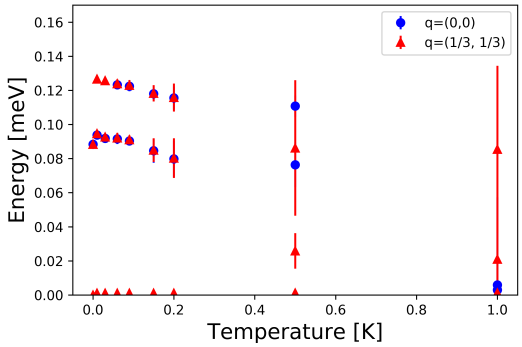

(b) Excitation energies as a function of temperature for a simulated triangle with $J = 186$ mK and $D = 80$ mK.

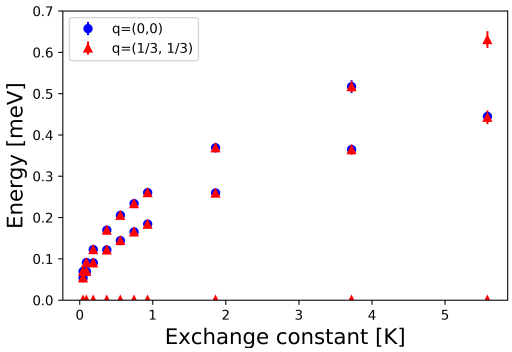

(c) Excitation energies as a function of exchange constant for a simulated triangle with $D = 80$ mK and $T = 90$ mK.

Figure 6.6

6.2.3 Triangle with anisotropy in local *xy*-plane

Next we simulated the three spins with anisotropy in the local xy-plane. This more closely mimics the behaviour of the spins in GGG and GAG [20]. Looking at the spin movement in Figure 6.7 we see that the spins are no longer confined to a circle around the local z-axis. In fact it looks more like they are pointing tangential to the triangle and rotating along the z-axis. This makes sense because we expect the ground state for this anisotropy to be as presented in Figure 6.7c. Figures 6.7a and 6.7b show the two versions of the spin state in the simulations. There are no clear correlations in the data between the value of the anisotropy or temperature and which of the two states the spins have.
The spin movement narrows in x and y when the anisotropy increases or the temperature decreases.

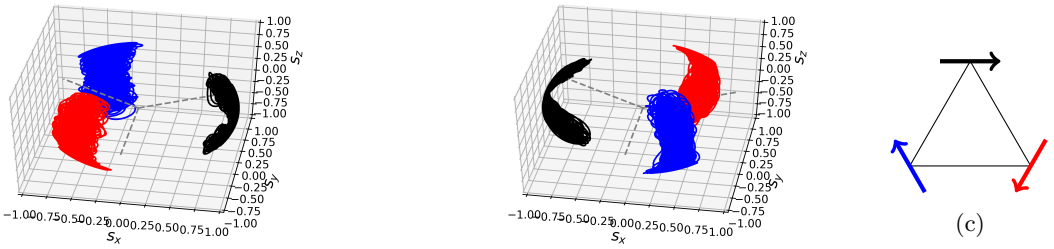

(a) $J = 186$mK, $T = 20$mK, and $D = -80$mK

(b) $J = 186$mK, $T = 20$mK, and $D = -160$mK

Figure 6.7: (a), (b) Spin movement of the three spins in the triangle with local xy anisotropy, showing the two possible spin configurations. The colours of the spin movements, corresponds to the same colour spin in (c). The local z-axes are shown as dashed lines. (c) The approximate spin configuration for the spin movement shown in (a).

As before we look at the scattering cross section of the movement, illustrated in Figure 6.8. There are several things that are different. First and foremost the spectrum has more peaks. At $\mathbf{q} = (0, 0)$ there are two main peaks and the higher energy peak has two smaller neighbouring peaks. These small neighbouring peaks were quite difficult to fit, hence the fit of two Lorentzian functions for the $\mathbf{q} = (0, 0)$ spectrum.
We can see that two of the peaks of the $\mathbf{q} = (1/3, 1/3)$ spectrum are at the same energies as for $\mathbf{q} = (0, 0)$, and there is a structural peak at $E = 0$ as before. Four added Lorentzians were fitted to the $\mathbf{q} = (1/3, 1/3)$ spectra to describe all the peaks.

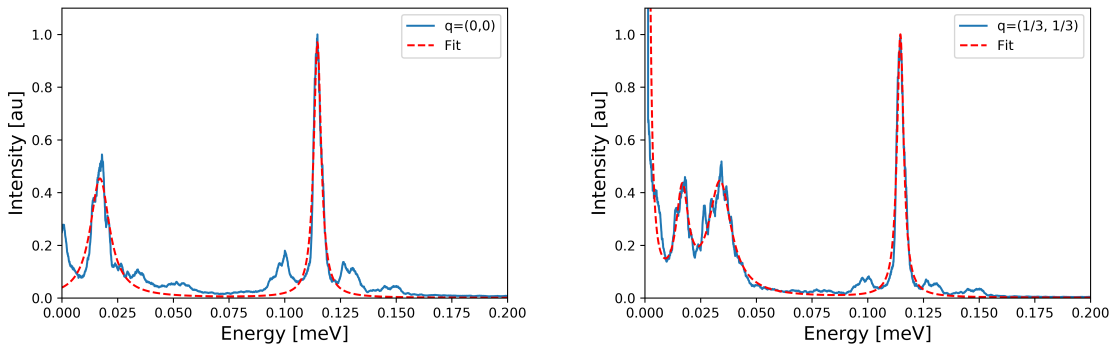

Figure 6.8: Cross section of spin movement with $J = 186$ mK, $T = 20$ mK, and $D = -80$ mK, shown with Lorentzian fits plotted in red. The right hand graph has $\mathbf{q} = (0, 0)$ and the left hand graph has $\mathbf{q} = (1/3, 1/3)$.

Two Lorentzians are fitted to the $\mathbf{q} = (0, 0)$ data and four to the $\mathbf{q} = (1/3, 1/3)$ to describe the spectra. The means and widths of the peaks are used to define the energy of the excitations and the error on this energy. These can be seen plotted in Figure 6.9 for varying anisotropy values and varying temperature.
The high energy peak has a clear dependence on anisotropy, with the energy of the excitations decreasing as the size of the anisotropy decreases.
It is difficult to say whether the placement of the lower energy peaks depend on anisotropy. It looks like there is a decrease in energy with the decrease in anisotropy strength.

The energy of the lower peaks seems to increase as the temperature increases. The energy of the high peaks seem to decrease and then stay constant as the temperature increases.

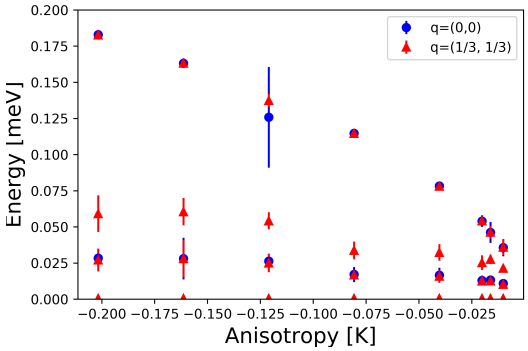

(a) Excitation energies as a function of anisotropy for a simulated triangle with $J = 186$ mK and $T = 20$ mK.

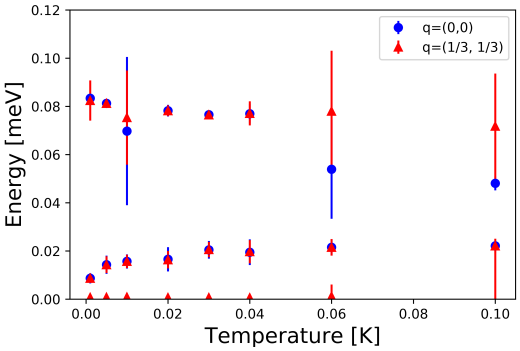

(b) Excitation energies as a function of temperature for a simulated triangle with $J = 186$ mK and $D = -40$ mK.

Figure 6.9

6.3 Kagomé lattice at zero temperature

A 2D kagomé lattice consisting of 27 spins was simulated with antiferromagnetic nearest neighbour exchange. The kagomé lattice has two ground states the $\mathbf{q} = 0$ mode shown in Figure 3.1b and the $\sqrt{3} \times \sqrt{3}$ state seen in Figure 6.10a [15].
For the simulation with zero temperature we chose to focus on the $\sqrt{3} \times \sqrt{3}$ mode as it has a zero mode moving in a loop of six spins compared to a line-shaped zero mode extending through the whole structure in the $\mathbf{q} = 0$ state. The chosen mode is akin to the previously discussed triangle zero mode where one spin is stationary and two spins canted away from the ground state rotate freely as illustrated in Figure 6.10a.
For the simulation at zero temperature the expected zero mode energy relation is given by Eq. 2.71. As with the triangle the θ in the equation is the spins' angle with the x-axis. The canting angle is defined by $\phi = \theta - 30°$. The simulated energy at $\mathbf{q} = 0$ is plotted with the theoretical value in Figure 6.10b. The simulated and theoretical energies show excellent agreement.

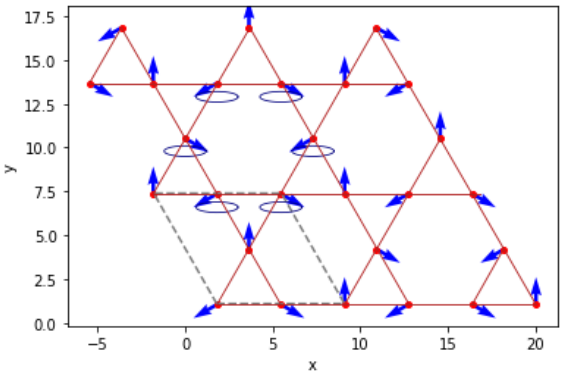

(a) Spin positions of the spins in the kagomé lattice in the $\sqrt{3} \times \sqrt{3}$ mode. Unit cell marked by dashed line. The state shown has continuous degeneracy as the spins on a hexagon can can be rotated out of the plane as indicated by the ellipses without changing the ground state energy.

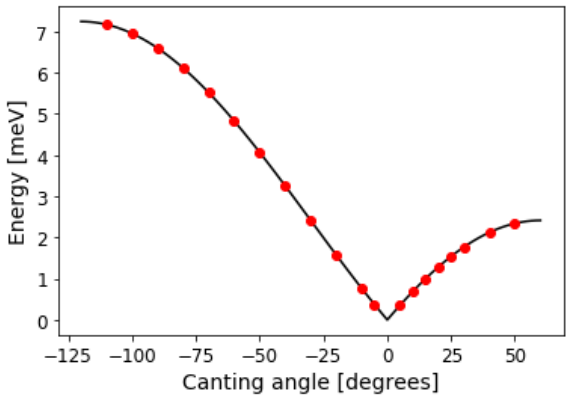

(b) The zero mode of the canted spins in a kagomé lattice, with $s = 7/2$, $J = 2$ K and $T = 0$ K, plotted with the theoretical energy as given by Eq. 2.71

Figure 6.10

The unit cell of the lattice contains three spins in an equilateral triangle, like the system simulated earlier. To see the full behaviour of spins on a kagomé lattice, such as the $\sqrt{3} \times \sqrt{3}$ mode, we need to simulate more unit cells. Three times three lattice unit cells were simulated, to make sure the spins spanned the magnetic unit cell of the $\sqrt{3} \times \sqrt{3}$ and the boundary conditions would result in the edge spins having neighbouring spins with the correct directions. It was simulated with periodic boundary conditions in the x- and y-directions to make sure all spins functionally had four neighbours.

Simulating several unit cells means the scattering cross section can be calculated for several relevant $\mathbf{q}$-values. We found the $\mathbf{q}$-values for which we could expect elastic peaks in Ch. 3. For nuclear scattering we expect peaks at $\mathbf{q} = (0,0), (2,0), (0,2), (2,2)$ and for the magnetic scattering we expect peaks when one or both of the coordinates were odd integers, for example $\mathbf{q} = (0,1), (1,0), (1,1)$. To find where there might be inelastic peaks, we look at the constraints placed by the periodic boundary conditions. This means the spin value is the same for the 0th spin and the Nth spin. Looking at the spins along the x-axis:, we have spin coordinates: $\mathbf{r}_0 = 0$, $\mathbf{r}_N = 3\mathbf{a}$

$$\exp(i\mathbf{r}_0 \cdot \mathbf{q}) = \exp(i\mathbf{r}_N \cdot \mathbf{q}) = 1 \tag{6.3}$$

$$i2n\pi = i\mathbf{r}_N \cdot \mathbf{q} = i3\mathbf{a}(h\mathbf{a}^* + k\mathbf{b}^*) = i3h \cdot 2\pi \tag{6.4}$$

$$h = \frac{n}{3}, \tag{6.5}$$

where n is an integer number. We can perform the same calculation for the y-direction with the spin coordinate $\mathbf{r}_N = 3\mathbf{b}$ to get

$$k = \frac{m}{3}, \tag{6.6}$$

where m is an integer number. This means that the relevant $\mathbf{q}$-values for inelastic scattering are $\mathbf{q} = \left(\frac{n}{3}, \frac{m}{3}\right)$, with $n, m \epsilon 0, 1, 2$. Taking all of these would mean looking at a lot of different cross sections, but due to the symmetries in the lattice there are only a few unique cross sections. We choose to focus on the $(h, 0)$ directions: $\mathbf{q}$ = (0,0), (1/3,0), (2/3,0), (1,0), (4/3,0),

(5/3,0) and the (h, h) direction: $\mathbf{q}$ = (0,0), (1/3, 1/3), (2/3, 2/3), (1, 1), (4/3, 4/3), (5/3, 5/3).

6.4 Kagomé lattice with temperature

We are interested in comparing simulations to GAG data on the hyperkagomé and our fist step is to simulate this simpler system. For this reason the spin value was chosen to be $s = 7/2$, the nearest neighbour exchange was chosen to be $J = 186$ mK as for GAG [4], and the temperatures chosen to be the same order of magnitude as the ones in the paper T=1 − 100 mK. The simulations were done both without anisotropy and with different anisotropy configurations. Since the anisotropy strength for GAG is not given in the literature [4], the anisotropy strength was chosen to be $D = 80$ mK, a comparable size to the exchange interaction. The four types of anisotropy simulated were anisotropy with local z-axis as the easy axis, easy plane anisotropy in the local xy-plane, easy axis anisotropy in global z, and easy plane anisotropy in the global xy-plane. The single ion anisotropy has strength $D = 80$ mK for all of the spins.

6.4.1 Kagomé lattice with no anisotropy

First we look at the data for the lattice with no anisotropy and low temperature. The simulated spectrum in Figure 6.11a suggests that there are spin waves propagating. We can make out something that looks like an optical mode at $E = 2J$, and very high intensity at low energy at $\mathbf{q} = (1, 0)$ while almost zero intensity at $\mathbf{q} = (0, 0)$. Simulations of the antiferromagnetic kagomé lattice have been previously been performed by Robert et al [36]. They combined Monte Carlo and spin dynamics simulations to investigate 36 × 36 unit cells of a kagomé lattice in temperature with no anisotropy. They simulated temperature by generating different ground states for the spins and letting the simulation run deterministically by solving the spin equation of motion.

$$\frac{\mathrm{d}\mathbf{s}_i}{\mathrm{d}t} = J(\sum_j \mathbf{s}_j) \times \mathbf{s}_i \tag{6.7}$$

The spectrum shows some of the same features as the data from Robert et al. [36] seen in Figure 6.11b, like the very bright area at $\mathbf{q} = (1, 0)$ and the peak at q=(2/3,0) and q=(4/3,0) that looks like the soft mode. There are a few differences in the spectra, the most obvious of which is the $\mathbf{q}$-resolution. This is due to the comparative sizes of the simulated lattices, Figure 6.11b has been made from a lattice of 36 × 36 unit cells, a significantly bigger system than the one simulated in this thesis. This leads to the presumed acoustic mode not being visible on Figure 6.11a. We also see two excitations at high energies, one at $E \approx 2$ meV and one at $E \approx 2.5$ meV where the latter is not present in Robert's work. This might be due to the smaller size or higher temperature of the lattice.

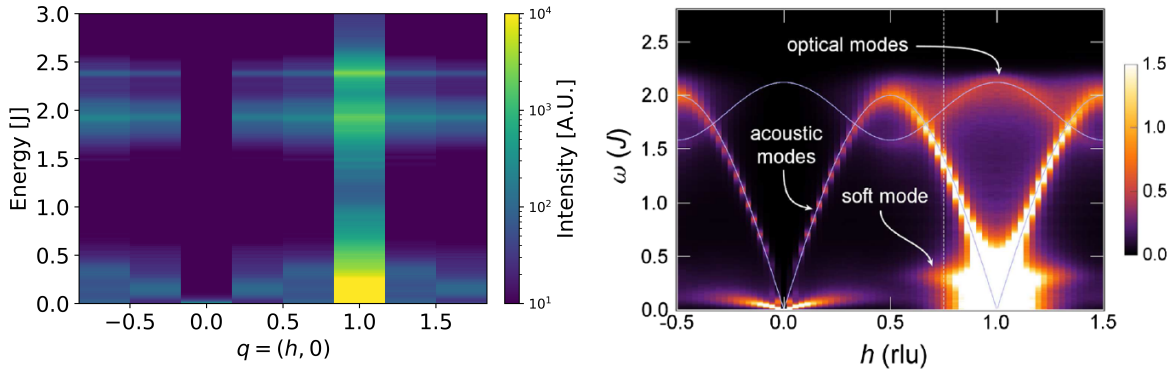

(a) Intensity map of the scattering function vs. E and $\mathbf{q} = (h, 0)$ for 3×3 unit cells of a kagomé lattice with $T/J = 5 \cdot 10^{-3}$, $J = 186$ mK and $D = 0$.

(b) Intensity map of the scattering function vs. E and $\mathbf{q} = (h, 0)$ for 36×36 unit cells of a kagomé lattice with $T/J = 5 \cdot 10^{-4}$. From Robert et al. [36].

Figure 6.11

6.4.2 Kagomé lattice with anisotropy in local z-axis

Looking at the data with anisotropy along the local z-axis we see a few differences from the corresponding simulations with the triangle. First and foremost the spin movement is no longer strictly confined parallel to the easy axis, but starts to move around the global xy-plane as the temperature increases. Figure 6.12a shows the spin movements at $T = 10$ mK, where the temperature is not yet large enough that the spins move round the circle, but they seem to have two modes. One where the spins are parallel to their local z-axis and one where they have a 30° angle with their local z-axis, as illustrated in Figure 6.12b.
Calculating the scattering cross section for these data we see several excitation peaks. Each peak was fitted with a Lorentzian function to find its position and width.

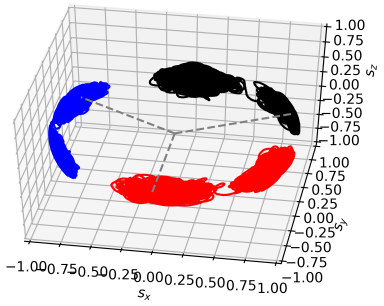

(a) Spin movement of three spins in kagomé unit cell with $J = 186$mK, $T = 10$mK, and $D = 80$mK. The colours of the spin movements corresponds to three spins in (b). Anisotropy easy axis shown as dashed line.

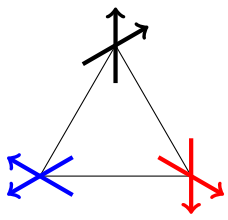

(b) The two possible spin directions in a kagomé unit cell are plotted.

Figure 6.12

For $\mathbf{q} = (0, 0)$ the intensity shows three peaks at $T = 100$ mK, one close to zero and two that could be separate modes. These are also represented for $\mathbf{q} = (1/3, 1/3)$ with different

amplitudes. These are shown with Lorentzian fits in Figure 6.13. The peak at $E = 0.08$ meV splits into two peaks at lower temperatures.

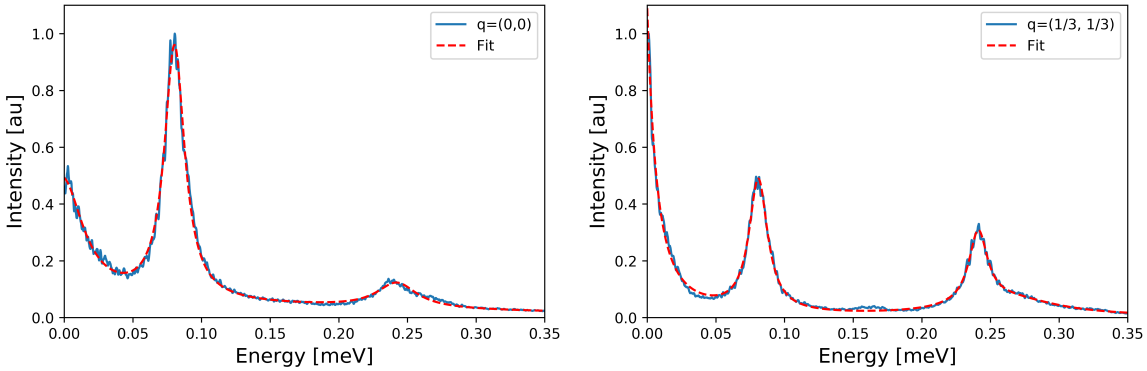

Figure 6.13: Cross section for the 3×3 kagomé unit cells with $J = 186$ mK, $T = 100$ mK and $D = 80$ mK anisotropy in along the local z-axis. The right panel has $\mathbf{q} = (0, 0)$ and the left panel has $\mathbf{q} = (1/3, 1/3)$.

The energy of these peaks are constant in temperature as seen in Figure 6.14a. At high temperature $T/J \approx 0.5$ the peaks become broad and difficult to distinguish from each other. This is a contrast to the simulations of the triangle, where the anisotropy was set to the same value $D = 80$ mK and there is a clear decrease in excitation energy with temperature. Looking at the scattering cross section as a function of $\mathbf{q}$, as seen in Figure 6.14b we see the peak widths and intensities do seem to be dependent on $\mathbf{q}$ while the energy seems largely independent of $\mathbf{q}$. It is difficult to make out the dispersion, with the resolution of the plot.

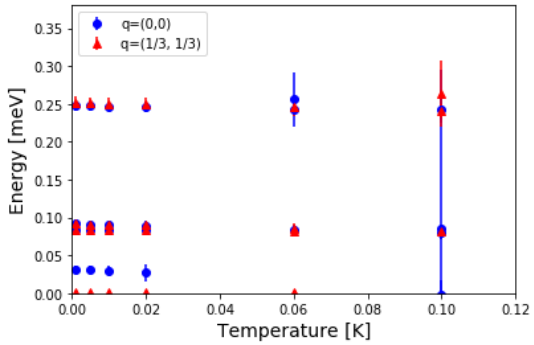

(a) Energy of excitation peaks as a function of temperature for two different $\mathbf{q}$-values for a kagomé lattice with $J = 186$ mK and $D = 80$ mK.

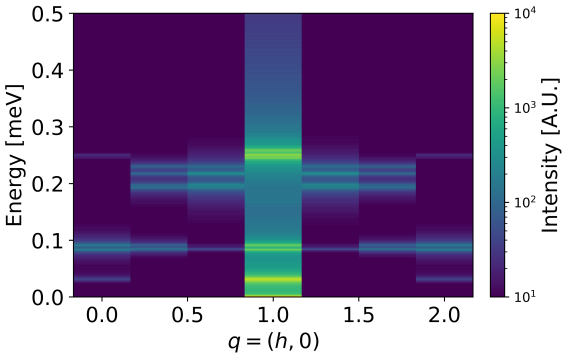

(b) Intensity map of the scattering function vs. E and $\mathbf{q} = (h, 0)$ for $T = 1$ mK for 3x3 unit cells of a kagomé lattice with $J = 186$ mK and $D = 80$ mK.

Figure 6.14

6.4.3 Kagomé lattice with anisotropy in local *xy*-plane

When the anisotropy is in the local xy-plane, the spins confine themselves to moving in an ellipse along the global z-axis, as seen in Figure 6.15. This is the same spin movement that we saw for the triangle with easy plane anisotropy in the local xy-plane. The spin directions as seen in the global xy-plane are illustrated in Figure 6.15b.

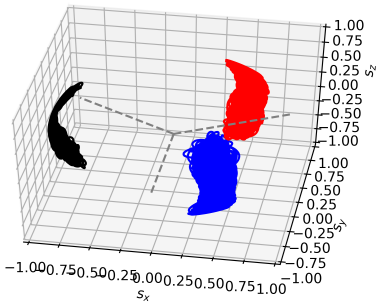

(a) Spin movement of three spins in kagomé unit cell with $J = 186$ mK, $T = 10$ mK, and $D = -80$ mK. The colours of the spin movements corresponds to three spins in (b). Local z-axis shown as grey dashed line.

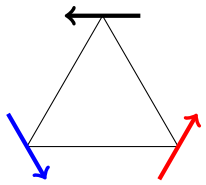

(b) The spin directions in a kagomé unit cell with $J = 186$ mK, $T = 10$ mK, and $D = -80$ mK.

Figure 6.15

For $\mathbf{q} = (0, 0)$ the intensity shows two peaks at $T = 100$ mK, one narrow and well-defined at lower energy and one that is broader at higher energy. There are also two peaks at $\mathbf{q} = (1/3, 1/3)$, they are both much broader and higher energy than the $\mathbf{q} = (0, 0)$ peaks. These spectra are shown with Lorentzian fits in Figure 6.16.

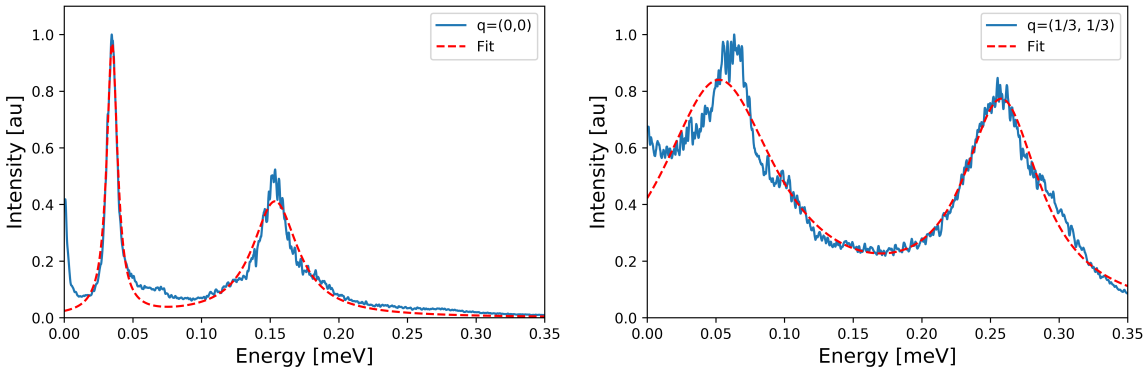

Figure 6.16: Cross section for the 3×3 kagomé unit cells with $J = 186$ mK, $T = 100$ mK and $D = -80$ mK anisotropy in the local xy-plane. The right panel has $\mathbf{q} = (0, 0)$ and the left panel has $\mathbf{q} = (1/3, 1/3)$.

The temperature dependence of the energies excitation look like they follow a $\sqrt{T}$ dependence. The highest excitation decreases in temperature and the lowest excitation increases. This happens for all $\mathbf{q}$-vectors. The temperature dependence of the excitation energies looks similar to the temperature dependence seen in Figure 6.9b for the triangle, at least for lower temperatures. Figure 6.17b shows that the excitations are $\mathbf{q}$-dependent, as with the easy axis anisotropy. The figure shows two excitation bands that broaden and increase in energy towards $\mathbf{q} = (1, 0)$ and tapers off towards $\mathbf{q} = (0, 0)$.

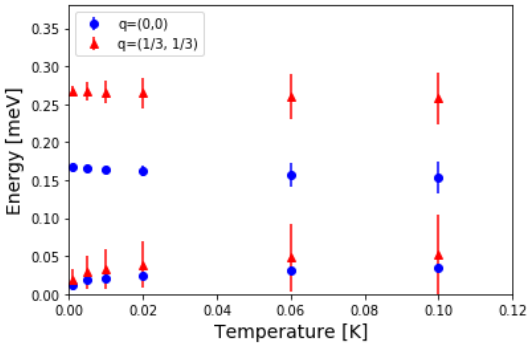

(a) Energy of excitation peaks as a function of temperature for two different **q**-values for 3x3 unit cells of a kagomé lattice with $J = 186$ mK and $D = -80$ mK.

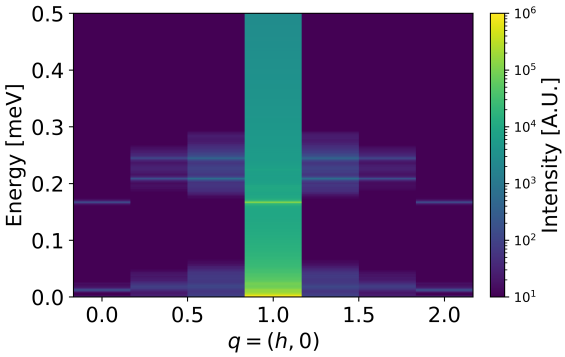

(b) Intensity map of the scattering function vs. E and $\mathbf{q} = (h, 0)$ for $T = 1$ mK, for 3×3 unit cells of a kagomé lattice with $J = 186$ mK and $D = -80$ mK.

Figure 6.17

6.4.4 Kagomé lattice with anisotropy in global z-axis

With the anisotropy easy axis being along the global z-axis, the anisotropy contributed to the frustration. The spins aligned themselves so one spin was parallel and two were mostly antiparallel with this axis, as seen by Figure 6.18a. The figure suggests that the spins still keep 120° between each other.

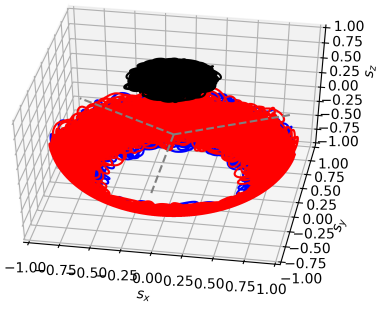

(a) Spin movement of three spins in kagomé unit cell with $J = 186$ mK, $T = 10$ mK, and $D = 80$ mK in the global z-direction. The colours of the spin movements corresponds to three spins in (b).

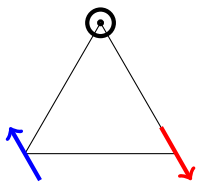

(b) The spin directions in a kagomé unit cell with $J = 186$ mK, $T = 10$ mK, and $D = 80$ mK.

Figure 6.18

The energy of the spins as a function of temperature for two **q**-values is shown in Figure 6.19a. The energies look constant as a function of temperature, like for the simulation with anisotropy easy axis along the local z-axis. This is likely for the same reason as with the anisotropy in the local z-axis, namely that the total added value of the anisotropy is the largest effect in the system and therefore dictates the dynamics of the spins.
When looking at the intensity as a function of energy and **q** in Figure 6.19b we can see that the excitations are **q**-dependent. There are two narrow bands at $\mathbf{q} = (0, 0)$ which are exchanged by several narrow bands at $\mathbf{q} = (n/3, 0)$ where n=1, 2, 3, 4, and 5.

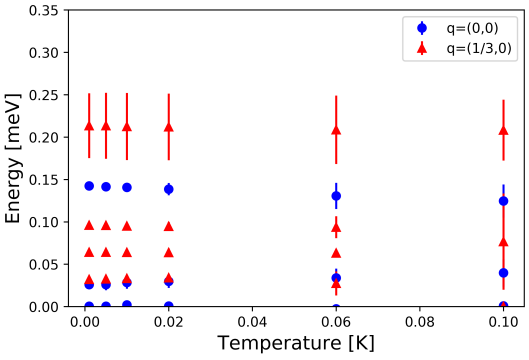

(a) Energy of excitation peaks as a function of temperature for two different **q**-values, for 3x3 unit cells of a kagomé lattice with $J = 186$ mK and $D = 80$ mK.

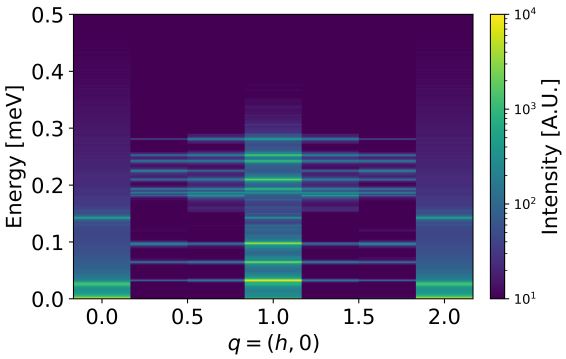

(b) Intensity map of the scattering function vs. E and $\mathbf{q} = (h, 0)$ for $T = 1$ mK, for 3×3 unit cells of a kagomé lattice with $J = 186$ mK and $D = 80$ mK.

Figure 6.19

6.4.5 Kagomé lattice with anisotropy in global *xy*-plane

When there is an easy plane anisotropy in the global xy-plane, the spins move freely in this plane, still with 120° between each other, as shown in Figure 6.20a.

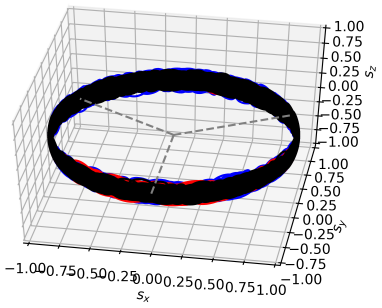

(a) Spin movement of three spins in kagomé unit cell with $J = 186$ mK, $T = 10$ mK, and $D = -80$ mK in the global xy-plane. The colours of the spin movements corresponds to three spins in (b).

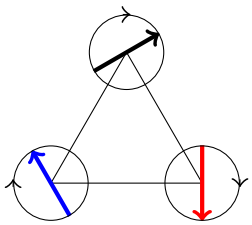

(b) The spin directions in a kagomé unit cell with $J = 186$ mK, $T = 10$ mK, and $D = 80$ mK.

Figure 6.20

Figure 6.21a shows that the energy of the spins is constant as a function of temperature. The excitations are **q**-dependent, with the energy increasing towards $\mathbf{q} = (1, 0)$. This is seen in Figure 6.21b.

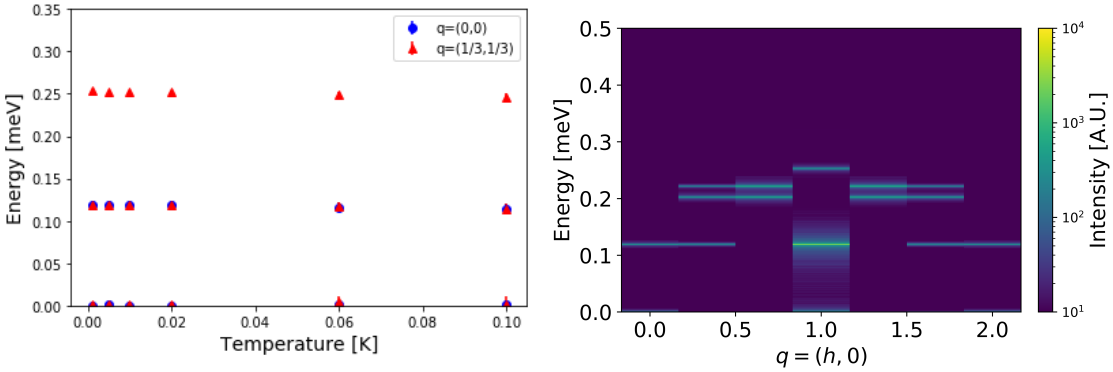

(a) Energy of excitation peaks as a function of temperature for two different **q**-values for 3x3 unit cells of a kagomé lattice with $J = 186$ mK and $D = -80$ mK.

(b) Intensity map of the scattering function vs. E and $\mathbf{q} = (h, 0)$ for $T = 1$ mK for 3×3 unit cells of a kagomé lattice with $J = 186$ mK and $D = -80$ mK.

Figure 6.21

6.5 Discussion

6.5.1 Triangle

We simulated four different triangle systems with antiferromagnetic exchange interactions. The first was the triangle with no temperature and anisotropy in the local z-axis. This system behaved as theoretically predicted for no anisotropy, where the spins were in a zero mode with the energy depending on the canting angle, described by Eq. 5.5.
When anisotropy was added the energy of the system changed for low canting angles to look more like the energy of a single spin with easy axis anisotropy.
A triangle with no anisotropy in low temperature showed two different excitations, visible at $\mathbf{q} = (1/3, 1/3)$. One low energy excitation with energy constant in temperature, and one broad excitation with energy increasing with temperature. The width of the broad peak suggests that the peak describes several excitations.
The shape of this spectrum is very similar to that of the excitation spectrum of GAG measured with neutron scattering [4]. The key differences are that the observed high energy excitation INS3 shown in the inset of Figure 6.22a does not show up in the triangle simulations, and the energy scales are very different. The difference in energy is primarily caused by the lack of anisotropy in the simulations.

A triangle with anisotropy in the local z-axis was simulated for several temperatures, several anisotropy values, and several exchange values. Looking at the intensity spectra for $\mathbf{q} = (0, 0)$ and $\mathbf{q} = (1/3, 1/3)$ we see two excitation peaks and one structural peak at $E = 0$ for $\mathbf{q} = (1/3, 1/3)$. For lower temperatures the two peaks are well-defined and at higher temperatures they become broad and more noisy, and a broad, badly defined peak appears at lower energy. The two excitation peaks are closer in energy to INS1 and INS2 in GAG, but the shape of the peaks do not look very similar. INS3 is also not replicated in the triangle spectrum. The dissimilarities between the two cases is not too surprising given that the anisotropy simulated in this case is along the local z-axis and the anisotropy found for GAG is in the local xy-plane [4].
The energies of the excitations increased with increasing anisotropy, and with increasing exchange interaction. This is as expected. The excitation energies decreased with increasing

temperature, and the peak widths increased with temperature. This is the opposite relation in the triangle without anisotropy, but since the energies of the two excitations are $E \sim 10^{-3}$ meV for the triangle with no anisotropy and $E \sim 10^{-1}$ meV for the triangle with anisotropy, we conclude that the two represent different excitations. These different behaviours show how the system reacts differently to increasing temperature with and without anisotropy. In the simulation with anisotropy increased temperature get the spins further away from the energy minimum which makes the energy decrease. When there is no anisotropy the exchange interaction dominates which means the energy increases with canting angle. We cannot compare with the temperature dependence of the excitation peaks in GAG because it is not known.

A triangle with anisotropy in the local xy-plane was also simulated for several temperatures and several anisotropy values. The spin movement shows the spins lying perpendicular to their local z-axes and moving along the global z-axis. The excitation spectrum shows two and three excitation peaks for $\mathbf{q} = (0, 0)$ and $\mathbf{q} = (1/3, 1/3)$ respectively when varying the anisotropy, as well as the structural peak seen at $\mathbf{q} = (1/3, 1/3)$. The energies of the excitation peaks increased with the size of the anisotropy, like it did for the triangle with anisotropy in the local z-axis. The higher energy peak decreases in energy with increasing temperature, while the lower energy peak increases in energy. Both seem to approach a constant at the highest temperatures. This behaviour could be due to a mix of a zero mode which increases in energy with temperature and an anisotropy mode that decreases in energy when the spins are not in the anisotropy plane.
The simulated intensity spectra do not resemble the shape of the excitation spectrum for GAG. The excitations in the triangle have energy $E = 0.02$ meV and $E = 0.11$ meV, which is lower than INS1 and INS2, and they are significantly more well defined. The energy difference is small, which makes it likely to be due to the spins in the triangle having only two neighbours and not four like in a hyperkagomé lattice. The sharpness of the peaks is affected by many things, among which are the lower temperatures in the simulation compared to the experiments. Another parameter that affects the peak widths of the simulated spectrum is the damping factor λ. If we increase λ we also increase the width of the peak. Furthermore the peak widths of the neutron scattering data are affected by potential imperfections in the GAG powder measured and instrument resolution, neither of which we have included in the simulations.
As before INS3 is not reproduced by these simulations. It is expected for there to be differences in excitation spectra, as it would be highly unlikely for us to be able to reproduce the excitations of a hyperkagomé lattice by simulating just a single triangle. We did not have the time to simulate 3×3 unit cells of a triangular lattice.

6.5.2 Kagomé

A kagomé lattice of 3×3 unit cells with antiferromagnetic exchange interactions was simulated for a variety of different anisotropy configurations. The simplest system was a lattice with zero temperature, no anisotropy and some spins canted away from equilibrium. The energy of the system showed perfect agreement with theory.
The kagomé lattice with temperature and no anisotropy showed sign of spin waves, with an optical mode visible in the spectrum at $E = 2J$. The spectrum also shares many similarities with the spectrum from a simulated kagomé lattice of 36×36 unit cells by Robert et al. [36]. Amongst these are a very bright peak at low energy for $\mathbf{q} = (1, 0)$, very low intensity at

$\mathbf{q} = (0, 0)$, and signs of a soft mode at $\mathbf{q} = (2/3, 0)$ and $\mathbf{q} = (4/3, 0)$. The main difference between the two figures is the low $\mathbf{q}$-resolution of our figure, which is due to the small size of the system.

The kagomé lattice with anisotropy along the local z-axis shows the spins lying along the local z-axis for low temperatures and moving around the global xy-plane for high temperatures. There is one step between the two at $T = 10$ mK where the spins have two states, one along the local z-axis and one at 30° to it. We expect the spins to behave like the triangle with anisotropy in the local z-axis, where the spins stay in the z-direction, and moved uniformly away from it with increasing temperature. This behaviour in the kagomé lattice is unexpected, and it is unknown if it is correct or an artefact of the way the anisotropy is implemented in the code, but unfortunately there was not enough time to investigate the cause of this effect.
Looking at the excitation spectra we see between two and three excitations depending on the $\mathbf{q}$-value. These are close to the energies of INS1 and INS2 in GAG, and resemble the shape in that the lower energy peak is more well-defined than the higher energy peak. There is no equivalent to the INS3 peak in the simulated intensities. The two excitation peaks for the kagomé simulations do not overlap like the GAG excitations do. We do not expect the excitation spectra to be identical, since the anisotropy is along the local z axis instead of the local xy plane, and the lattices are different in the two cases, but it is interesting that excitations happen at about the same energies. The spectrum is also closer to the GAG spectrum than for the triangle with local z anisotropy, which shows that the lattice does have a big effect on the spin dynamics, and that a kagomé lattice is one step closer to GAG than a single triangle.
The excitation energies are constant in temperature in contrast to the simulated triangle with anisotropy along local z. This might be due to the fact that the anisotropy is affected by the number of spins in the lattice, which would make the actual anisotropy strength $N_{spin}D = 27D = 2.2$ K for the kagomé lattice. This is significantly more than the exchange interaction of $J = 186$ mK, which means that the anisotropy dominates the system and forces the spins to keep constant overall direction.

In the simulated kagomé lattice with anisotropy in the local xy-plane, the spins lie perpendicular to the local z-axis and move along the global z-axis. This is in agreement with the results for the triangle with anisotropy in the local xy-plane. Two excitation peaks were seen in the excitation spectra for $\mathbf{q} = (0, 0)$ and $\mathbf{q} = (1/3, 1/3)$. As with the triangle simulation the higher energy peak decreases in energy with increasing temperature, while the lower energy peak increases in energy. This also looks like the triangle with corresponding anisotropy. The energies are also $\mathbf{q}$-dependent, the two excitations increase in energy and broaden towards $\mathbf{q} = (1, 0)$. The intensity spectra for $T = 100$ mK are the closest to GAG of all the simulations with anisotropy, as seen in Figure 6.22. At $\mathbf{q} = (0, 0)$ there is a narrow peak at $E = 0.03$ meV and a broader peak at $E = 0.15$ meV. These are close to the energies of INS1 and INS2 as shown in Figure 6.22a. The main difference between the two spectra is that the high energy peak for the kagomé lattice is more well-defined and the two peaks are not merged. This could be due to a variety of factors, like the difference in lattice structure or anisotropy value between the systems. Since the anisotropy value for GAG is not known it is difficult to predict its effect on the spin dynamics. Jacobsen also observed that simulated excitation peaks were sharper compared to measured data [10], so the effect is expected.

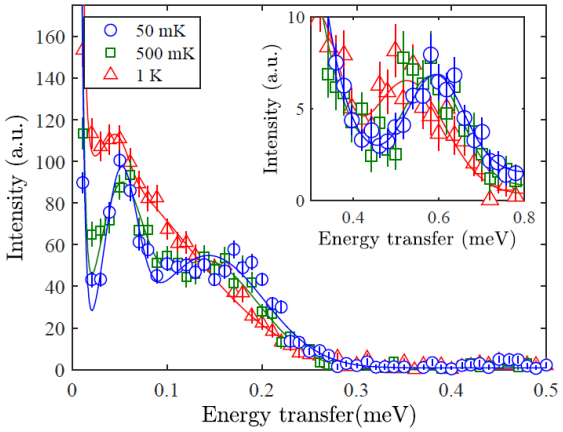

(a) Temperature and energy dependence of excitations of GAG found from inelastic neutron scattering on a powder of GAG. Inset shows **q**-integrated intensity of the higher energy excitation. Figure from Jacobsen et al. [4].

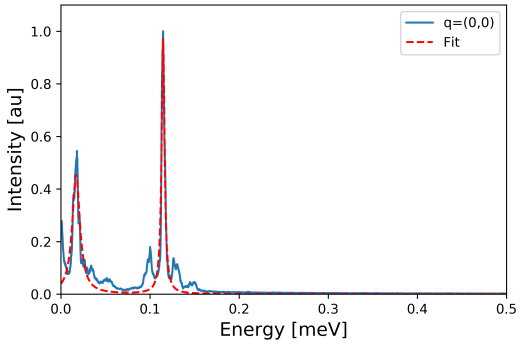

(b) ntensity of triangle with antiferromagnetic exchange $J = 186$ mK, temperature $T = 20$ mK and anisotropy $D = -80$ mK in the local xy-plane. Red dashed line shows fit with two Lorentzian functions.

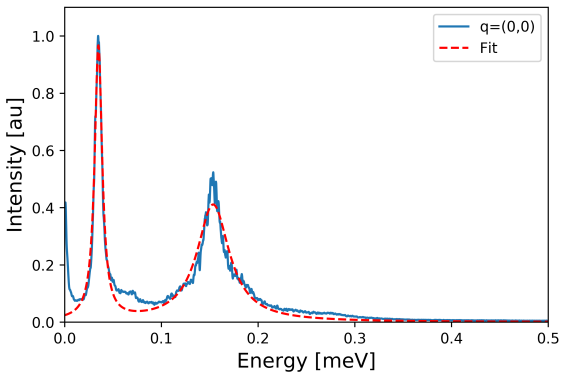

(c) Intensity of 3×3 unit cells of a kagomé with antiferromagnetic exchange $J = 186$ mK, temperature $T = 100$ mK and anisotropy $D = -80$ mK in the local xy-plane. Red dashed line shows fit with two Lorentzian functions.

Figure 6.22

In the simulated kagomé lattice with anisotropy in the global z-axis, the anisotropy contributes to the frustration in the lattice. There is one spin in each unit cell pointing up along the global z-axis and two spins that point mostly antiparallel to this axis, all with 120° to each other. It looks like the upward pointing spin is close to stationary while the two downward pointing spins rotate freely in the global xy-plane. This indicates the presence of a zero mode. This is supported by the three excitations at $E = 0.03$ meV, $E = 0.06$ meV and $E = 0.1$ meV, that are constant in $\mathbf{q}$ and very well defined.

For the kagomé lattice with anisotropy in the global xy-plane, the spins move freely in the plane while still keeping 120° angle to each other. The excitation energies are constant in temperature and seem to vary in $\mathbf{q}$, the energy of the peaks increase towards $\mathbf{q} = (1, 0)$ with the peaks splitting in two at $\mathbf{q} = (1/3, 0)$, $(2/3, 0)$, $(4/3, 0)$, and $(5/3, 0)$.

Chapter 7

Conclusion and Outlook

In this chapter we will summarise the results of this thesis and provide an outlook for possible future work.

7.1 Conclusions

In this thesis we have worked with and improved the simulation suite CLaSSiC. The single-ion anisotropy interaction was added to CLaSSiC, and extensive validations performed. The physical parameters, exchange interaction J, single-ion anisotropy D, external magnetic field B and temperature T, were validated both for integration in spherical and Cartesian coordinates. Several errors were found when validating the simulation in spherical coordinates, namely instabilities and the simulations in temperature being consistently off compared to theory. Smaller errors in the simulation program were also found and corrected during the project.
In contrast, integration in Cartesian coordinates have results that agree with analytical calculations. The implementation of the Zeeman interaction, temperature, nearest neighbour exchange interaction and the single-ion anisotropy interaction were validated independently for one and two spins, and in combination for two spins and a spin chain. We can conclude that we can accurately simulate the dynamics of any system of spins, including exchange interactions, local and global anisotropies, applied magnetic fields and temperature effects.

We simulated three spins in a triangle with antiferromagnetic exchange interactions, and with and without anisotropy, in an effort to build our understand of spin dynamics in frustrated systems, and how they are affected by temperature and anisotropy strength. The results were compared with excitation spectra for GAG to see if a three spin system could replicate some of the dynamics in GAG.
Three different three spin systems were simulated, one with no anisotropy, one with anisotropy along the local z-axis and one with anisotropy in the local xy-plane. The first triangle showed two excitation peaks, one of them increasing in energy as a function of temperature. This is a concrete example of the zero mode excitation at a finite temperature.
For the triangles with anisotropy, the excitation energies were shown to increase with the anisotropy strength for both cases, as we expect. For the triangle with anisotropy along the local z-axis we further showed that the excitation energies increased with exchange strength and that the energies decreased in energy as the temperature increased. The triangle with anisotropy in the local xy-plane showed two different behaviours for the two excitation peaks as a function of temperature. The higher energy peak decreased in energy, while the lower

energy peak increase its energy as a function of increasing temperature. This could be due to a mix of a zero mode which increases in energy with temperature and an anisotropy mode that decreases in energy when the spins are not in the anisotropy plane.

To understand how the spin dynamics are affected by being in a lattice structure, we simulated a kagomé lattice consisting of 9 corner sharing triangles or 3×3 unit cells with various anisotropy directions. For the simulation with no anisotropy, the dispersion was compared with a dispersion found by similar simulations by Robert et al. [36]. The two shared several features, but it was difficult to follow the details of the dispersions, given our poor resolution in $\mathbf{q}$. The kagomé lattice with anisotropy in the local z-axis shows an unexpected spin movement with a mode along the local z-direction and a mode with 30° to the local z-axis. It is unclear whether this is an artefact of the implementation of the anisotropy or not. The energy of the excitations are constant in temperature, likely due to the anisotropy.
The kagomé lattice with anisotropy in the global z-axis had different amount of excitations depending on the $\mathbf{q}$-value, but they all had a constant energy as a function of temperature. There were three well-defined excitations around $E \sim 0.5$ meV, that are constant in $\mathbf{q}$. This is the sign of local modes in the lattice.
The kagomé lattice with anisotropy in the global xy-plane, showed the spins rotating freely in the plane while keeping 120° to each other. The excitation energies were also constant as a function of temperature.

Comparing the shape of the excitation spectrum of the triangle with anisotropy in the local xy-plane with the energy spectrum of GAG shows some similarities. Both systems have two large excitation peaks with energies around 0.1 meV. GAG also has an excitation at $E \sim 0.5$ meV which does not show up in the simulations of the triangles. The triangle has lower energy peaks, likely due to the spins in a triangle having half the amount of nearest neighbours compared to in a hyperkagomé lattice.
The kagomé lattice with anisotropy in the local xy-axis has two excitation peaks at almost the same energies as the two lower energy excitations for GAG. This shows that some of the excitation spectrum of GAG can be described with a simpler system like a small kagomé lattice.
It was difficult to compare the dispersions of GAG and the kagomé simulations, because the $\mathbf{q}$-resolution for the kagomé dispersion is very low due to the small size of the simulated lattice.

7.2 Outlook

We can split the outlook into two categories, the first one is improvements suggested for the simulation suite itself and the second is the things we would like to simulate with the program. Currently big simulations take a lot of time to run, it would be nice to speed this up. The simulations of the 3×3 kagomé unit cells of $N = 5 \cdot 10^6$ datapoints took eight hours to run on a computer with a clock frequency of 3.40 GHz. Speeding this up can be done by optimising the central loop of the code, for example by using a faster integration method than Adams-Bashfort or writing it in a faster code language like C [37]. Python is slower because it is an interpreted language, where each code line is read and translated into machine executable commands, e.g. for each step in the loop, where C compiles the code into machine executables once and for all [38]. To further speed up the code and lessen the amount of storage needed for simulated data, one could look into only saving e.g. every third or every

fourth data point. This would save the time it takes to save the individual data points, and make it faster to calculate the scattering functions for simulations.
It would be interesting to implement a dipole interaction to the simulations in order to better describe systems like GAG and GGG which both have dipole interactions of the same order of magnitude as the exchange and anisotropy interactions.
We simulated a kagomé lattice with 3×3 unit cells with different anisotropy directions. To build on this, one could further explore the parameter space, for example by varying the anisotropy size or simulating higher temperatures. Varying the anisotropy could have the goal of achieving the same distribution of spin orientations as in GAG, to see how that would affect the energy spectrum. It is also relevant to investigate the strange mode seen in the kagomé simulations with anisotropy in the local z-axis, where the spins lay with a 30° angle to local z. With a faster simulation program it would be possible to simulate more kagomé unit cells for example 36×36, and get a much better $\mathbf{q}$-resolution to be able to analyse the energy dispersion of the simulations. This would be interesting to compare to neutron scattering data on jarosite, like the data from Matan et al. [19]. It is also interesting to simulate a triangular lattice with high definition in order to compare to neutron data on this system, like the paper from Janas et. al [39].
With a faster runtime it would also be possible to simulate a 3D lattice like the hyperkagomé lattice. With a unit cell of 24 spins it should be possible to simulate $2 \times 2 \times 2$ unit cells or even $4 \times 4 \times 4$ unit cells. This could be done to further investigate GAG and see if the third excitation in the GAG power spectrum could be reproduced in the simulations. It would also be interesting to look at similar systems like $Yb_3Ga_5O_{12}$ which we are interested in in the group, see Sandberg et al. [40]. There are several interesting 3D systems to potentially simulate, for example titanates like $Ho_2Ti_2O_7$ and $Dy_2Ti_2O_7$ [41]. It would also be interesting to do these simulations in absolute units so the intensities of the scattering function could be directly compared with data.

Bibliography

[1] L. Balents, "Spin liquids in frustrated magnets," *Nature*, vol. 464, pp. 199–208, Mar. 2010.

[2] G. H. Wannier, "Antiferromagnetism. the triangular ising net," *Phys. Rev.*, vol. 79, pp. 357–364, 2 Jul. 1950.

[3] T. Fennell, P. P. Deen, A. R. Wildes, K. Schmalzl, D. Prabhakaran, A. T. Boothroyd, R. J. Aldus, D. F. McMorrow, and S. T. Bramwell, "Magnetic coulomb phase in the spin ice $Ho_2Ti_2O_7$," *Science*, vol. 326, no. 5951, pp. 415–417, 2009, ISSN: 0036-8075.

[4] H. Jacobsen, O. Florea, E. Lhotel, K. Lefmann, O. Petrenko, C. S. Knee, T. Seydel, P. F. Henry, R. Bewley, D. Voneshen, A. Wildes, G. Nilsen, and P. P. Deen, *Spin dynamics of the director state in frustrated hyperkagome systems*, 2021.

[5] S. T. Bramwell and B. Keimer, "Neutron scattering from quantum condensed matter," *Nature Materials*, vol. 13, pp. 763–767, Aug. 2014.

[6] G. L. Squires, *Introduction to the Theory of Thermal Neutron Scattering*, 3rd ed. Cambridge University Press, 2012.

[7] K. Lefmann, *Neutron Scattering: Theory, Instrumentation, and Simulation*. Niels Bohr Institute, Copenhagen, 2019.

[8] S. Blundell, *Magnetism in Condensed Matter*. Oxford University Press, 2001.

[9] P. W. Anderson, "An approximate quantum theory of the antiferromagnetic ground state," *Phys. Rev.*, vol. 86, pp. 694–701, 5 Jun. 1952.

[10] H. S. Jacobsen, "Magnetic properties of nano-scale hematite: Theory, experiments, and simulations," M.S. thesis, University of Copenhagen, 2014.

[11] K. Yosida, *Theory of Magnetism*. Springer, 1998.

[12] E. Y. Lenander, "Spin dynamics outside the scope of spin wave theory," Bachelor's thesis, University of Copenhagen, 2020.

[13] J. T. Chalker, "Geometrically frustrated antiferromagnets: Statistical mechanics and dynamics," in *Introduction to Frustrated Magnetism*, C. Lacroix, P. Mendels, and F. Mila, Eds., Springer, 2011, pp. 3–22.

[14] K. Lefmann, H. Jacobsen, J. Garde, P. Hedegård, A. Wischnewski, S. N. Ancona, H. S. Jacobsen, C. R. H. Bahl, and L. T. Kuhn, "Dynamic rotor mode in antiferromagnetic nanoparticles," *Phys. Rev. B*, vol. 91, p. 094 421, 9 Mar. 2015.

[15] T. Yildirim and A. B. Harris, "Magnetic structure and spin waves in the kagomé jarosite compound $KFe_3(SO_4)_2(OH)_6$," *Phys. Rev. B*, vol. 73, p. 214 446, 21 Jun. 2006.

[16] P. Mendels and A. S. Wills, "Kagomé antiferromagnets: Materials vs. spin liquid behaviors," in *Introduction to Frustrated Magnetism*, C. Lacroix, P. Mendels, and F. Mila, Eds., Springer, 2011, pp. 207–236.

[17] S. Janas, "Neutron spectroscopy studies of geometrically frustrated antiferromagnets," Ph.D. dissertation, PhD School of the Faculty of Science, University of Copenhagen, 2020.

[18] F. C. Coomer, A. Harrison, G. S. Oakley, J. Kulda, J. R. Stewart, S. J. A., B. Fåk, J. W. Taylor, and D. Visser, "Spin waves in the frustrated kagomé lattice antiferromagnet $KFe_3(OH)_6(SO_4)_2$," *Journal of Physics: Condensed Matter*, vol. 18, p. 8847, 39 Sep. 2006.

[19] K. Matan, D. Grohol, D. G. Nocera, T. Yildirim, A. B. Harris, S. H. Lee, S. E. Nagler, and Y. S. Lee, "Spin waves in the frustrated kagomé lattice antiferromagnet $KFe_3(OH)_6(SO_4)_2$," *Phys. Rev. Lett.*, vol. 96, p. 247 201, 24 Jun. 2006.

[20] J. A. M. Paddison, H. Jacobsen, O. A. Petrenko, M. T. Fernández-Díaz, P. P. Deen, and A. L. Goodwin, "Hidden order in spin-liquid $Gd_3Ga_5O_{12}$," *Science*, vol. 350, no. 6257, pp. 179–181, 2015, ISSN: 0036-8075.

[21] O. A. Petrenko, C. Ritter, M. Yethiraj, and D. McK Paul, "Investigation of the low-temperature spin-liquid behavior of the frustrated magnet gadolinium gallium garnet," *Phys. Rev. Lett.*, vol. 80, pp. 4570–4573, 20 May 1998.

[22] O. Florea, E. Lhotel, H. Jacobsen, C. S. Knee, and P. P. Deen, "Absence of magnetic ordering and field-induced phase diagram in the gadolinium aluminum garnet," *Phys. Rev. B*, vol. 96, p. 220 413, 22 Dec. 2017.

[23] P. P. Deen, O. A. Petrenko, G. Balakrishnan, B. D. Rainford, C. Ritter, L. Capogna, H. Mutka, and T. Fennell, "Spin dynamics in the hyperkagome compound $Gd_3Ga_5O_{12}$," *Phys. Rev. B*, vol. 82, p. 174 408, 17 Nov. 2010.

[24] N. d'Ambrumenil, O. A. Petrenko, H. Mutka, and P. P. Deen, "Dispersionless spin waves and underlying field-induced magnetic order in gadolinium gallium garnet," *Phys. Rev. Lett.*, vol. 114, p. 227 203, 22 Jun. 2015.

[25] P. Bonville, J. A. Hodges, J. P. Sanchez, and P. Vulliet, "Planar spin fluctuations with a quadratic thermal dependence rate in spin liquid $Gd_3Ga_5O_{12}$," *Phys. Rev. Lett.*, vol. 92, p. 167 202, 16 Apr. 2004.

[26] S. R. Dunsiger, J. S. Gardner, J. A. Chakhalian, A. L. Cornelius, M. Jaime, R. F. Kiefl, R. Movshovich, W. A. MacFarlane, R. I. Miller, J. E. Sonier, and B. D. Gaulin, "Low temperature spin dynamics of the geometrically frustrated antiferromagnetic garnet $Gd_3Ga_5O_{12}$," *Phys. Rev. Lett.*, vol. 85, pp. 3504–3507, 16 Oct. 2000.

[27] P. Schiffer, A. P. Ramirez, D. A. Huse, and A. J. Valentino, "Investigation of the field induced antiferromagnetic phase transition in the frustrated magnet: Gadolinium gallium garnet," *Phys. Rev. Lett.*, vol. 73, pp. 2500–2503, 18 Oct. 1994.

[28] P. P. Deen, O. Florea, E. Lhotel, and H. Jacobsen, "Updating the phase diagram of the archetypal frustrated magnet $Gd_3Ga_5O_{12}$," *Phys. Rev. B*, vol. 91, p. 014 419, 1 Jan. 2015.

[29] https://github.com/hyatt03/LaSSi, Accessed: 20-03-2020, 2020.

[30] J. Garde, "Numerical simulations of magnetic dynamics in nanoparticles," M.S. thesis, University of Copenhagen, 2008.

[31] R. T. Christensen, "Simulations of classical spin dynamics," Bachelor's thesis, University of Copenhagen, 2017.

[32] J. P. Hyatt, "General purpose simulations of classical spin dynamics," Bachelor's thesis, University of Copenhagen, 2019.

[33] L. D. Landau and E. M. Lifshitz, *Statistical Physics, vol. 5 of Course of Theoretical Physics*, 3rd ed. Butterworth-Heinemann, 1980.

[34] J. C. Butcher, *Numerical Methods for Ordinary Differential Equations*. Wiley, 2016.

[35] C. R. H. Bahl, J. Garde, K. Lefmann, T. B. Jensen, P.-A. Lindgård, D. E. Madsen, and S. Mørup, "Uniform spin wave modes in antiferromagnetic nanoparticles with uncompensated moments," *The European Physical Journal B*, vol. 62, pp. 53–57, 2008.

[36] J. Robert, B. Canals, V. Simonet, and R. Ballou, "Propagation and ghosts in the classical kagome antiferromagnet," *Phys. Rev. Lett.*, vol. 101, p. 117 207, 11 Sep. 2008.

[37] *Extending python with c or c++*, https://docs.python.org/3/extending/extending.html, Accessed: 25-05-2021.

[38] T. Lambert, *Computer programming languages: Why c runs so much faster than python*, https://www.huffpost.com/entry/computer-programming-languages-why-c-runs-so-much_b_59af8178e4b0c50640cd632e, Accessed: 31-05-2021, 2017.

[39] S. Janas, J. Lass, A.-E. Ţu ţueanu, M. L. Haubro, C. Niedermayer, U. Stuhr, G. Xu, D. Prabhakaran, P. P. Deen, S. Holm-Dahlin, and K. Lefmann, "Classical spin liquid or extended critical range in h-$YMnO_3$?" *Phys. Rev. Lett.*, vol. 126, p. 107 203, 10 Mar. 2021.

[40] L. Sandberg, R. Edberg, I. M. B. Bakke, K. Pedersen, Mônica, C. Hatnean, G. Balakrishnan, L. Mangin-Thro, A. Wildes, B. Fåk, G. Ehlers, G. Sala, P. Henelius, K. Lefmann, and P. Deen, "Emergent magnetic behaviour in the frustrated yb3ga5o12 garnet," 2020.

[41] B. D. Gaulin and J. S. Gardner, "Experimental studies of pyrochlore antiferromagnets," in *Introduction to Frustrated Magnetism*, C. Lacroix, P. Mendels, and F. Mila, Eds., Springer, 2011, pp. 177–206.

Appendix A

Equations of motion

The equations of motions are found from

$$-i\frac{\mathrm{d}}{\mathrm{d}t}\mathbf{s} = [H, \mathbf{s}] \tag{A.1}$$

where κ is the anisotropy matrix, $\mathbf{s}$ is the spin vector and we have set $\hbar = 1$.
The commutators of the spin operators are

$$[s_i^x, s_j^y] = is_i^z\delta_{ij}, \qquad [s_i^y, s_j^z] = is_i^x\delta_{ij}, \qquad [s_i^z, s_j^x] = is_i^y\delta_{ij} \tag{A.2}$$

Some useful commutator identities are

$$[A, BC] = [A, B]C + B[A, C] \tag{A.3}$$
$$[AB, C] = A[B, C] + [A, C]B \tag{A.4}$$

A.1 Anisotropy

The anisotropy part of the equation of motion is

$$-i\frac{\mathrm{d}}{\mathrm{d}t}\mathbf{s} = [\mathbf{s}^T\kappa\mathbf{s}, \mathbf{s}] \tag{A.5}$$
$$= \left[(s_x, s_y, s_z)\begin{pmatrix}\kappa_{11} & \kappa_{12} & \kappa_{13}\\ \kappa_{21} & \kappa_{22} & \kappa_{23}\\ \kappa_{31} & \kappa_{32} & \kappa_{33}\end{pmatrix}\begin{pmatrix}s_x\\ s_y\\ s_z\end{pmatrix}, \mathbf{s}\right] \tag{A.6}$$
$$= [s_x(\kappa_{11}s_x + \kappa_{12}s_y + \kappa_{13}s_z) + s_y(\kappa_{21}s_x + \kappa_{22}s_y + \kappa_{23}s_z) + s_z(\kappa_{31}s_x + \kappa_{32}s_y + \kappa_{33}s_z), \mathbf{s}] \tag{A.7}$$

The x-component is

$$-i\frac{\mathrm{d}}{\mathrm{d}t}s_x = -i\kappa_{12}s_xs_z + i\kappa_{13}s_xs_y - i\kappa_{21}s_zs_x - i\kappa_{22}(s_ys_z + s_zs_y) + i\kappa_{23}(s_y^2 - s_z^2) \tag{A.8}$$
$$+ i\kappa_{31}s_ys_x + i\kappa_{32}(s_y^2 - s_z^2) + i\kappa_{33}(s_zs_y + s_ys_z) \tag{A.9}$$

Rewriting this we get

$$\frac{\mathrm{d}}{\mathrm{d}t}s_x = s_z(\kappa_{21}s_x + \kappa_{22}s_y + \kappa_{23}s_z) - s_y(\kappa_{31}s_x + \kappa_{32}s_y + \kappa_{33}s_z) \tag{A.10}$$
$$+(\kappa_{12}s_x + \kappa_{22}s_y + \kappa_{32}s_z)s_z - (\kappa_{13}s_x + \kappa_{23}s_y + \kappa_{33}s_z)s_y \tag{A.11}$$

Similarly for the other two components we get

$$\frac{\mathrm{d}}{\mathrm{d}t}s_y = s_x(\kappa_{31}s_x + \kappa_{32}s_y + \kappa_{33}s_z) - s_z(\kappa_{11}s_x + \kappa_{12}s_y + \kappa_{13}s_z) \tag{A.12}$$

$$+(\kappa_{13}s_x + \kappa_{23}s_y\kappa_{33}s_z)s_x - (\kappa_{11}s_x + \kappa_{21}s_y + \kappa_{31}s_z)s_z \tag{A.13}$$

and

$$\frac{\mathrm{d}}{\mathrm{d}t}s_z = s_y(\kappa_{11}s_x + \kappa_{12}s_y + \kappa_{13}s_z) - s_x(\kappa_{21}s_x + \kappa_{22}s_y + \kappa_{23}s_z) \tag{A.14}$$

$$+(\kappa_{11}s_x + \kappa_{21}s_y + \kappa_{31}s_z)s_y - (\kappa_{12}s_x + \kappa_{22}s_y + \kappa_{32}s_z)s_x \tag{A.15}$$

Together this can be written as

$$\frac{\mathrm{d}}{\mathrm{d}t}\mathbf{s} = -\mathbf{s} \times (\kappa\mathbf{s}) + (\mathbf{s}^T\kappa) \times \mathbf{s} \tag{A.16}$$

When taking the classical limit we can rewrite to

$$\frac{\mathrm{d}}{\mathrm{d}t}\mathbf{s} = -2\mathbf{s} \times (\kappa\mathbf{s}). \tag{A.17}$$

Appendix B

Equation of motion in spherical coordinates

We start of with the equation of motion with temperature for the spins:

$$\frac{\mathrm{d}\mathbf{s}_i}{\mathrm{d}t} = \gamma \mathbf{s}_i \times (\tilde{\mathbf{B}} + \mathbf{b}) - \gamma\lambda \mathbf{s}_i \times (\mathbf{s}_i \times \tilde{\mathbf{B}}) \tag{B.1}$$

To convert to spherical coordinates we define the spin, the magnetic field and the random field as follows

$$\mathbf{s}_i = (\sin(\theta_i)\cos(\phi_i), \sin(\theta_i)\sin(\phi_i), \cos(\theta_i))^\dagger \tag{B.2}$$

$$\tilde{\mathbf{B}} = (B_x, B_y, B_z)^\dagger \tag{B.3}$$

$$\mathbf{b} = b \cdot (\sin(\theta_b)\cos(\phi_b), \sin(\theta_b)\sin(\phi_b), \cos(\theta_b))^\dagger \tag{B.4}$$

Inserting these into Eq. B.1 and taking the z-component, we get

$$\begin{aligned} -\sin\theta_i \frac{\mathrm{d}\theta_i}{\mathrm{d}t} =& -\gamma \sin\theta_i \big[(-b\sin\theta_b \sin\phi_b + B_x\lambda\cos\theta_i - B_y)\cos\phi_i \\ &+ (b\sin\theta_b\cos\phi_b + B_y\lambda\cos\theta_i + B_x)\sin\phi_i - B_z\sin\theta_i\lambda\big] \end{aligned} \tag{B.5}$$

$$\begin{aligned} \frac{\mathrm{d}\theta_i}{\mathrm{d}t} =& \frac{-1}{\sin\theta_i}\Big(-\gamma \sin\theta_i \big[(-b\sin\theta_b \sin\phi_b + B_x\lambda\cos\theta_i - B_y)\cos\phi_i \\ &+ (b\sin\theta_b\cos\phi_b + B_y\lambda\cos\theta_i + B_x)\sin\phi_i - B_z\sin\theta_i\lambda\big]\Big) \end{aligned} \tag{B.6}$$

Taking the y-component

$$\begin{aligned} \cos\theta_i \sin\phi_i \frac{\mathrm{d}\theta_i}{\mathrm{d}t} + \sin\theta_i\cos\phi_i \frac{\mathrm{d}\phi_i}{\mathrm{d}t} =& \lambda B_x\gamma\cos\phi_i\sin\phi_i\cos^2\theta_i \\ &- \lambda B_y\gamma\cos^2\phi_i\cos^2\theta_i \\ &- \lambda B_z\gamma\sin\theta_i\sin\phi_i\cos\theta_i \\ &- \lambda B_x\gamma\cos\phi_i\sin\phi_i \\ &+ \lambda B_y\gamma\cos^2\phi_i \\ &+ \lambda B_y\gamma\cos^2\theta_i \\ &- b\gamma\sin\theta_i\cos\phi_i\cos\theta_b \\ &+ b\gamma\sin\theta_b\cos\phi_b\cos\theta_i \\ &- B_z\gamma\sin\theta_i\cos\phi_i \\ &+ B_x\cos\theta_i \end{aligned} \tag{B.7}$$

$$\begin{aligned}\frac{\mathrm{d}\phi_i}{\mathrm{d}t} =& \frac{\gamma}{\sin\theta_i \cos\phi_i}(\lambda B_x \cos\phi_i \sin\phi_i \cos^2\theta_i \\ &- \lambda B_y \cos^2\phi_i \cos^2\theta_i \\ &- \lambda B_z \sin\theta_i \sin\phi_i \cos\theta_i \\ &- \lambda B_x \cos\phi_i \sin\phi_i \\ &+ \lambda B_y \cos^2\phi_i \\ &+ \lambda B_y \cos^2\theta_i \\ &- b \sin\theta_i \cos\phi_i \cos\theta_b \\ &+ b \sin\theta_b \cos\phi_b \cos\theta_i \\ &- B_z \sin\theta_i \cos\phi_i \\ &+ B_x \cos\theta_i \\ &- \frac{1}{\gamma} \cos\theta_i \sin\phi_i \frac{\mathrm{d}\theta_i}{\mathrm{d}t}\end{aligned} \tag{B.8}$$

Insert Eq. B.6

$$\begin{aligned}\frac{\mathrm{d}\phi_i}{\mathrm{d}t} =& \frac{\gamma}{\sin\theta_i \cos\phi_i}(\lambda B_x \cos\phi_i \sin\phi_i \cos^2\theta_i \\ &- \lambda B_y \cos^2\phi_i \cos^2\theta_i \\ &- \lambda B_z \sin\theta_i \sin\phi_i \cos\theta_i \\ &- \lambda B_x \cos\phi_i \sin\phi_i \\ &+ \lambda B_y \cos^2\phi_i \\ &+ \lambda B_y \cos^2\theta_i \\ &- b \sin\theta_i \cos\phi_i \cos\theta_b \\ &+ b \sin\theta_b \cos\phi_b \cos\theta_i \\ &- B_z \sin\theta_i \cos\phi_i \\ &+ B_x \cos\theta_i) \\ &+ \gamma \cot\theta_i \tan\phi_i(-b \sin\theta_b \sin\phi_b \cos\phi_i \\ &+ B_x \lambda \cos\theta_i \cos\phi_i \\ &- B_y \cos\phi_i \cos\theta_i \sin\phi_i \\ &+ b \sin\theta_b \cos\phi_b \sin\phi_i \\ &+ B_y \lambda \cos\theta_i \sin\phi_i \\ &+ B_x \sin\phi_i \\ &- B_z \sin\theta_i \lambda)\end{aligned} \tag{B.9}$$

(B.10)

The equations are kept expanded for ease of implementation. Equations B.6 and B.9 are used for simulations.